Title

Pelagic barite formation, dissolution, and preservation: contextualizing a marine carbon cycle proxy

Author

Light, Tricia M

Publication Date

2023

Peer reviewed|Thesis/dissertation

UNIVERSITY OF CALIFORNIA SAN DIEGO

Pelagic barite formation, dissolution, and preservation: contextualizing a marine carbon cycle proxy

A Dissertation submitted in partial satisfaction of the requirements
for the degree Doctor of Philosophy

in

Oceanography

by

Tricia Light

Committee in charge:

Richard Norris, Chair
Christopher Charles
Julia Diaz
Olivia Graeve
Jules Jaffe

2023

The Dissertation of Tricia Light is approved, and it is acceptable in quality and form for publication on microfilm and electronically.

University of California San Diego

2023

DEDICATION

To my grandmother, who taught a 4-year-old about climate change, filled my childhood with science, and epitomized a life of service.

TABLE OF CONTENTS

DISSERTATION APPROVAL PAGE iii

DEDICATION iv

TABLE OF CONTENTS v

LIST OF FIGURES viii

LIST OF TABLES xi

LIST OF ABBREVIATIONS xii

ACKNOWLEDGEMENTS xiii

VITA xv

ABSTRACT OF THE DISSERTATION xvii

INTRODUCTION 1

References 3

CHAPTER 1. Quantitative visual analysis of marine barite microcrystals: insights into precipitation and dissolution dynamics 6

Abstract 6

Introduction 7

Methods 8

Results 15

Discussion 21

Conclusions 28

Acknowledgements 29

References 29

CHAPTER 2. Marine barite morphology as an indicator of biogeochemical conditions within organic matter aggregates 34

Abstract 34

Introduction 35

Materials and Methods 39

Results 47

Discussion 53

Acknowledgements 64

References 64

CHAPTER 3: Water column barium sulfate dissolution and shielding by organic matter aggregates: Implications for the pelagic barite proxy 73

Abstract 73

Introduction 74

Materials and Methods 77

Results 88

Discussion 96

Conclusions 107

Acknowledgements 107

References 108

CHAPTER 4: Marine barite dynamics across the sediment water interface and along an offshore gradient 117

Abstract 117

Introduction 118

Materials and Methods 120

Results 124

Discussion 127

Conclusions and Next Steps 131

Acknowledgements 132

References 132

CONCLUSIONS 135

SUPPLEMENTARY INFORMATION 137
Supplementary Information for CHAPTER 1 137
Supplementary Information for CHAPTER 2 139
Supplementary Information for CHAPTER 3 142
Supplementary Information for CHAPTER 4 150

LIST OF FIGURES

Figure 1. Locations of sampling sites S1–S5 in the Eastern Pacific. Bathymetry is from the global multiresolution topography (GMRT) synthesis (Ryan 2009). 9

Figure 2 (A) Abundances of all barite microcrystals, (B) dissolved oxygen concentrations, (C) abundances of clusters of adjoined barite microcrystals, and (D) temperature with depth in the water column. Abundance points indicate average abundance ± standard error across the three filter fields analyzed for each sampling depth and site. Vertical lines and text labels indicate ... 11

Figure 3. Representative barite microcrystals displaying a range of morphologies. (A) Large, platy barite microcrystal potentially hydrothermal in origin. (B) Barrel-shaped barite microcrystal in association with organic matter. (C) Barrel-shaped barite microcrystal displaying etch pits and signs of dissolution. (D) Cluster of submicron, barrel-shaped barite 16

Figure 4. Average particle area per barite microcrystal by depth and site. Points indicate average area ± standard error for each sampling depth and site. Vertical lines and shading indicate average abundance ± standard error for each water layer. 19

Figure 5. Average (A) area and (B) solidity for barite microcrystals that were and were not associated with organic matter in each water column layer. Error bars display standard error. N = 1325, 2389, and 718 for surface, OMZ, and deep water layers, respectively. Asterisks indicate significant differences within water layers, $*p < 0.05$ and $***p < 0.001$. 20

Figure 6. Solidity for single barite microcrystals by depth. Box plots display the median and first and third quartiles, whiskers display higher and lower values to the 1.5× interquartile range, and points display outlying values. Vertical lines and text labels indicate average abundance ± standard error for each water layer. 24

Figure 7. Representative marine barite crystals collected from a water depth of 200 m in the North Pacific. A), B), and C) Typical elliptical or barrel-shaped barite crystals. D) Six-sided barite crystal with irregular edges. See Light and Norris 2021 for detailed information regarding crystal collection and analysis. 39

Figure 8. SEM images of representative barite crystal morphologies for treatments A) SI-1.5, B) SI-2, C) SI-2.5, D) SI-3, and E) SI-3.5. 48

Figure 9. SEM images of representative barite crystal morphologies for treatments A) Formic, B) Ascorbic, C) Pyromellitic, and D) EDTA. Insets depict the chemical structure of the corresponding organic compound. HRTEM images of crystals from E) Formic, F) Ascorbic, G) Pyromellitic, and H) EDTA treatments. Ba and S elemental composition maps of 49

Figure 10. SEM images of representative barite crystal morphologies for treatments A) Ethanol, B) Soy-10, C) Soy-50, D) Soy-100, and E) Soy-200. HRTEM images and corresponding elemental composition maps for treatments F-I) SI-2.5, L-O) Soy-100, and R-U) Soy-200. Lattice-fringe images and SAED patterns for a region of the corresponding crystal for J). 51

Figure 11. SEM images of representative barite crystal morphologies for treatments A) Soy-100, B) Time-10, C) Time-30, and D) Time-120. Lattice-fringe images and SAED patterns for crystals from treatments E) and F) Soy-100, G) and H) Time-10, and I) and J) Time-30. Lattice-fringe images show d-spacings characteristic of barite: 3.10 Å (211) for E, 2.33 Å (220) 52

Figure 12. Average barite crystal area with experiment duration. The red line shows average barite crystal area for marine barite crystals collected from the North Pacific (Light and Norris 2021). 52

Figure 13. Generalized schematic of characteristic barite size and morphology as a function of experimental barite saturation index, experiment duration, and soy phospholipid concentrations. Filled symbols indicate experimental conditions that yielded barite crystals that resemble marine barite. 54

Figure 14. SEM images of representative barium sulfate microcrystals over time from No Aggregate, Overlying Water, and Aggregate treatments of the organic matter shielding experiment. Yellow numbers indicate the number of clearly visible, well-defined crystal faces assigned to each particle. 79

Figure 15. A) SEM images of representative barium sulfate microcrystals from pH, salinity, and temperature experiments on Day 0, Day 7, and Day 14. B) TEM results for select crystals from Day 0 (pH = 7.9/psu = 34/4 °C treatment), Day 7 (psu = 26.7 treatment), and Day 14 (pH = 7.9/psu = 34/4 °C treatment). i) HRTEM images. ii) Lattice fringe images, with ten unit 80

Figure 16. Barium sulfate A) total area per field, B) mass per crystal, and C) average number of well-defined crystal faces per field over time for No Aggregates, Overlying Water, and Aggregate treatments of the organic matter shielding experiment. Red dashed lines show fitted linear regression curves with standard error in gray for all parameters with a statistically.....90

Figure 17. Barium sulfate mass per crystal over time for free crystals in the A) pH, B) salinity, and C) temperature variation experiments. Red dashed lines show fitted linear regression curves for each treatment with a statistically significant ($p < 0.05$) change over time (see Supplementary Information 3.2 for regression values). Interaction between treatment and rate of change.....94

Figure 18. Schematic illustrating the proposed role of organic matter aggregates (depicted in green) in protecting pelagic barite crystals (depicted as purple diamonds) from dissolution in the water column. Schematic is not to scale, and water depths are approximate as each of the processes listed occur over a wide range of depths. 103

Figure 19. A) Salinity and B) transmission profiles acquired during CTD down casts at study sites S1-S5. Profiles were smoothed via boxcar averaging with a step size of 10 dbar. 137

Figure 20. Schematic representing barite microcrystal image analysis. SEM images were binarized, smoothed, and quantitatively analyzed for area, solidity, aspect ratio, and circularity according to the equations displayed above.....137

Figure 21. Histograms of barite microcrystal A) major axis and B) minor axis lengths for all single microcrystals and microcrystal clusters. A) omits 39 outliers with lengths ranging from 4-15 µm and B) omits 7 outliers with widths ranging from 4-6 µm.....138

Figure 22. Histograms of barite microcrystal A) aspect ratio and B) circularity by sample site for all single particles, omitting barite clusters. A) omits 40 outliers with aspect ratios ranging from 4-7.25. 139

Figure 23. SEM images of representative barite crystal morphologies for crystals precipitated under Ba^{2+}:Sr^{2+} ratios of A) 10:1, B) 5:1, C) 1:1, D) 1:5, and E) 1:10. Barite crystal size and morphology were comparable between all 5 treatments. Apart from the quantity of $Sr(NO_3)_2$ added to the solution, experimental conditions were identical to those described for.....139

Figure 24. SEM images of barite crystal morphologies for crystals precipitated under Ba^{2+}:SO_4^{2-} ratios of A) 1:625, B) 1:2000, C) 1:7145, and D) 1:16670. Barite crystal size and morphology were comparable between treatments A-C, while crystals from treatment D were slightly smaller and displayed more rounded corners. Concentrations of Ba^{2+} and SO_4^{2-} were adjusted. 140

Figure 25. CrysTBox indexing analysis results for a SAED pattern of a barite crystal synthesized in the presence of EDTA. The annotated diffraction spot indices (A) and axes (B) are consistent with a crystal basal face of (0,1,1). 142

Figure 26. Organic matter aggregates imaged immediately before destructive sampling on incubation days 2, 3, 8, 12, and 16. Grid underneath the aggregates show 1 cm x 1cm larger squares and 1 mm x 1 mm smaller squares.....142

Figure 27. Barite crystal area per particle over time for No Aggregate, Overlying Water, and Aggregate treatments of the organic matter shielding experiment. Red dashed lines show fitted linear regression curves with standard error calculated by local regression in gray. 144

Figure 28. Barite crystal area per particle over time for A) pH, B) salinity, and C) temperature variation experiments. Red dashed lines show the fitted linear regression curve.....145

Figure 29. Representative barite crystals from day 21 of the pH, salinity, and temperature experiments. 145

LIST OF TABLES

Table 1. Sampling locations and depths. In total, 54 samples were collected across 5 sites. 10

Table 2. Experimental parameters, analyses conducted, and resultant barite crystal morphologies. SI is the saturation index, while other experiments focused on varying concentrations of organic additives and experiment duration times. All Soy and Time treatments also contained 9 % v/v ethanol. 43

Table 3. pH, salinity, temperature, and estimated barium sulfate saturation state for barium sulfate dissolution rate experimental treatments. pH = 7.9/psu = 34/4 °C and 20 °C treatments used unmodified filtered seawater, and pH and/or salinity were adjusted for all other treatments. 83

Table 4. Linear regression values for No Aggregate, Overlying Water, and Aggregate treatments of the organic matter shielding experiment. Regressions were calculated with time in days as the independent variable. 92

Table 5. Linear regression values for pH, salinity, and temperature experiments. A single regression was conducted using data from all treatments within each experiment. Regressions were calculated with time in days as the independent variable and crystal mass as the dependent variable. 95

Table 6. Semi-quantitative EDX spectra spot analyses of phosphorous intensity relative to sulfur intensity for SI-2.5, Soy-100, and Soy-200 treatments. Phosphorous (P) intensity was measured at 2.01 keV, and sulfur (S) was measured at 2.31 keV. 141

Table 7. Estimated concentrations of seawater cations and anions for all treatments of the salinity experiment. Seawater for all other experimental treatments was assumed to have the same composition as the psu = 34 treatment. 143

Table 8. Linear regression values for each treatment of the pH, salinity, and temperature experiments. Regressions were calculated with time in days as the independent variable and crystal mass as the dependent variable. Since rate of change in crystal mass did not significantly vary with treatment, these regression values were only calculated for visualization purposes. . 146

Table 9. Comparison of surface area normalized barium sulfate dissolution rates observed in this investigation with those calculated from rate constants reported in Zhen-Wu et al. (2016). $\Omega BaSO4$ is the average of the estimated $\Omega BaSO4$ of each treatment in the specified experiment. Average surface area (SA) per barium sulfate crystal at Day 0 is estimated by multiplying 147

Table 10. Correlations between core top Ba measurements, other marine carbon cycle proxies, and export production estimates from datasets presented in Hayes et al. (2020), Schoeopfer et al. (2015), Serno et al. (2014), and Shen et al. (2023). Data from Schoeopfer et al. (2015) and Shen et al. (2023) suggest that sediment barite shows a stronger positive correlation with some 148

LIST OF ABBREVIATIONS

CTD	Conductivity Temperature Depth sensor
DO	Dissolved Oxygen
EDS	Energy-Dispersive X-ray Spectroscopy
EPS	Extracellular Polymeric Substances
HRTEM	High Resolution Transmission Electron Microscopy
OMZ	Oxygen Minimum Zone
SEM	Scanning Electron Microscope
TEP	Transparent Exopolymer Particles

ACKNOWLEDGEMENTS

This dissertation was made possible by a fantastic amount of love and support from my family and friends. My parents, Lori and Roger, have always nurtured my curiosity, encouraged my ambitions, and shown me how to enjoy life while also working hard. My partner, Benjamin, has been my biggest champion and made all this work possible in so many ways. My sister, Liz, has always been there for me, and my Aunt Patty has been a constant source of encouragement. I have the most incredible friends, and I could not even begin to list everything they have done for me. I am so grateful for my Wednesday crew, my wonderful SIO cohort, and the more senior students who have given me so much guidance over the past five years.

I would like to thank my advisor, Professor Richard Norris, for taking me in, having enormous faith in me, and always encouraging me to make my own path through graduate school. I am grateful for the assistance and support of my committee members, Professors Christopher Charles, Julia Diaz, Olivia Graeve, and Jules Jaffe. I also owe a huge thanks to my previous mentors—particularly Dr. Branwen Williams of the Keck Science Department of the Claremont Colleges and Drs. Núria Catalán and Rafael Marcé of the Institut Català de Recerca de l'Aigua—for shaping so much of who I am as a scientist.

This work has also been made possible by the invaluable contributions of my collaborators and colleagues. Thank you so much to Dr. Francisca Martínez Ruiz for contributing greatly to my understanding of marine barite dynamics and making my HRTEM analyses possible. Dr. Jennifer Prairie's generosity and expertise was essential to the success of Chapter 3. Manuel Garcia excelled in the lab and was so helpful in experiment monitoring and analysis. Many thanks to the science parties, captains, and crews of R/V Sally Ride cruises SR 2002 and SR 2215, and to Natalia Erazo for being an incredible co-chief scientist. Finally, I am

very grateful for the assistance of the many anonymous reviewers who have improved improved this work.

Chapter 1, in full, is a reprint of the material as it appears in “Quantitative visual analysis of marine barite microcrystals: Insights into precipitation and dissolution dynamics,” published in Limnology and Oceanography in 2021. T. Light and R. Norris. The dissertation author was the primary investigator and author of this paper.

Chapter 2, in full, a reprint of the material as it appears in “Marine barite morphology as an indicator of biogeochemical conditions within organic matter aggregates,” published in Geochimica et Cosmochimica Acta in 2023. T. Light, F. Martínez-Ruiz, and R. Norris. The dissertation author was the primary investigator and author of this paper.

Chapter 3, in full, is a reprint of the material as it appears in “Water column barium sulfate dissolution and shielding by organic matter aggregates: Implications for the pelagic barite proxy,” published in Chemical Geology in 2023. T. Light, M. Garcia, J. C. Prairie, F. Martínez-Ruiz, and R. Norris. The dissertation author was the primary investigator and author of this paper.

Chapter 4 contains unpublished material and is coauthored with R. Norris. The dissertation author was the primary investigator and author of this paper.

VITA

2017 Bachelor of Arts in Chemistry, Scripps College

2018 Fulbright Research Scholar, Catalan Institute for Water Research

2020 Master of Science in Oceanography, University of California San Diego

2023 Doctor of Philosophy in Oceanography, University of California San Diego

PUBLICATIONS

T. Light, E. Norris, D. Zhai, R. Varner, K. B. Lanpher, D. Capone, N. G. Erazo, and R. Norris (In Press). All aboard! Behind the scenes of a scientific research cruise. *Frontiers for Young Minds*.

N. G. Erazo, T. Light, D. A. Capone, A. Effinger, P. F. Erazo, L. Huang, A. Kannad, K. B. Lanpher, E. Norris, S. O. Perry, E. Romero, T. M. Russell, R. I. Varner, L. Wicker, A. Yu, D. Zhai, and R. D. Norris (In Press). The Ocean as a Classroom: Considering the Roles of Equity, Diversity, and Justice in Oceanographic Knowledge Production to Promote Accessibility for Future Generations. *Oceanography*.

T. Light, F. Martínez-Ruiz, and R. Norris (2023). Marine barite morphology as an indicator of biogeochemical conditions within organic matter aggregates. *Geochimica et Cosmochimica Acta*, 358 (38-48).

Light, T., M. Garcia, J. C. Prairie, F. Martínez-Ruiz, and R. Norris (2023). Water column barium sulfate dissolution and shielding by organic matter aggregates: Implications for the pelagic barite proxy. *Chemical Geology*, 121637.

Light, T., E. Mcintosh, and O. Stephenson (2022). Advancing Equity in Access to Distributed Energy Resources in California. *Journal of Science Policy and Governance*, 20(01).

Light, T. and R. Norris (2021). Quantitative Visual Analysis of Marine Barite Microcrystals: Insights into Precipitation and Dissolution Dynamics. *Limnology and Oceanography*, 66(10).

Xu, X., H. Wei, G. Barker, K. Holt, S. Julian, T. Light, S. Melton, A. Salamanca, K. Moffett, J. McClelland, and A. Hardison (2020). Tidal Freshwater Zones as Hotspots for Biogeochemical Cycling: Sediment Organic Matter Decomposition in the Lower Reaches of two South Texas Rivers. *Estuaries and Coasts*, 44 (722-733).

Light, T., B. Williams, J. Halfar, A. Hou, Z. Zajacz, A. Tsay, and W. Adey (2018). Advancing Mg/Ca Analysis of Coralline Algae as a Climate Proxy by Assessing LA-ICP-OES Sampling and Coupled Mg/Ca and δ18O Analysis. *Geochemistry, Geophysics, and Geosystems*, 19.

Pastor, A., N. Catalán, N. Nagar, T. Light, C. Borrego, and R. Marcé (2018). A Universal Bacterial Inoculum for Dissolved Organic Carbon Biodegradation Experiments in Freshwaters. *Limnology and Oceanography: Methods*, 16(7).

FIELD OF STUDY

Major Field: Oceanography
Studies in Marine Chemistry and Geochemistry
Professor Richard Norris

ABSTRACT OF THE DISSERTATION

Pelagic barite formation, dissolution, and preservation: contextualizing a marine carbon cycle proxy

by

Tricia Light

Doctor of Philosophy in Oceanography

University of California San Diego, 2023

Professor Richard Norris, Chair

The marine carbon cycle is a major driver of global climate. Reliable marine carbon cycle proxies are required to study the relationship between life in the ocean and climate in the past and to predict how the marine carbon cycle may change in the future. Pelagic barite in marine sediments is a valuable marine carbon cycle proxy. However, many aspects of pelagic barite dynamics are poorly constrained. Important questions remain regarding how and where pelagic

barite forms, what factors influence pelagic barite dissolution in the water column, and which aspects of the marine carbon cycle the pelagic barite proxy captures. This dissertation presents observational studies and laboratory experiments that shed light on these questions and thus advance the ability of the pelagic barite proxy to provide insights into earth's history. Chapter 1 presents a quantitative visual analysis of 5481 barite microcrystals from the Eastern Pacific water column. This extensive dataset provides new evidence for the role of organic matter aggregates in barite formation and suggests that barite records are influenced by water column dissolution and spatially heterogeneous formation. Chapter 2 uses laboratory experiments to constrain physical and chemical conditions during pelagic barite formation. These findings suggest that pelagic barite forms in marine organic matter aggregate microenvironments that are short-lived, moderately supersaturated with respect to barite, and rich in soy phospholipids. Chapter 3 uses laboratory incubations to constrain plausible water column pelagic barite dissolution rates under a range of seawater conditions. These experiments suggest that organic matter aggregates play a vital role in shielding pelagic barite from dissolution, which implies that the pelagic barite proxy captures the arrival of organic matter to the sediment-water interface. Chapter 4 presents preliminary findings regarding how pelagic barite size, abundance, and morphology vary within sediment core tops and across the sediment water interface over an offshore gradient off the coast of Southern California. This early work suggests differential dissolution of very small barite crystals at the sediment-water interface, and the data and samples acquired for this investigation are available for potential collaborators interested in pursuing the topic further. Together, these chapters increase our confidence in the barite proxy by shedding light on pelagic barite formation, dissolution, and preservation. This work advances the accurate and reliable interpretation of barite records to gain insight into past ocean conditions.

INTRODUCTION

The biological pump, or the biologically driven sequestration of carbon from the atmosphere into the deep ocean, plays a key role in determining atmospheric carbon dioxide concentrations and thus global climate (DeVries, 2022). Quantifying how the biological pump responds to variable climate, biogeochemical, and ecosystem conditions is vital to accurately predicting how the marine carbon cycle will function in the future, particularly in the face of anthropogenic climate change and other human influences (e.g., Fakhraee et al., 2020; Nowicki et al., 2022). However, the marine carbon pump and associated burial of organic carbon in marine sediments is difficult to quantify in the modern ocean, let alone in the past (Hain, Sigman, and Haug, 2014). Many different bieogeochemical proxies have been used to reconstruct aspects of the marine carbon cycle over time, but these proxies each present their own limitations (e.g., Calvert and Pedersen, 2007).

Pelagic barite, also referred to as marine barite, is a particularly valuable marine carbon cycle proxy (Carter et al., 2020; Horner et al., 2021). Barite is a naturally occurring mineral consisting of barium sulfate ($BaSO_4$), and pelagic barite is barite that forms within the ocean water column (Horner et al., 2021). Pelagic barite precipitates from barium (Ba^{2+}) and sulfate (SO_4^{2-}) ions in seawater. Barium is a naturally occurring trace element in the ocean, and its primary inputs are river runoff and hydrothermal activity (Wolgemuth and Broecker, 1970). Sulfate is the second most abundant anion in the modern ocean and is ubiquitous throughout the water column (Millero, 1974).

Pelagic barite in seawater and marine sediments has been linked to primary productivity and the export of organic carbon for decades (e.g., Turekian and Tausch, 1964; Wolgemuth and Broeker, 1970). The ocean is largely undersaturated with respect to barite (Monnin et al., 1999),

but pelagic barite precipitates within supersaturated microenvironments within decomposing organic matter aggregates (Bishop, 1988; Ganeshram et al., 2003). Thus, pelagic barite is thought to serve as an ecosystem-wide carbon export proxy not directly tied to any one organism (Martinez-Ruiz et al. 2018). The accumulation rate of barite in marine sediments is widely used as a proxy for organic carbon export out of the surface ocean (e.g., Carter et al., 2016; Erhardt et al., 2013; Kim et al., 2022; Lowery and Bralower, 2022). Pelagic barite in marine sediments also serves as an archive of past seawater chemistry (e.g., Markovic et al., 2016; Paytan et al., 1993; Yao et al., 2020). As a result, the pelagic barite proxy has shed light onto ocean conditions during key periods of earth's history such as the Paleocene-Eocene Thermal Maximum, the Pliocene-Pleistocene transition, and Quaternary glacial to interglacial transitions (e.g., Bridgestock et al., 2019, Ma et al., 2015; Paytan et al., 1996).

Despite its widespread use as a proxy, the factors influencing pelagic barite formation, dissolution, and preservation are poorly understood, and these uncertainties limit its utility as a tool for studying the marine carbon cycle (e.g., Carter et al. 2020; Yao et al. 2020). In this dissertation, I shed light on these knowledge gaps through a combination of observational and experimental work. In my first chapter, I collected, imaged, and quantitatively analyzed thousands of barite microcrystals from the Eastern Pacific water column to obtain direct evidence for hypothesized water column barite processes. In my second chapter, I conducted a series of laboratory experiments to determine how characteristic pelagic barite crystals might form within organic matter aggregates. In my third chapter, I used laboratory experiments to constrain water column barite dissolution rates and evaluate how organic matter aggregates shield barite from dissolution. Finally, in my fourth chapter, I quantitatively analyze pelagic barite from the sediment and water column across an offshore gradient in the Eastern Pacific to

assess how barite changes across the sediment-water interface and under different oceanographic conditions. Together, these chapters increase our confidence in pelagic barite as an ecosystem-wide carbon cycle proxy, suggest that the barite record captures the arrival of organic matter to sediments, and highlight spatial heterogeneity and preservation across the sediment-water interface as topics that merit additional study. Thus, this work addresses current shortcomings in our ability to interpret pelagic barite proxy records and advances marine barite as a valuable tool for studying marine ecosystem change.

References

Bishop, J. K. B. 1988. The Barite-Opal-Organic Carbon Association in Oceanic Particulate Matter. Nature. 332, 341.

Bridgestock, L., Hsieh, Y. T., Porcelli, D., Henderson, G. M. 2019. Increased export production during recovery from the Paleocene–Eocene thermal maximum constrained by sedimentary Ba isotopes. Earth Planet. Sci. Lett. 510, 53–63.

Calvert, S. E., Pedersen, T. F. 2007. Elemental proxies for palaeoclimatic and palaeoceanographic variability in marine sediments: interpretation and application. In: Hillaire-Marcel, C., De Vernal, A. (Eds.), Proxies in Late Cenozoic Paleoceanography. Elsevier, Amsterdam. 567–644.

Carter, S. C., Griffith, E. M., Penman, D. E. 2016. Peak intervals of equatorial Pacific export production during the middle Miocene climate transition. Geology. 44, 923-926.

Carter, S., Paytan, A., Griffith, E. 2020. Toward an improved understanding of the marine barium cycle and the application of marine barite as a paleoproductivity proxy. Minerals. 10, 421.

DeVries, T. 2022. The ocean carbon cycle. Annu. Rev. Environ. Resour. 47, 317–341.

Erhardt, A. M., Pälike, H., Paytan, A. 2013. High-resolution record of export production in the eastern equatorial Pacific across the Eocene-Oligocene transition and relationships to global climatic records. Paleoceanogr. 28, 130-142.

Fakhraee, M., Planavsky, N.J., Reinhard, C.T. 2020. The role of environmental factors in the long-term evolution of the marine biological pump. Nat. Geosci. 13, 812–816.

Ganeshram, R. S., François, R. Commeau, J., Brown-Leger, S. L. 2003. An Experimental Investigation of Barite Formation in Seawater. Geochim. Cosmochim. Acta. 67, 2599–2605.

Hain, M., Sigman, D., Haug, G. 2014. The biological pump in the past. In H. Holland and K. Turekian (Eds.), Treatise on Geochemistry. Elsevier, Oxford. 485-517.

Horner, T.J., Crockford, P.W. 2021. Barium Isotopes: Drivers, Dependencies, and Distributions Through Space and Time. Cambridge University Press.

Kim, J. E., Westerhold, T., Alegret, L., Drury, A. J., Röhl, U., Griffith, E. M. 2022. Precessional pacing of tropical ocean carbon export during the Late Cretaceous. Clim. Past. 18, 2631-2641.

Lowery, C. M., Bralower, T. J. 2022. Elevated Post K-Pg Export Productivity in the Gulf of Mexico and Caribbean. Paleoceanogr. Paleoclim. 37, e2021PA004400.

Ma, Z., Ravelo, A.C., Liu, Z., Zhou, L., Paytan, A. 2015. Export production fluctuations in the eastern equatorial Pacific during the Pliocene-Pleistocene: reconstruction using barite accumulation rates. Paleoceanogr. 30, 1455–1469.

Markovic, S., Paytan, A., Li, H., Wortmann, U. G. 2016. A Revised Seawater Sulfate Oxygen Isotope Record for the Last 4Myr. Geochim. Cosmochim. Acta. 175, 239–51.

Martinez-Ruiz, F., Jroundi, F., Paytan, A., Guerra-Tschuschke, I., del Mar Abad, M., González-Muñoz, M. 2018. Barium bioaccumulation by bacterial biofilms and implications for Ba cycling and use of Ba proxies. Nat. Commun. 9, 1619.

Millero, Frank. 1974. Seawater as a Multicomponent Electrolyte Solution. In: Goldberg, E. D. (Eds.), The Sea. Wiley, New York. 3-80.

Monnin, C., Jeandel, C., Cattaldo, T., Dehairs, F. 1999. The Marine Barite Saturation State of the World's Oceans. Mar. Chem. 65, 253–61.

Nowicki, M., DeVries, T., Siegel, D. A. 2022. Quantifying the carbon export and sequestration pathways of the ocean's biological carbon pump. Glob. Biogeochem. Cycles 36, e2021GB007083.

Paytan, A., Kastner, M., Chavez, F. P. 1996. Glacial to interglacial fluctuations in productivity in the equatorial pacific as indicated by marine barite. Science. 274, 1355–1357.

Paytan, A., Kastner, M., Chavez, F.P. 1996. Glacial to interglacial fluctuations in productivity in the equatorial pacific as indicated by marine barite. Science. 274, 1355–1357.

Paytan, A., Kastner, M., Martin, E. E., Macdougall, J. D., Herbert, T. 1993. Marine Barite as a Monitor of Seawater Strontium Isotope Composition. Nature. 366, 445– 449.

Turekian, K. K., Tausch, E. H. 1964. Barium in Deep-sea Sediments of the Atlantic Ocean. Nature. 201, 4920.

Wolgemuth, K., Broecker, W.S. 1970. Barium in sea water. Earth Planet. Sci. Lett. 8, 372-378.

Yao, W., Paytan, A., Griffith, E. M., Martínez-Ruiz, F., Markovic, S., Wortmann, U. G. 2020. A

Revised Seawater Sulfate S-Isotope Curve for the Eocene. Chem. Geol. 532, 119382.

CHAPTER 1. Quantitative visual analysis of marine barite microcrystals: insights into precipitation and dissolution dynamics

T. Light and R. Norris.

Abstract

The accumulation rate of authigenic barite ($BaSO_4$) in marine sediments is a promising proxy for reconstructing marine export production, but many aspects of barite precipitation and dissolution in the water column remain unknown. Here, we collected, imaged, and quantitatively analyzed 5481 barite microcrystals in bottle casts from the Eastern Pacific water column to gain a better understanding of in situ barite dynamics. Barite crystal abundance increases rapidly between the surface and 500 m in depth and then declines to predominantly low abundances below ~ 1000 m. The falloff in barite abundance between the oxygen minimum zone (OMZ) and the ocean interior suggests 60% ± 20% loss of barite by dissolution, nearly all of which is complete by water depths of 1000 m. However, there are occasional samples, as deep as 1250 m, with unusually high barite abundance that may represent marine snow deposition events. We found that microcrystals associated with organic matter substrates were smaller and less solid than free crystals, which suggests ongoing barite precipitation toward larger, more regularly shaped microcrystals within organic matter aggregates. Trends in barite microcrystal size with depth suggest that organic matter aggregates also play a role in shielding barite microcrystals from dissolution. In addition, our extensive data set raises new questions regarding marine barite nucleation and spatial heterogeneity. By helping bridge the gap between hypothesized barite dynamics and in situ observations of barite microcrystals, this study advances our understanding of water column Ba processes and the utility of sediment barite as an export production proxy.

Introduction

Export production, or the downward flux of organic carbon out of the surface ocean, plays an important role in regulating atmospheric carbon dioxide concentrations and thus global climate on a range of time scales (e.g., DeVries et al. 2012; Martínez-García et al. 2014; Gottschalk et al. 2019). Reliable proxies for export production in the geologic past are necessary to constrain the effect of climate on export production and vice versa. While various export production proxies have been employed, these proxies all present their own limitations (Hain et al. 2014).

The accumulation rate of the mineral barite ($BaSO_4$) in marine sediments and related sediment parameters are particularly promising proxies for reconstructing export production (Paytan and Griffith 2007; Griffith and Paytan 2012; Carter et al. 2020). The ocean is largely undersaturated with respect to barite (Monnin et al. 1999), but barite microcrystals are observed throughout the water column (e.g., Dehairs et al. 1980; Bishop 1988). Marine sediments that underlay more productive regions have been observed, since the mid-20th century, to contain elevated Ba concentrations (Chow and Goldberg 1960; Turekian and Tausch 1964). Extensive evidence has explained this correlation by barite precipitation within microenvironments created by sinking organic matter aggregates in the water column (e.g. Bertram and Cowen 1997; Ganeshram et al. 2003; Horner et al. 2015).

Recent work has helped illuminate the exact processes by which this barite precipitation occurs. Laboratory experiments and in situ observations suggest that bacterial biofilms, and in particular extracellular polymeric substances (EPS), mediate authigenic barite precipitation by concentrating Ba via amorphous, P-rich barite precursors (Martinez-Ruiz et al. 2018, 2019, 2020). Several strains of bacteria have also been shown to facilitate barite

precipitation in the laboratory (González-Muñoz et al. 2003, 2012; Torres-Crespo et al. 2015). However, many aspects of marine barite precipitation remain elusive, in part due to the relative scarcity of direct observations of barite microcrystals in the water column.

The extent of barite dissolution in the water column is also poorly constrained (Carter et al. 2020). Approximately, 70% of authigenic barite deposited at the sediment water interface is thought to dissolve before incorporation into the sediment record (Paytan and Kastner 1996). Qualitative morphological evidence of microcrystal etching and dissolution pits suggests that barite dissolution is also widespread in the water column (Sun et al. 2015). However, organic matter aggregates may play an important role in protecting barite microcrystals from dissolution (Carter et al. 2020).

A robust understanding of the factors that control water column barite precipitation and dissolution in the water column is crucial to our ability to reliably use sediment Ba proxies to reconstruct past export production. Here, we quantitatively analyze high-resolution images of over 5000 barite microcrystals to shed light on how organic matter aggregates influence barite precipitation and dissolution and other aspects of the marine Ba cycle.

Methods

Sample collection

Barite microcrystals were collected during a cruise of the R/V Sally Ride from 13 January 2020 to 21 January 2020 along the Fieberling-Guadalupe Seamount Chain in the Eastern Pacific (Fig. 1). This relatively oligotrophic ocean region experiences large-scale flows associated with the eastern rim of the subtropical gyre, southward surface flow associated with the California current, and northwestward currents from the equator (Roden 1991). The study

site is 800 km from the nearest-known active hydrothermal vent, the White Point vent off the coast of Southern California (Beaulieu and Szafrański 2020).

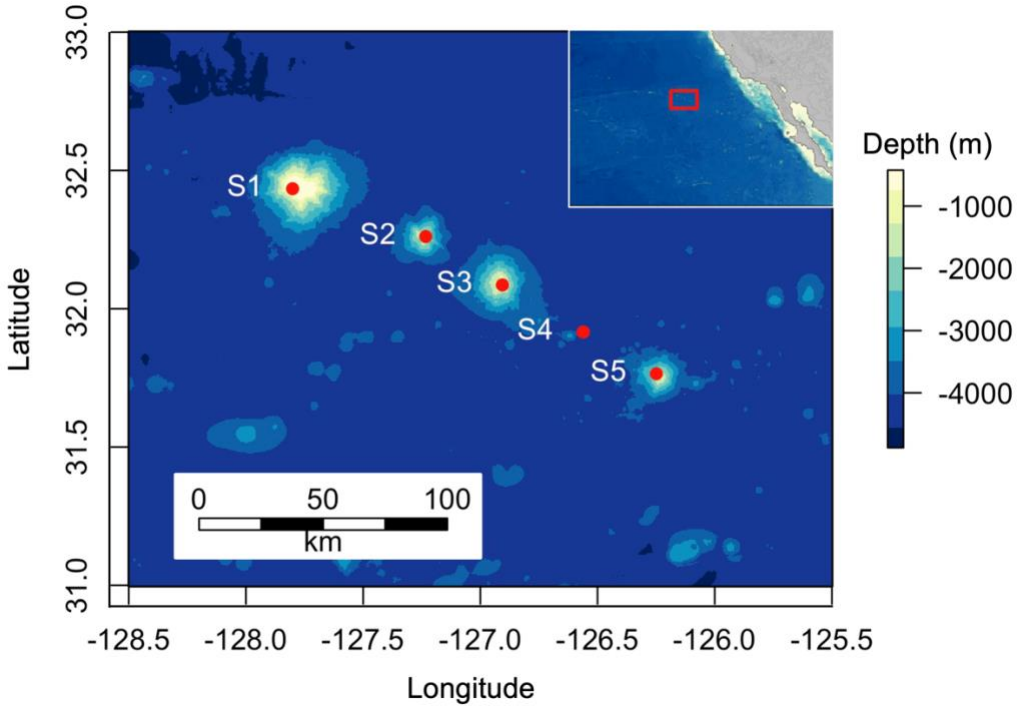

Figure 1. Locations of sampling sites S1–S5 in the Eastern Pacific. Bathymetry is from the global multiresolution topography (GMRT) synthesis (Ryan 2009).

Sampling was conducted using Niskin bottles attached to a conductivity-temperature-depth (CTD) rosette sampling system at five sites along the seamount chain, including one deep water site (Table 1). Continuous measurements of water temperature, salinity, and oxygen concentrations were recorded during each cast using a Sea-bird Electronics 911plus CTD (Fig. 2, Supporting Information 1.1). Continuous transmission measurements were recorded using a C-Star Transmissometer (Supporting Information 1.1).

Table 1. Sampling locations and depths. In total, 54 samples were collected across 5 sites.

Site	**Latitude**	**Longitude**	**Seamount**	**Maximum water depth (m)**	**Water depths sampled (m)**
S1	32.434 N	127.801 W	Fieberling	544	50, 100, 150, 200, 300, 400, 500
S2	32.261 N	127.233 W	Fieberling 2	1407	50, 100, 150, 200, 300, 400, 500, 750, 1000, 1250,1400
S3	32.086 N	126.906 W	Hoke	1044	50, 100, 150, 200, 300, 400, 500, 750, 1000
S4	31.916 N	126.561 W	N/A	4274	50, 100, 150, 200, 300, 400, 500, 750, 1000, 1250, 1500, 2000, 2500, 3000, 3500, 4000, 4200
S5	31.765 N	126.249 W	Stoddard	1579	50, 100, 150, 200, 300, 500, 750, 1000, 1250, 1500

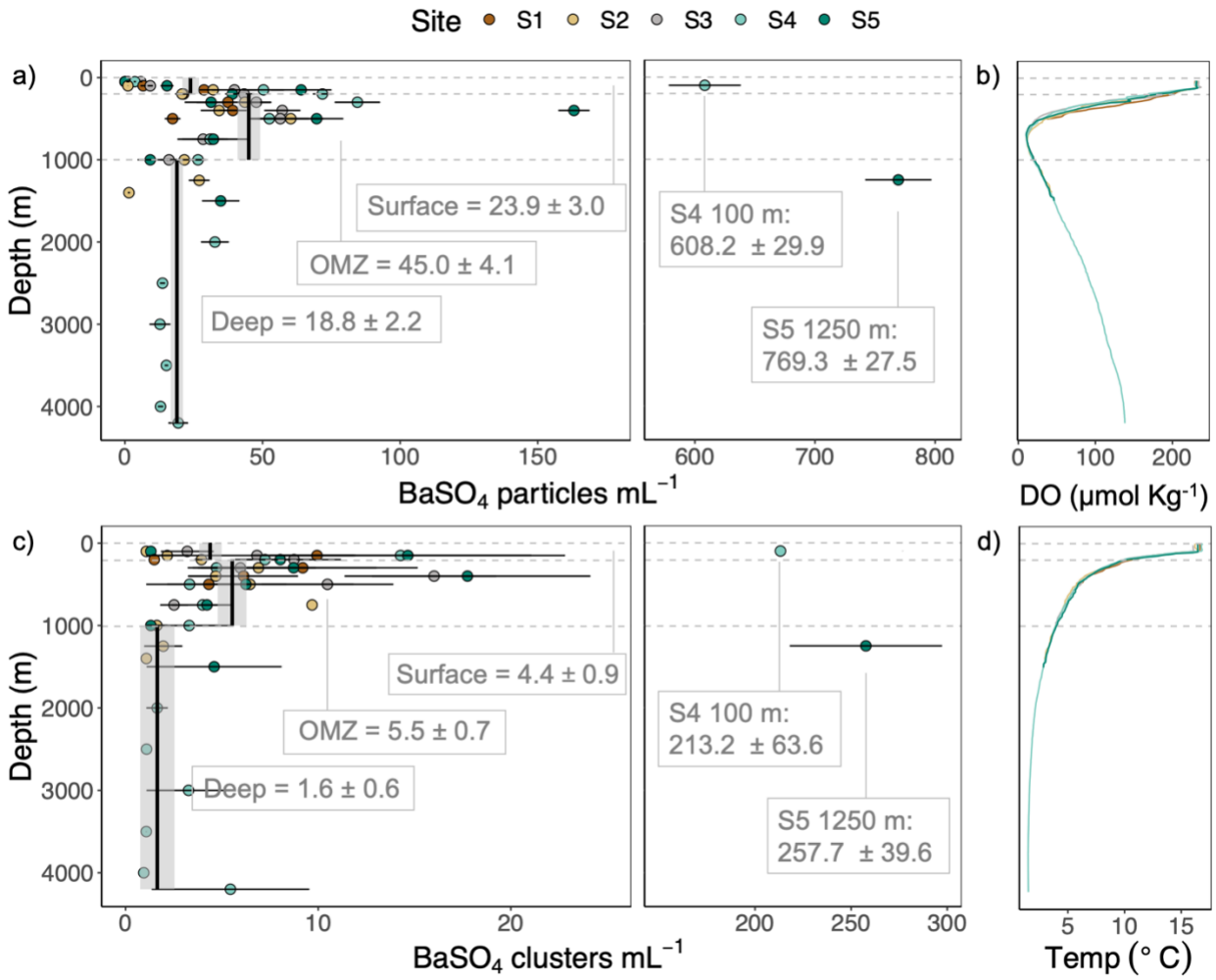

Figure 2. (A) Abundances of all barite microcrystals, (B) dissolved oxygen concentrations, (C) abundances of clusters of adjoined barite microcrystals, and (D) temperature with depth in the water column. Abundance points indicate average abundance ± standard error across the three filter fields analyzed for each sampling depth and site. Vertical lines and text labels indicate average abundance ± standard error for each water layer. Outlying abundance values ± standard error are shown in the middle panel. Dissolved oxygen and temperature profiles were acquired during CTD down casts and were smoothed via boxcar averaging with a step size of 10 m.

Seawater from each depth was sampled via Niskin bottle spigot and sequentially filtered to collect suspended particulate matter. Seawater (3–5 L) was filtered through polycarbonate filters with a diameter of 47 mm and a pore diameter of 12 μm. Subsamples of coarsely filtered water (1–2 L) were then filtered through polycarbonate filters with a diameter of 47 mm and a pore diameter of 0.22 μm. All filters were rinsed with 30 mL of deionized water to remove salts.

Filters were dried in a fume hood and stored in airtight sample bags until later analysis. Filtration of all samples was completed within 6 h of collection.

Barite analysis

Barite microcrystals on each filter with 0.22-μm pores were imaged via scanning electron microscopy equipped with energy-dispersive X-ray spectroscopy (SEM-EDS). Approximately one quarter of each filter was mounted on an aluminum stub with carbon tape for analysis. Analyses were conducted on a Phenom Desktop SEM with an accelerating voltage of 15 kV, vacuum of 1 Pa, and working distance of 9–10 mm. For each filter sample, a random number generator was used to randomly select a field (0.65–0.81 mm^2 in area) for analysis. A backscatter electron detector was used to systematically identify all potential barite microcrystals within the field by their high atomic number. Identification was confirmed by EDS, and all barite microcrystals were imaged. Additional point(s) were analyzed as necessary to determine if microcrystals were associated with organic matter substrates, which appeared visually distinct from the flat surface of the polycarbonate filter. This process was repeated for two additional randomly selected fields for each filter. Smaller areas (0.2–0.4 mm^2) were analyzed for two filters with extremely high barite microcrystal densities (S4 100 m and S5 1250 m). A total of 5481 barite microcrystals were imaged from 54 bottles sampled at 5 sites.

Images were quantitatively analyzed using the FIJI distribution of ImageJ (Schindelin 2012; Schindelin et al. 2015). Scaling parameters were extracted from the metadata of each image. Barite particles were distinguished from the filter background and surrounding particles using the Trainable Weka Segmentation plugin (Arganda-Carreras et al. 2017). The

resulting binary image was smoothed to retain 10% of available Fourier descriptors using the Shape Smoothing plugin. Barite microcrystal abundance for each field was calculated as follows:

$$A_b = \frac{n_b * A_f}{A_a * V}$$

where A_b is barite microcrystal abundance, n_b is number of barite particles observed in a given field, A_f is area of the filter, A_a is area of the field analyzed, and V is the volume of seawater filtered through the corresponding filter. Area, solidity, aspect ratio, and circularity were calculated for each smoothed particle using the ImageJ's Analyze Particle plugin (Supporting Information 1.2-1.5). Solidity was calculated as a quantitative measure of morphology—specifically of the regularity of the outline of each microcrystal—according to the equation:

$$S = \frac{A}{A_C}$$

where S is solidity, A is the area of the particle, and A_C is the area of the convex hull, or the smallest convex polygon that encloses the particle's outline (Supporting Information 1.2). Images were also visually analyzed to determine if each barite microcrystal was associated with organic matter and/or occurred in a cluster with other barite microcrystals. Barite particles greater than 8 μm in diameter were identified as potentially hydrothermal in origin and excluded from statistical analyses.

Statistical analyses

The abundance and features of barite microcrystals were statistically compared for three layers in the water column: surface (0–200 m), OMZ (201–1000 m), and deep (> 1001 m). These layers were consistent with observed O_2 profiles during sampling (Supporting Information 1.1). We calculated barite particle and microcrystal cluster loss from the OMZ to the deep water layer according to the equation:

$$L = 1 - \frac{A_{Deep}}{A_{OMZ}}$$

where L is loss, A_{Deep} is the abundance of barite particles/clusters in the deep water layer, and A_{OMZ} is the abundance of barite particles/clusters in the OMZ layer. One-way ANOVAs with a posteriori Tukey's honestly significant difference (HSD) tests were used to compare barite microcrystal abundance and microcrystal cluster abundance between layers, treating layer as a fixed variable and filter as a random variable. Filters S4 100 m and S5 1250 m were identified as statistical outliers according the protocol described by Zuur et al. (2010) and thus excluded from abundance statistics.

One-way ANOVAs with a posteriori Tukey's HSD tests were used to compare microcrystal area and solidity per particle between layers. Two-way ANOVAs were conducted to examine the interaction of association with organic matter and layer on particle area and solidity. Post hoc simple effects comparisons were conducted to determine the influence of association with organic matter on area and solidity within each layer. A chi-squared test of independence was used to compare frequency of organic matter association between clusters and individual particles. Abundance values were square root transformed and area and solidity values were log transformed for all statistical analyses to meet assumptions of normality and homogeneity of variances.

All analyses were performed in R: A Language and Environment for Statistical Computing, Version 3.6.3 (R Core Team 2020). Tidyverse was used for data processing (Wickham et al. 2019), lme4 was used to fit linear mixed effects models for statistical analyses (Bates et al. 2015), and ggplot2 was used for data visualization (Wickham 2016).

Results

Barite microcrystal abundance and size

Barite microcrystal abundance increased rapidly between the surface and ~ 500 m depth before steadily decreasing until ~ 1000 m depth (Fig. 2A). Barite microcrystal abundance was higher in the OMZ (45.0 ± 4.1 particles mL^{-1}) than in the surface (23.9 ± 3.0 particles mL^{-1}) or deep (18.8 ± 2.2 particles mL^{-1}) water layers ($p = 0.004$, Fig. 2A). Barite was observed on 52 out of 54 filters analyzed; only filters S1 50 m and S5 50 m contained no visible microcrystals in the fields randomly selected for analysis.

Of 5481 barite particles imaged, 971 were present as clusters of submicron barite microcrystals (e.g., Fig. 3D,K). Clusters were observed on 48 out of 54 filters analyzed. The distribution of microcrystal clusters largely mirrored that of barite particles as a whole (Fig. 2B). Cluster abundance was higher in surface (4.4 ± 0.9 clusters mL^{-1}) and OMZ (5.5 ± 0.7 clusters mL^{-1}) layers than in the deep (1.6 ± 0.6 clusters mL^{-1}) layer ($p = 0.036$, Fig. 2B).

Figure 3. Representative barite microcrystals displaying a range of morphologies. (A) Large, platy barite microcrystal potentially hydrothermal in origin. (B) Barrel-shaped barite microcrystal in association with organic matter. (C) Barrel-shaped barite microcrystal displaying etch pits and signs of dissolution. (D) Cluster of submicron, barrel-shaped barite microcrystals. (E) Barrel-shaped barite microcrystal. (F) Circular barite microcrystal. (G) Hexagonal barite microcrystal. (H) Double-headed arrow barite microcrystal showing signs of dissolution along edges. (I) Irregularly shaped barite microcrystal. (J) Irregularly shaped barite microcrystal in association with organic matter. (K) Cluster of submicron barite microcrystals with diverse morphologies and sizes. (L) Hexagonal barite microcrystal with an etch pit in the center.

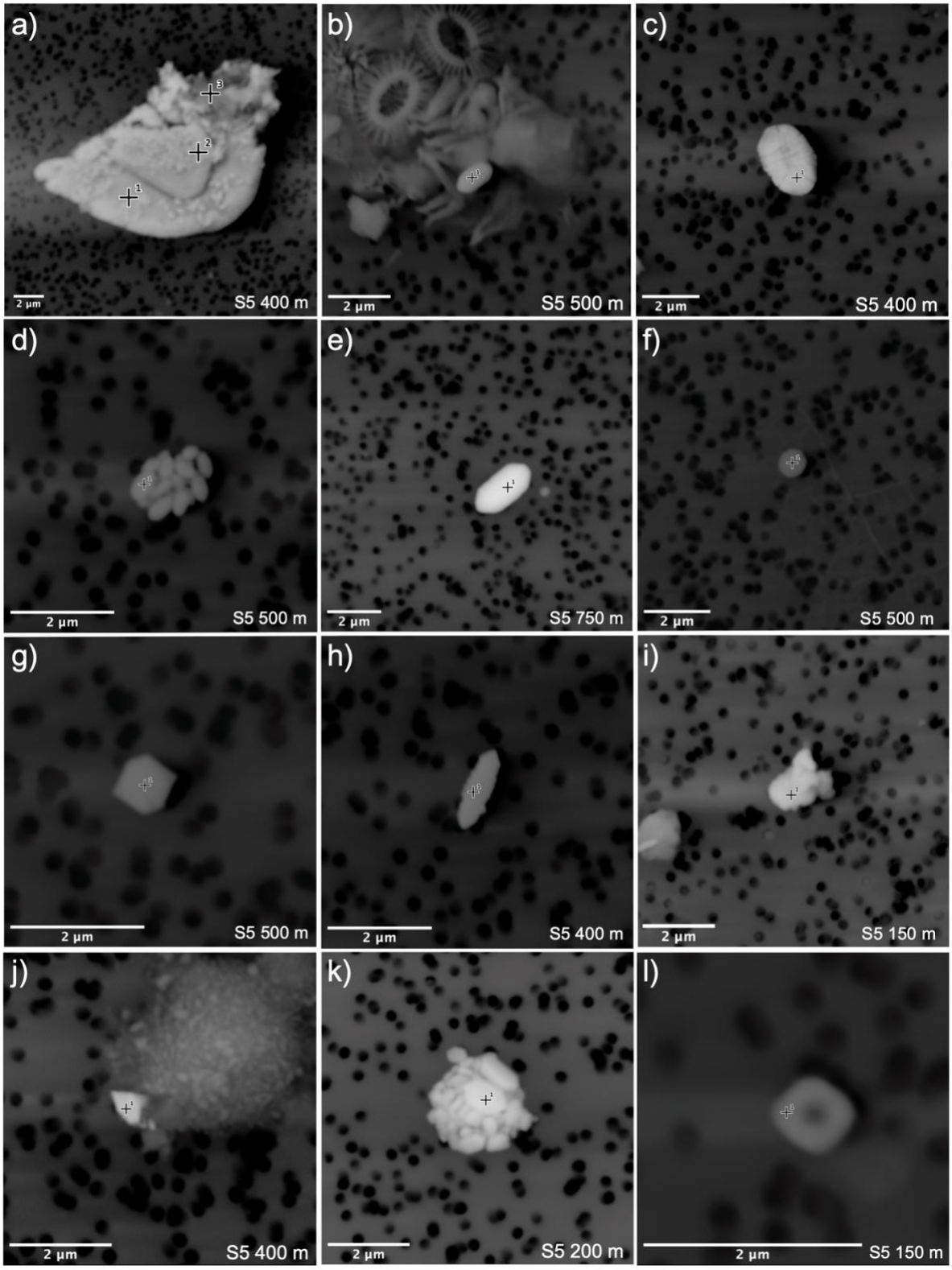
a)
2 µm
S5 400 m
b)
2 µm
S5 500 m
c)
2 µm
S5 400 m
d)
2 µm
S5 500 m
e)
2 µm
S5 750 m
f)
2 µm
S5 500 m
g)
2 µm
S5 500 m
h)
2 µm
S5 400 m
i)
2 µm
S5 150 m
j)
2 µm
S5 400 m
k)
2 µm
S5 200 m
l)
2 µm
S5 150 m

Barite microcrystal abundance was more than 3 times higher and microcrystal cluster abundance was more than 10 times higher for filters S4 100 m and S5 1250 m than for any other filter (Fig. 2). With the exception of these outliers, microcrystal and microcrystal cluster abundance patterns were similar across all five sites.

Most barite microcrystals were between 0.25 and 1.75 μm in length (Supporting Information 1.3). Barite microcrystals were larger in the OMZ (0.90 ± 0.03 μm^2) than in surface (0.81 ± 0.03 μm^2) or deep (0.74 ± 0.04 μm^2) layers ($p = 0.002$, Fig. 4). Average barite microcrystal size increased below 3000 m (1.12 ± 0.10 μm^2), but relatively few ($n = 183$) microcrystals were analyzed for these depths. There was a significant interaction between layer and association with organic matter on microcrystal size ($p < 0.001$, Fig. 5A). In post hoc comparisons, particles associated with organic matter were smaller than particles not associated with organic matter in surface ($p < 0.001$) and OMZ layers ($p < 0.001$), but no significant difference was observed in the deep layer (Fig. 5A). Clusters of barite microcrystals were ~ 50% larger by area than individual barite particles, but since each cluster contained from at least 4 to more than 20 microcrystals, microcrystals within clusters were, on average, much smaller than barite particles that were not in clusters (Fig. 3). No systematic differences in barite microcrystal area were observed between sites.

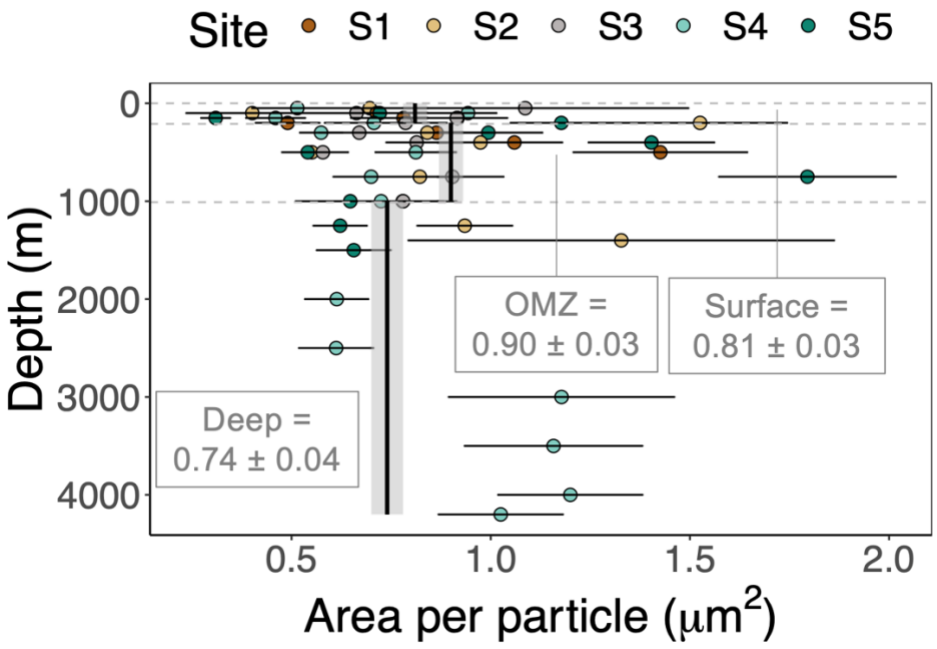

Figure 4. Average particle area per barite microcrystal by depth and site. Points indicate average area ± standard error for each sampling depth and site. Vertical lines and shading indicate average abundance ± standard error for each water layer.

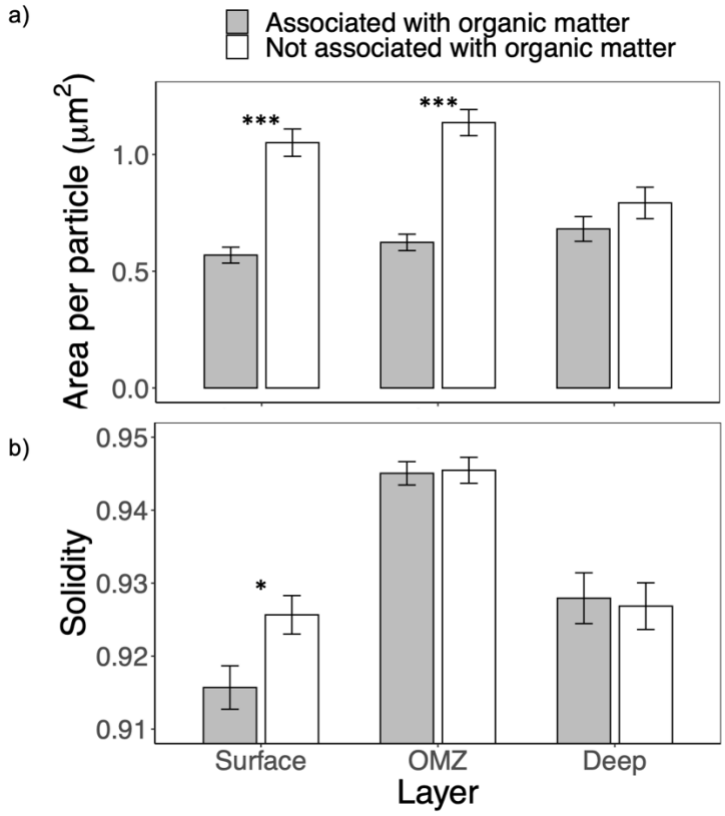

Figure 5. Average (A) area and (B) solidity for barite microcrystals that were and were not associated with organic matter in each water column layer. Error bars display standard error. N = 1325, 2389, and 718 for surface, OMZ, and deep water layers, respectively. Asterisks indicate significant differences within water layers, $*p < 0.05$ and $***p < 0.001$.

Five barite microcrystals had diameters greater than 8 μm and were thus characterized as potentially hydrothermal in origin. These five microcrystals resembled the hydrothermal barite particles displayed in Paytan et al. 2002 and exhibited platy morphologies visually distinct from the other barite microcrystals observed in the water column (e.g., Fig. 3A). Two of these likely hydrothermal barite particles were from S4 100 m water depth, two were from S5 400 m water depth, and one was from S5 1250 m water depth.

Barite microcrystal morphology

A wide range of barite morphologies were observed across all five study sites (Fig. 3, Supporting Information S3). Most microcrystals were ovoid or barrel shaped (e.g., Fig. 3B–E),

but many microcrystals also displayed rectangular or hexagonal morphologies (e.g., Fig. 3G). Several circular (e.g., Fig. 3F) and double-headed arrow (e.g., Fig. 3H) morphologies were also observed. Many microcrystals also displayed irregular or amorphous morphologies (e.g., Fig. 3I,J). Most microcrystal clusters contained microcrystals displaying similar sizes and morphologies within the cluster (e.g., Fig. 3D), but some displayed more heterogeneous microcrystal sizes (e.g., Fig. 3K). Nearly 50% of particles were visibly associated with organic matter substrates (e.g., Fig. 3B,J). There was no significant difference in association with organic matter between individual microcrystal and microcrystal clusters. Approximately, 10% of microcrystals (e.g., Fig. 3C,L) displayed visible signs of dissolution such as etch pits or inner cavities (Dunn et al. 1999).

Microcrystal solidity ranged from 0.5 to 1, which means that particle outlines ranged from very concave and irregular to perfectly solid, such as in the case of a perfect ellipse or polygon. Barite microcrystals displayed higher solidity, or had more regularly shaped outlines, in the OMZ (0.921 ± 0.002) than in surface (0.945 ± 0.001) or deep (0.927 ± 0.002) layers ($p < 0.001$, Fig. 4). There was a significant interaction between layer and association with organic matter on microcrystal solidity ($p = 0.039$, Fig. 5B). In post hoc comparisons, particles associated with organic matter displayed lower solidity than particles not associated with organic matter in the surface layer ($p = 0.012$), but no significant difference was observed in OMZ and deep layers (Fig. 5A). No systematic differences in solidity were observed between sites.

Discussion

Potential allogenic barite sources

The distinctive morphology and relatively large size of five barite microcrystals suggest that they are in a different class than the authigenic marine barite microcrystals that dominate our

sample, and for this reason we excluded them from our statistical analyses. Nonetheless, the origins of these microcrystals are speculative given the local nature of our sample set, and hence we can only suggest possible sources. First, the large microcrystals may have come from a hydrothermal source north of the study region. Our samples were collected in the western limb of the California Current, where flow is to the southeast with a mean velocity of 3–5 cm s^{-1} (Centurioni et al. 2008). Since there is no known near-surface source area for hydrothermal barite to the northwest of our study area, the microcrystals may have been advected offshore by coastal jets within the California Current System (Centurioni et al. 2008; Matthews and Emery 2009). The nearest-known active hydrothermal vents (Beaulieu and Szafrański 2020) are, respectively, 800 km to the east and 1000 km to the north of Study Sites S4 and S5, raising the possibility of long distance, offshore transport.

A second possibility is that these particles may be diagenetic barite locally derived by advection off the tops or flanks of the Fieberling Seamount chain. However, we consider a local source unlikely because the unusually large barite microcrystals were distributed throughout the water column and the CTD profiles we collected with our bottle casts suggest that localized upwelling was not occurring during our cruise (Fig. 2, Supplementary Information 1.1). A third possibility is that the large barite microcrystals might reach our site via dust transport from the Southwestern deserts; Santa Ana winds transport large amounts of dust and soot offshore into the Eastern Pacific (e.g., Jardine et al. 2021). This possible origin is made more plausible by observations that the large barite microcrystals are on the small end of the grain-size spectrum for loess deposited on the Channel Islands, where the mean grain size is about 35 μm (Muhls et al. 2007). In addition, authigenic barite is observed in paleosols in Southern Nevada (Brock-Hon

et al. 2012; Robins et al. 2012). However, barite has not been reported in loess from the California deserts or islands, suggesting that if it is present, it is a rare accessory mineral.

Barite precipitation in organic matter aggregates

Barite microcrystal abundance patterns provide evidence for barite precipitation in association with organic matter remineralization (Fig. 2). The rapid increase in barite microcrystal abundance between the surface and 500 m depth is consistent with carbon remineralization rate profiles in the Eastern Pacific (Feely et al. 2004). These mesopelagic increases in microcrystal abundance are consistent with mesopelagic particulate Ba peaks reported in previously studies (Dehairs et al. 1980, 1991; Martinez-Ruiz et al. 2020) and implied by dissolved Ba and Ba isotope profiles (Horner et al. 2015; Hsieh and Henderson 2017; Bridgestock et al. 2018). The presence of barite microcrystals at all sample sites below 50 m depth also indicates that widespread authigenic barite precipitation begins in the euphotic zone, as does organic matter remineralization (Abell et al. 2000).

Barite microcrystal area and solidity data also highlight the link between organic matter aggregates and barite precipitation. Marine barite particles are thought to begin as amorphous precursors and precipitate toward more regularly shaped microcrystals (Martinez-Ruiz et al. 2019). Thus, the small size and low solidity of microcrystals observed in association with organic matter substrates compared to free crystals suggest that crystals within aggregates represent snapshots of ongoing barite precipitation (Fig. 5). The microenvironments created by these aggregates likely facilitate precipitation toward larger microcrystals with more regular, that is, solid, morphologies. Disintegration of these aggregates over time then leaves behind barite microcrystals not associated with organic matter. Ongoing precipitation toward larger, more solid particles also helps explain crystal solidity and area patterns with depth; microcrystals were

smaller and less solid in surface waters relative to more mature barite microcrystals in the OMZ (Figs. 4 and 6).

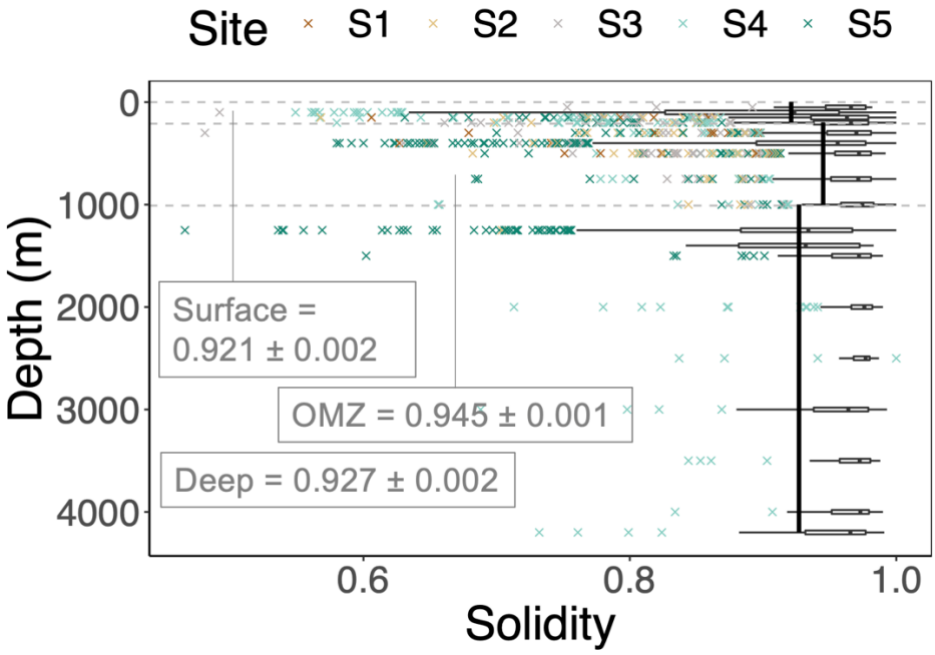

Figure 6. Solidity for single barite microcrystals by depth. Box plots display the median and first and third quartiles, whiskers display higher and lower values to the 1.5× interquartile range, and points display outlying values. Vertical lines and text labels indicate average abundance ± standard error for each water layer.

Together, these findings constitute novel lines of evidence for recently proposed pathways for barite precipitation. While precise characterization of the organic matter substrates observed here is outside the scope of this study, our extensive observations of barite microcrystals associated with organic matter are consistent with the proposed link between barite precipitation and EPS suggested by Martinez-Ruiz et al. (2019). Our findings of ongoing precipitation toward more solid barite microcrystals may also be evidence of barite precipitation via sulfate substitution for phosphate in amorphous Ba-rich intermediaries (Martinez-Ruiz et

al. 2018). A range in crystal shapes during early crystallization may also explain the wide range in morphologies we observed among barite microcrystals (Fig. 3, Supporting Information 1.3).

Water column barite dissolution dynamics

Barite microcrystal abundance profiles indicate an increase in water column barite dissolution relative to precipitation between depths of 500 and 1000 m (Fig. 2). The falloff in barite abundance between the OMZ and the ocean interior below 1000 m is consistent with 60% ± 20% loss by dissolution for all barite particles and 70% ± 40% loss for microcrystal clusters in particular. This decline may reflect an absolute increase in barite dissolution below 500 m. Alternatively, since organic matter remineralization is expected to decrease below depths of 500 m, this decline in barite microcrystal abundance may be the result of fairly consistent rates of barite dissolution in the upper 1000 m accompanied with a decrease in barite precipitation below 500 m.

Microcrystal size and morphology are consistent with water column barite dissolution, particularly in the lower OMZ. Barite microcrystals were smaller and less solid in deep water relative to the OMZ (Figs. 4 and 6). We also observed qualitative evidence of barite microcrystal dissolution in the form of etching and dissolution pits, similar to that reported by Sun et al. (2015), in approximately 10% of barite microcrystals analyzed throughout the water column (Fig. 3).

The abundance of marine barite microcrystals appears to be fairly constant below 1000 m in depth, which suggests that rates of barite dissolution are relatively low in deep waters (Fig. 2). This may be partly due to the shielding of barite microcrystals from dissolution by organic matter aggregates. Microcrystals that are associated with organic matter are smaller and less solid than microcrystals that are not associated with organic matter in the surface layer (Fig. 5).

However, in the deep layer mean area and solidity are equivalent for microcrystals that are and are not associated with organic matter (Fig. 5). In the case of microcrystal area, this convergence is largely driven by a reduction in area for microcrystals that are not associated with organic matter. This suggests that dissolution is less pronounced within the microenvironments made by flocs of sinking organic matter. This organic matter shielding effect likely occurs throughout the water column, but its importance for marine barite cycling is most pronounced in deep waters, where barite microcrystal abundances are low. The shielding effect of organic matter aggregates may also play a significant role in facilitating barite preservation long enough to reach marine sediments.

The size distribution of the water column barite microcrystals we analyzed here was skewed toward smaller particles relative to the barite microcrystal size distribution reported for Central North Pacific marine sediment in Robin et al. 2003. This likely indicates that most submicron barite microcrystals in the water column dissolve at the sediment sediment–water interface before incorporation into the sediment record. The increase we observed in average barite microcrystal size below 3000 m depth may similarly indicate the complete dissolution of smaller barite microcrystals in the deep water column (Fig. 4). However, we did not observe a continued decrease in microcrystal abundance at these depths, and significant deep-water precipitation to offset dissolution and maintain constant barite abundances is unlikely because of continued destruction of sinking organic flocs.

Barite microcrystal clusters

The prevalence of submicron barite microcrystal clusters suggests that clusters may provide clues to authigenic barite formation mechanisms. Barite clusters imply that relatively large numbers of distinct barite nucleation points can exist in close proximity to one another

within organic matter aggregates. The formation of larger barite microcrystals may be impeded by growth competition within microcrystal clusters, as has been shown to occur when other minerals precipitate from multiple nucleation sites in close proximity to one another (e.g., Yang et al. 2014). Moreover, the range of microcrystal size and shape within some clusters (e.g., Fig. 3K) implies that a range of barite precipitation rates can occur within individual organic matter aggregates. This points to the complexity of barite precipitation mechanisms and the likelihood of Ba-rich intermediary phases.

Submicron microcrystal clusters themselves could serve as precursors to larger barite particles. Clusters are particularly abundant in the surface layer and on filters with very high barite microcrystal abundance (Fig. 2), which suggests that clusters may form early in the barite precipitation process. In addition, the combination of submicron microcrystals into larger particles may explain the irregularly shaped barite microcrystals observed here (e.g. Fig. 3I,J) and described in other studies (Dehairs et al. 1980; Sun et al. 2015). However, we find that microcrystal clusters were not significantly more likely to be associated with organic matter than individual particles. Since our other data indicate that microcrystals within organic matter aggregates represent snapshots of ongoing barite precipitation, this undermines the hypothesis of microcrystal clusters as precursors of larger particles. Further research is needed to determine the role submicron microcrystal clusters play in the broader context of authigenic barite precipitation.

Spatial variability and authigenic barite hotspots

We did not observe systematic differences in barite microcrystal abundance or properties along the study site transect or between our deep water site and the sites overlying seamounts (Figs. 2, 4, and 6). However, we did observe considerable variability between individual sites

and depths. Downward organic carbon flux is largely driven by relatively large and rare organic matter aggregates (Alldredge and Silver 1988; Honjo et al. 2008). Since barite precipitation is thought to occur in association with organic matter aggregates, it thus follows that barite distribution in the water column is heterogeneous and somewhat stochastic. By sampling small water volumes, our investigation likely captured this spatial heterogeneity.

Two filters in particular, S4 100 m and S5 1250 m, showed exceptionally high barite microcrystal abundances (Fig. 2). Transmission data and other water parameters showed no discontinuities at these depths (Supporting Information 1.1), so these peaks are likely not due to oceanographic perturbations such as sediment advected off the seamounts or hydrographic transitions in water properties at these depths. Rather, they may be remnants of large organic matter aggregates that just happened to be sampled by the Niskin Bottle. Alternatively, these peaks may track events of mass production of organic matter flocs near the surface and their sedimentation into the ocean interior.

The samples with very high barite microcrystal abundance suggest that sediment barite accumulation may be dominated by localized barite precipitation events. Apart from the aforementioned overrepresentation of clusters, microcrystals at these depths were similar to those observed elsewhere in the water column. This suggests that they precipitated through similar mechanisms, but additional research is necessary to constrain the drivers for and implications of barite heterogeneity in the water column.

Conclusions

Our quantitative visual analysis of thousands of barite microcrystals provides a novel line of evidence for authigenic barite precipitation in association with organic matter aggregates and suggests that these aggregates help protect barite microcrystals from dissolution. We can also

quantify the steep loss of barite microcrystals below ~500 m water depth, presumably due to the dissolution of 60% ± 20% of particles formed shallower in the water column. This large-scale data set is the first of its kind and opens up new avenues for research regarding submicron microcrystal clusters and spatial heterogeneity of barite in the water column. While the accumulation rate of barite in marine sediments is a common export production proxy, direct observations of in situ barite microcrystals are limited and significant questions remain regarding the factors that influence marine barite precipitation and preservation, both within the water column and at the sediment–water interface. By providing insight into water column barite dynamics, our findings help contextualize the sediment barite record and serve as a crucial intermediary step in developing Ba sediment proxies to their full potential.

Acknowledgements

Sample collection was funded by the UC Ship Funds Program. T. L. was supported by a Department of Defense National Defense Science and Engineering Fellowship. We thank the science party and crew of Cruise SR 2002 on the RV Sally Ride for their invaluable assistance. We are grateful to Adina Paytan for thoughtful discussion and to three anonymous reviewers whose comments greatly improved our manuscript.

Chapter 1, in full, is a reprint of the material as it appears in "Quantitative visual analysis of marine barite microcrystals: Insights into precipitation and dissolution dynamics," published in Limnology and Oceanography in 2021. T. Light and R. Norris. The dissertation author was the primary investigator and author of this paper.

References

Abell, J., Emerson, S., Renaud, P. 2000. Distributions of TOP, TON and TOC in the North Pacific Subtropical Gyre: Implications for nutrient supply in the surface ocean and remineralization in the upper thermocline. J. Mar. Res. 58, 203–22.

Alldredge, A., Silver, M. 1988. Characteristics, dynamics and significance of marine snow. Prog. Oceanogr. 20, 41–82.

Arganda-Carreras, I., Kaynig, V., Rueden, C., Eliceiri, K., Schindelin, J., Cardona, A., Seung, H. 2017. Trainable Weka Segmentation: A machine learning tool for microscopy pixel classification. Bioinformatics. 33, 2424–26.

Bates, D., Mächler, M., Bolker, B., Walker, S. 2014. lme4: Fitting Linear Mixed-Effects Models Using Lme4.

Beaulieu, S., Szafrański, K. 2020. InterRidge Global Database of Active Submarine Hydrothermal Vent Fields Version 3.4. PANGAEA.

Bertram, M., Cowen, J. 1997. Morphological and compositional evidence for biotic precipitation of marine barite. J. Mar. Res. 55, 577–93.

Bishop, J. 1988. The barite-opal-organic carbon association in oceanic particulate matter. Nature 332, 341.

Bridgestock, L., Hsieh, Y., Porcelli, D., Homoky, W., Bryan, A., Henderson, G. 2018. Controls on the barium isotope compositions of marine sediments. Earth Planet. Sci. Lett. 481, 101–10.

Brock-Hon, A., Robins, C. Buck, B. 2012. Micromorphological investigation of pedogenic barite in Mormon Mesa petrocalcic horizons, Nevada USA: Implication for genesis. Geoderma. 179, 1-8.

Carter, S., Paytan, A., Griffith, E. 2020. Toward an improved understanding of the marine barium cycle and the application of marine barite as a paleoproductivity proxy. Minerals. 10, 421.

Chow, T., Goldberg, E. 1960. On the marine geochemistry of barium. Geochim. Cosmochim. Acta. 20, 192–98.

Centurioni, L., Ohlmann, J., Niiler, P. 2008. Permanent meanders in the California current system. J. Phys. Oceanogr. 38, 1690-1710.

Dehairs, F., Chesselet, R., Jedwab, J. 1980. Discrete suspended particles of barite and the barium cycle in the open ocean. Earth Planet. Sci. Lett. 49, 528–50.

Dehairs, F., Stroobants, N., Goeyens, L. 1991. Suspended barite as a tracer of biological activity in the Southern Ocean. Mar. Chem. 35, 399–410.

DeVries, T., Primeau, F., Deutsch, C. 2012. The sequestration efficiency of the biological pump. Geophys. Res. Lett. 39, L13601.

Dunn, K, Daniel, E., Shuler, P., Chen, H., Tang, Y., Yen, T. 1999. Mechanisms of surface precipitation and dissolution of barite. Colloid. Interf. Sci. 214, 427-437.

Feely, R., Sabine, C., Schlitzer, R., Bullister, J., Mecking, S., Greeley, D. 2004. Oxygen utilization and organic carbon remineralization in the upper water column of the Pacific Ocean. J. Oceanogr. 60, 45–52.

Ganeshram, R., François, R., Commeau, J., Brown-Leger, S. 2003. An experimental investigation of barite formation in seawater. Geochim. Cosmochim. Acta. 67, 2599–2605.

González-Muñoz, M., Fernández-Luque, B., Martínez-Ruiz, F., Ben Chekroun, K., Arias, J. M., Rodríguez-Gallego, M., Martínez-Cañamero, M., de Linares, C., Paytan, A. 2003. Precipitation of barite by Myxococcus xanthus: possible implications for the biogeochemical cycle of barium. Appl. Environ. Microbiol. 69, 5722–5725.

Gonzalez-Muñoz, M., Martinez-Ruiz, F., Morcillo, F., Martin-Ramos, J., Paytan, A. 2012. Precipitation of barite by marine bacteria: a possible mechanism for marine barite formation. Geology. 40, 675–78.

Gottschalk, J., Battaglia, G., Fischer, H., Frölicher, T., Jaccard, S., Jeltsch-Thömmes, A., Joos, F., Köhler, P., Meissner, K. J., Menviel, L., Nehrbass-Ahles, C. 2019. Mechanisms of millennial-scale atmospheric CO_2 change in numerical model simulations. Quat. Sci. Rev. 220, 30–74.

Griffith, E., Paytan, A. 2012. Barite in the ocean – occurrence, geochemistry and palaeoceanographic applications. Sedimentology 59, 1817–35.

Hain, M., Sigman, D., Haug, G. 2014. The biological pump in the past. In H. Holland and K. Turekian (Eds.), Treatise on Geochemistry. Elsevier, Oxford. 485-517.

Honjo, S., Manganini, S., Krishfield, R., Francois, R. 2008. Particulate organic carbon fluxes to the ocean interior and factors controlling the biological pump: a synthesis of global sediment trap programs since 1983. Prog. Oceanogr. 76, 217–85.

Horner, T., Kinsley, C., Nielsen, S. 2015. Barium-isotopic fractionation in seawater mediated by barite cycling and oceanic circulation. Earth Planet. Sci. Lett. 430, 511–22.

Hsieh, Y., Henderson, G. 2017. Barium stable isotopes in the global ocean: tracer of Ba inputs and utilization. Earth Planet. Sci. Lett. 473, 269–78.

Jardine, G., Crocker, A. Bailey, I., Cooper, M., Milton, J., Wilson, P. 2021. The imprint of windblown dust from the North American Southwest on the California Channel Islands and Pacific Ocean sediments. Quat. Sci. Rev. 261, 106934.

Martínez-García, A., Sigman, D., Ren, H., Anderson, R., Straub, M., Hodell, D., Jaccard, S., Eglinton, T., Haug, G. 2014. Iron fertilization of the subantarctic ocean during the last ice age. Science. 343, 1347–50.

Martinez-Ruiz, F., Jroundi, F., Paytan, A., Guerra-Tschuschke, I., del Mar Abad, M., González-Muñoz, M. 2018. Barium bioaccumulation by bacterial biofilms and implications for Ba cycling and use of Ba proxies. Nat. Commun. 9, 1619.

Martinez-Ruiz, F., Paytan, A., Gonzalez-Muñoz, M., Jroundi, F., Abad, M., Lam, P., Bishop, J., Horner, T., Morton, P., Kastner, M. 2019. Barite formation in the ocean: origin of amorphous and crystalline precipitates. Chem. Geol. 511, 441–51.

Martinez-Ruiz, F., Paytan, A., Gonzalez-Muñoz, M., Jroundi, F., Abad, M., Lam, P., Horner, T., Kastner, M. 2020. Barite precipitation on suspended organic matter in the mesopelagic zone. Front. Earth. Sci. 8, 567714.

Matthews, D., Emery, W. 2009. Velocity observations of the California Current derived from satellite imagery. J. Geophys. Res. Oceans. 114, C08001.

Monnin, C., Jeandel, C., Cattaldo, T., Dehairs, F. 1999. The marine barite saturation state of the world's oceans. Mar. Chem. 65, 253–61.

Muhls, D., Budahn, J., Reheis, M., Beann, J., Skipp, G., Fisher, E. 2007. Airborne dust transport to the eastern Pacific Ocean off southern California: Evidence from San Clemente Island. J. Geophys. Res. Atmos. 112, D13.

Paytan, A., Griffith, E. 2007. Marine barite: recorder of variations in ocean export productivity. Deep Sea Res. Part II: Top. Stud. Oceanogr. 54, 687–705.

Paytan, A., Kastner, M. 1996. Benthic Ba fluxes in the central equatorial Pacific, implications for the oceanic Ba cycle. Earth Planet. Sci. Lett. 142, 439–50.

Paytan, A., Mearon, S., Cobb, K., Kastner, M. 2002. Origin of marine barite deposits: Sr and S isotope characterization. Geology. 30, 747–750.

R Core Team. 2020. R: A language and environment for statistical computing. Vienna, Austria: R Foundation for Statistical Computing.

Robin, E., Rabouille, C., Martinez, G., Lefecre, I., Reyss, J., Van Beek, P., Jeandel, C. 2003. Direct barite determination using SEM/EDS-ACC system: implication for constraining barium carriers and barite preservation in marine sediments. Mar. Chem. 82, 289-306.

Robins, C., Brock-Hon, A., Buck, B. 2012. Conceptual mineral genesis models for calcic pendants and petrocalcic horizons, Nevada. Soil Sci. Soc. Am. J. 76, 1887-1903.

Roden, G. 1991. Mesoscale flow and thermohaline structure around Fieberling Seamount. J. Geophys. Res. Oceans. 96, 16653–72.

Ryan, W., Carbotte, S., Coplan, J., O'Hara, S., Melkonian, A., Arko, R., Weissel, R., Ferrini, V., Goodwillie, A., Nitsche, F., Bonczkowski, J., Zemsky, R. 2009. Global multi-resolution topography synthesis. Geochem. Geophys. 10, Q03014.

Schindelin, J., Arganda-Carreras, I., Frise, E., Kaynig, V., Longair, M., Pietzsch, T., Preibisch, S., Rueden, C., Saalfeld, S., Schmid, B. and Tinevez, J.Y. 2012. Fiji: An open-source platform for biological image analysis. Nat. Methods. 9, 676–682.

Schindelin, J., Rueden, C., Hiner, M., Eliceiri, K. 2015. The ImageJ ecosystem: an open platform for biomedical image analysis. Mol. Reprod. Dev. 82, 518–29.

Sun, X., Yang, Z., Fan, D., Li, Y. 2015. Crystals of suspended marine barite in the Eastern Equatorial Pacific: Processes of dissolution and effects on crystal morphology. Chinese J. Oceanol. Limnol. 33, 194–203.

Torres-Crespo, N., Martínez-Ruiz, F., González-Muñoz, M., Bedmar, E., De Lange, G., Jroundi, F. 2015. Role of bacteria in marine barite precipitation: a case study using Mediterranean seawater. Sci. Total Environ. 512, 562–71.

Turekian, K., Tausch, E. 1964. Barium in deep-Sea sediments of the Atlantic Ocean. Nature 201, 696–97.

Wickham, H. 2016. Ggplot2: Elegant graphics for data analysis. New York: Springer-Verlag.

Wickham, H., Averick, M., Bryan, J., Chang, W., D'Agostino McGowan, L., François, R., Grolemund, G., Hayes, A., Henry, L., Hester, J., Kuhn, M. 2019. Welcome to the Tidyverse. J. Open Source Softw. 4, 1686.

Yang, S., Hou, Y., Zhang, B., Yang, X., Zhang, H., Zhao, H., Yang, H. 2014. Precisely controlled heterogeneous nucleation sites for TiO_2 crystal growth. Cryst. Eng. Comm. 16, 7502-7506.

Zuur, A., Ieno, E., Elphick, C. 2010. A protocol for data exploration to avoid common statistical problems. Methods Ecol. Evol. 1, 3–14.

CHAPTER 2. Marine barite morphology as an indicator of biogeochemical conditions within organic matter aggregates

T. Light, F. Martínez Ruiz, and R. Norris

Abstract

Marine barite is commonly used as a proxy to reconstruct past ocean productivity. Its distribution in the water column mirrors organic carbon fluxes since it precipitates within microenvironments in decomposing organic matter aggregates. Barite and barium proxies are therefore used to study various aspects of organic matter remineralization and the marine carbon cycle. Barite naturally occurs in a wide variety of crystal sizes and morphologies, but barite crystals that form in the ocean water column are dominantly 1-2 μm in length and have barrel-shaped morphologies. Here, we conducted a series of laboratory experiments to determine the physical and chemical conditions that yield barite crystals similar to marine barite. We found that barite saturation index, the presence and identity of organic compounds, and experiment duration all exert a strong influence on barite crystal size and morphology. Barrel-shaped, 1 μm length crystals resembling marine barite were produced in experiments with a barite saturation index of 2.5, soy phospholipid concentrations of $\geq$ 50 mg L^{-1}, and experiment durations of $\leq$ 10 minutes. These findings help constrain the plausible biogeochemical conditions within the aggregate microenvironments in which marine barite precipitates. Relatively high experimental concentrations of phospholipids are consistent with the hypothesized involvement of extracellular polymeric substances in marine barite precipitation. Short experiment durations suggest that a favorable saturation state may be short-lived in marine organic matter aggregates. We present detailed mineralogical and crystallographic analyses of the crystals we synthesized to gain insight into barite crystal growth. This work deepens our understanding of the mechanisms

behind marine barite precipitation and sheds light on microscale spatial and temporal dynamics within organic matter aggregates.

Introduction

The association of particulate Ba and particulate organic carbon in the ocean water column has been broadly demonstrated (e.g., Bishop 1988; Dehairs et al. 1980). Since marine barite precipitates mostly within sinking and suspended particulate matter, it can be a useful tool for studying the remineralization of marine organic matter aggregates such as fecal pellets and marine snow (Carter et al. 2020; Yao et al. 2021 and references therein). The gravitational settling of organic particles transports an estimated 7.3×10^{15} g C out of the surface ocean each year (Nowicki et al. 2022), so understanding marine particle dynamics is central to our ability to constrain the global carbon cycle (Hülse et al. 2017). However, studying marine organic matter aggregates, particularly in situ, is logistically challenging. Important questions remain regarding marine organic matter aggregate formation, persistence, and decomposition in the past and present, and this makes it difficult to predict how marine ecosystems will respond to future anthropogenic climate change (Buesseler et al. 2020; Fakhraee et al. 2020; Henson et al. 2022). Ba proxies have the potential to provide new insights into these processes because marine barite is relatively well-preserved in ocean sediments (Bishop 1988; Paytan et al. 1998), and barite abundance in sediments can be fairly easily measured through methods such as sequential leaching (Paytan et al. 1996) or chelating ligand analysis (House and Norris 2020). Sediment barium concentrations can also be easily measured (e.g., Murray and Leinen 1993).

The ocean is largely undersaturated with respect to barite (Monnin et al. 1999), but marine barite has been demonstrated to precipitate in supersaturated microenvironments within decomposing organic matter aggregates (Bishop 1988; Ganeshram et al. 2003). The precise

mechanism behind the formation of these supersaturated microenvironments is still unclear, but recent work suggests that phospholipids contained by the extracellular polymeric substances (EPS) in organic matter aggregates may play an important role in bioaccumulating barium. Barium has been shown to bind to phosphate groups on cell surfaces and within EPS under experimental conditions (Martinez-Ruiz et al. 2018). Similar crystallization pathways have been observed in the ocean water column, where barite is particularly abundant in suspended organic matter at intermediate depths in the mesopelagic zone (Martinez-Ruiz et al. 2020; Martinez-Ruiz et al. 2019). A portion of this barite then accumulates in marine sediments, where it is well-preserved under non sulfate-reducing conditions (e.g., Paytan et al. 1998).

Because marine barite precipitation is closely linked to organic matter decomposition, the accumulation rate of barite in marine sediments is broadly used as a proxy for the export of organic carbon out of the surface ocean (e.g., Carter et al. 2016; Erhardt et al. 2013; Kim et al. 2022; Lowery and Bralower 2022; Ma et al. 2014; Paytan et al. 1996). Barite abundance and barium isotopes within the water column are used as proxies for modern mesopelagic organic carbon remineralization (e.g., Jacquet et al. 2011; Hsieh and Henderson 2017). Sediment marine barite also serves as an archive for past seawater sulfur, oxygen, and strontium isotopes (e.g., Markovic et al. 2016; Paytan et al. 1993; Yao et al. 2020). However, uncertainties in the specifics of marine barite formation often complicate the interpretation of sediment barite records. For instance, periods of high barite accumulation at certain locations following the Cretaceous-Paleogene mass extinction (Lowery and Bralower 2022) or during Eocene hyperthermals (Griffith et al. 2021) may represent increases in carbon export, but they may also be partly due to changes in other ecosystem parameters such as plankton community composition and intensity of organic matter remineralization.

Despite the widespread utility of marine barite proxies, relatively little work has focused on the processes that cause marine barite precipitation and on how marine barite crystal size and morphology can shed light on the organic matter aggregates in which barite forms. Barite naturally occurs in a wide range of sizes and morphologies across different environments (Goldschmidt 1913), but marine barite crystals show distinct morphologies that tend to be barrel-shaped, elliptical, or six-sided and approximately 1 μm in length (Fig. 7) (Bertram and Cowen 1997; Light and Norris 2021; Sun et al. 2015). Previous laboratory investigations into barite precipitation have shown that barite crystal size and morphology is determined by factors such as barite saturation index, Ba^{2+} to SO_4^{2-} ratio, solution mixing protocol, concentration of Na^+ and other cations, and the presence of organic compounds such as sodium formate, ethylenediaminetetraacetic acid (EDTA), benzoic acids, polyacrylic acid, humic acids, and phosphonates (Benton et al. 1993; Bernard-Michel et al. 2002; Fernandez-Diaz et al. 1990; Freeman et al. 2006; Godinho and Stack 2015; Jones and Ogden 2009; Judat and Kind 2004; Kowacz et al. 2007; Ruiz-Agudo et al. 2015; Ruiz-Agudo et al. 2016; Qi et al. 2001; Shen et al. 2007; Smith et al. 2004; Widanagamage et al. 2014; Widanagamage et al. 2018). Crystal nucleation that is homogeneous (in solution) vs. heterogeneous (on surfaces) may also impact barite crystal size and morphology (Deng et al. 2019; He et al. 1995, Yuan et al. 2021). However, most prior studies on barite morphology were not designed to emulate marine environments and did not reliably produce crystals resembling marine barite.

Recent work has shown that barite crystals resembling marine barite can result from a two-step process in which a Ba-P amorphous phase formed with phytic acid is exposed to a sulfate-bearing solution (Ruiz-Agudo 2021). Boon and Jones (2016) investigated the elemental composition of barite crystals formed in synthetic seawater solutions, but the crystals they

produced generally did not resemble marine barite in size or morphology. Rather, marine barite morphologies resemble that of some carbonates resulting from microbially mediated precipitation (Dupraz et al. 2009). In the case of carbonates, mineral species abundance and morphology provides information on the conditions of precipitation such as the nature of the mediating biofilm and concentrations of organic compounds such as polyaspartic acid and other polyamino acids (e.g., Braissant et al. 2003). Thus, barite morphology may shed light on the organic microenvironments in which barite forms in natural settings.

Here, we conducted a wide variety of laboratory experiments to identify conditions that produce marine barite's characteristic size and morphology. We use these findings to constrain plausible biogeochemical conditions within the organic matter aggregate microenvironments in which marine barite precipitates in the ocean water column. We also explore the implications of marine barite morphology for both barite crystal growth and the marine barium cycle.

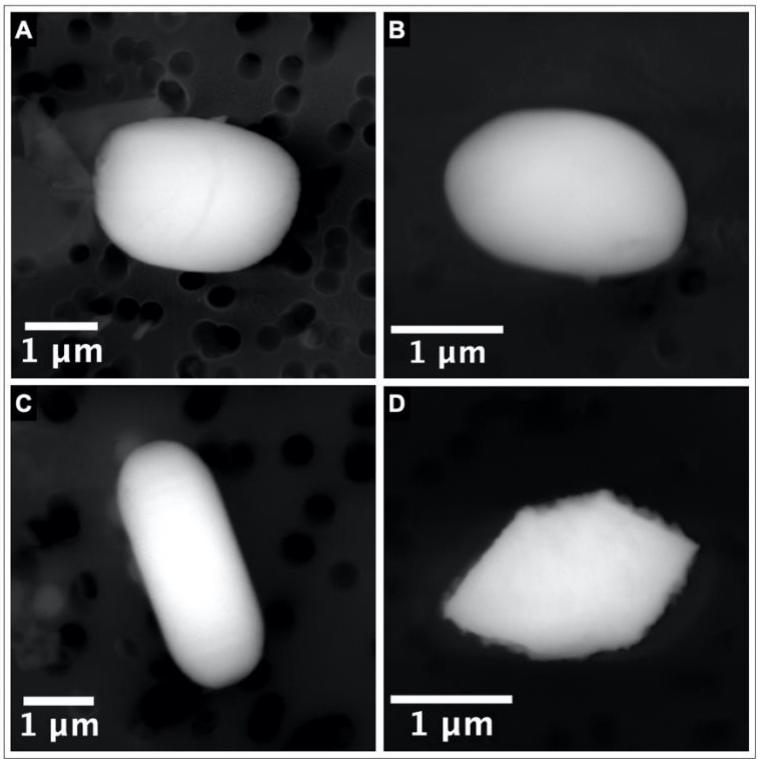

Figure 7. Representative marine barite crystals collected from a water depth of 200 m in the North Pacific. A), B), and C) Typical elliptical or barrel-shaped barite crystals. D) Six-sided barite crystal with irregular edges. See Light and Norris 2021 for detailed information regarding crystal collection and analysis.

Materials and Methods

Barite precipitation protocol

We conducted a series of laboratory experiments to assess the role of barite saturation index, presence and concentration of organic additives, and experiment duration time on barite crystal morphology (Table 2). All solutions were made using ultrapure Milli-Q water (18.2 MΩ·cm). Experiments were designed to simulate the relative concentrations of seawater constituents as closely as possible.

Barite supersaturation was obtained through the addition of barium chloride ($BaCl_2$, Fisher Scientific) and sodium sulfate (Na_2SO4, Fisher Scientific) to maintain a 1:625 $[Ba^{2+}]$:$[SO_4^{2-}]$ ratio, or the ratio achieved when the SO_4^{2-} concentration in solution is equal to that

of seawater and Ba^{2+} is enriched to achieve a saturation index of 2.5 (Emerson and Hedges 2008). Barite saturation indices were calculated using The Geochemist's Workbench software (Bethke 2022). Strontium nitrate ($SrNO_3$, Sigma-Aldrich) was added to each solution to achieve a $[Ba^{2+}]$:$[Sr^{2+}]$ ratio of 1. Sodium chloride (NaCl, Innovating Science) was added to all experiments as necessary to achieve $[Na^+]$ = 460 mM to approximate seawater Na^+ concentrations (Emerson and Hedges 2012). One exception was made for the pyromellitic acid experiment; pyromellitic acid was observed to form a precipitate in the presence of Na^+, so NaCl was not added to this solution and the concentrations of all other species were adjusted accordingly. Additional experiments were conducted to assess the influence of $[Ba^{2+}]$:$[Sr^{2+}]$ and $[Ba^{2+}]$:$[SO_4^{2-}]$ and ratios on barite crystal morphology (Supplementary Information 2.1, 2.2).

We used four organic additives in our experiments: sodium formate (HCOONa), L-ascorbic acid ($C_6H_8O_6$), pyromellitic acid (1,2,4,5-benzenetetracarboxylic acid, $C_{10}H_6O_8$), and EDTA ($C_{10}H_{16}N_2O_8$). These additives were acquired from Sigma-Aldrich, TCI, Sigma-Aldrich, and Eisen-Golden, respectively. Sodium formate was selected because formic acid occurs naturally in seawater (Koyama and Thompson 1964), and sodium formate has been previously shown to produce elliptical barite crystals (Widanagamage et al. 2018). Experiments with L-ascorbic acid were run because it also occurs naturally in seawater (Wangersky 1952) and has been shown to produce spherical calcium carbonate crystals (Saraya 2015). Pyromellitic acid was employed because it has been previously shown to produce elliptical barite crystals (Freeman et al. 2006), and benzoic acids can be used as a proxy for carboxy-rich alicylic molecules, which are a main component of marine dissolved organic matter (Liu et al. 2020). EDTA was used because it has been previously shown to produce elliptical barite crystals, and there is a large body of literature on the interactions between EDTA and barite (e.g., Akyol et al.

2016; Jones et al. 2007; Liu et al. 2018; Widanagamage et al. 2018; Zhang et al. 2011). EDTA also forms complexes with Ba^{2+} ions in solution, so the EDTA experiment was conducted at higher calculated barite supersaturation to compensate for complexed ions (Jones et al. 2007). Soy phospholipids were acquired from Millipore Sigma and contained roughly equal amounts of lecithin, cephalin, and phosphatidylinositol with minor amounts of other phospholipids and polar lipids. Soy phospholipids were used because phospholipids have been hypothesized to play an important role in marine barite precipitation (Martinez-Ruiz et al. 2018, 2019).

Experiments were designed to minimize contamination and high barite saturation indices at the solution mixing interface. All glassware was cleaned in 5% hydrochloric acid overnight. All reactants except Na_2SO_4 were dissolved in 40 ml water in a 200 ml glass beaker. Soy phospholipids were sonicated to dissolution in 5 ml of ethanol before addition to this $BaCl_2$ solution. Na_2SO_4 was separately dissolved in 10 ml of water. The $BaCl_2$ solution was then rapidly stirred on a magnetic stir plate while the Na_2SO_4 solution was slowly added. The final solution was then removed from the stir plate and allowed to sit for the specified time in the experimental treatment. The solution was then syringe filtered through a 0.2 μm pore size, 25 mm diameter nylon membrane filter enclosed in a reusable filter holder. Filters were then dried in a 60°C oven overnight prior to analysis. All experiments were conducted in duplicate.

We initially conducted experiments in polycarbonate plastic bottles, but we found that these bottles retained nuclei of barite crystals through repeated acid washes. These retained nuclei influenced the size and morphology of barite crystals synthesized in later experiments and led to inconsistent results between duplicate experiments. We also pursued many iterations of the solution mixing protocol before we discovered the importance of minimizing high barite saturation indices at the solution mixing interface. These iterations included adding concentrated

$BaCl_2$ to a dilute SO_4^{2-} solution, adding dilute $BaCl_2$ to the Na_2SO_4 solution without stirring, and scaling the experimental protocol up to larger volumes.

Table 2. Experimental parameters, analyses conducted, and resultant barite crystal morphologies. SI is the saturation index, while other experiments focused on varying concentrations of organic additives and experiment duration times. All Soy and Time treatments also contained 9 % v/v ethanol.

Treatment	**$BaSO_4$ SI**	**Organics**	**Time (minutes)**	**Analyses**	**Dominant Crystal Morphology**
SI-1.5	1.5	None	2	SEM	Irregular
SI-2	2	None	2	SEM, HRTEM	Irregular
SI-2.5	2.5	None	2	SEM, HRTEM	Rectangular, rhomboidal
SI-3	3	None	2	SEM	Concave diamond, rosette
SI-3.5	3.5	None	2	SEM	Concave diamond, rosette
Formic	2.5	1 M formic acid	2	SEM, HRTEM	Globular elliptical
Ascorbic	2.5	1 M ascorbic acid	2	SEM, HRTEM	Rectangular, hollow rhomboidal

Table 2. Experimental parameters, analyses conducted, and resultant barite crystal morphologies. SI is the saturation index, while other experiments focused on varying concentrations of organic additives and experiment duration times. All Soy and Time treatments also contained 9 % v/v ethanol. (Continued)

Treatment	**$BaSO_4$ SI**	**Organics**	**Time (minutes)**	**Analyses**	**Dominant Crystal Morphology**
Pyromellitic	2.5	48 mM pyromellitic acid	2	SEM, HRTEM	Elliptical, rhomboidal
EDTA	3	25 mM EDTA	2	SEM, HRTEM	Elliptical
Ethanol	2.5	9 % v/v ethanol	2	SEM	Rectangular, rhomboidal
Soy-10	2.5	10 mg L^{-1} soy phospholipids	2	SEM	Rectangular, rhomboidal, irregular
Soy-50	2.5	50 mg L^{-1} soy phospholipids	2	SEM	Elliptical, irregular
Soy-100	2.5	100 mg L^{-1} soy phospholipids	2	SEM, HRTEM	Elliptical
Soy-200	2.5	200 mg L^{-1} soy phospholipids	2	SEM, HRTEM	Elliptical

Table 2. Experimental parameters, analyses conducted, and resultant barite crystal morphologies. SI is the saturation index, while other experiments focused on varying concentrations of organic additives and experiment duration times. All Soy and Time treatments also contained 9 % v/v ethanol. (Continued)

Treatment	**$BaSO_4$ SI**	**Organics**	**Time (minutes)**	**Analyses**	**Dominant Crystal Morphology**
Time-10	2.5	100 mg L^{-1} soy phospholipids	10	SEM, HRTEM	Elliptical, globular
Time-30	2.5	100 mg L^{-1} soy phospholipids	30	SEM, HRTEM	Globular
Time-120	2.5	100 mg L^{-1} soy phospholipids	120	SEM, HRTEM	Globular

Barite crystal analyses

Morphology assessments of each treatment were conducted via Scanning Electron Microscopy equipped with Energy-dispersive X-ray Spectroscopy (SEM-EDX). One quarter of each nylon membrane filter was mounted on an aluminum stub with carbon tape for analysis. Size analysis and morphological characterization were conducted on a Phenom Desktop SEM with an accelerating voltage of 15 kV and working distance of 9-10 mm (Scripps Institution of Oceanography, UCSD). A backscatter electron (BSE) detector was used to identify likely barite crystals, and their identity was confirmed by EDX. Dominant crystal morphologies for each treatment were determined based on the visual assessment of at least 20 barite crystals on each duplicate filter. Higher-quality images of representative crystals were then acquired using an

AURIGA FIB- FESEM Carl Zeiss SMT microscope equipped with EDX and operated at 10 kV (Centre for Scientific Instrumentation, University of Granada) and a FEI Apreo 2 LoVac SEM equipped with EDX and operated at 20 kV (NanoEngineering Materials Research Center, University of California San Diego). Images were processed using the FIJI distribution of ImageJ (Schindelin et al. 2012; 2015).

Barite crystals from treatments Soy-100, Time-10, Time-30, and Time-120 (with experiment duration times of 2, 10, 30 and 120 minutes, respectively) were quantitatively analyzed to determine the effect of experiment duration on crystal size. Twenty barite crystals for each treatment were randomly selected and imaged during SEM analysis. Images were then analyzed using the FIJI distribution of ImageJ (Schindelin et al. 2012; 2015). Scaling parameters were extracted from the metadata of each image. Barite crystals were distinguished from the filter background using the Trainable Weka Segmentation plugin (Arganda-Carreras et al. 2017). Barite crystal areas were then calculated using FIJI's Analyze Particles plugin. Results were plotted in R using ggplot 2.0 (R Core Team 2020; Wickham 2016).

Eleven of the seventeen experimental treatments were selected for additional analysis via high-resolution transmission electron microscopy (HRTEM) (Table 2). For each of these treatments, one quarter of one duplicate filter was suspended in ethanol and ground with an agate mortar. Particulate matter suspended in this ethanol was then deposited on carbon-film-coated copper grids. Barite crystals on these grids were then imaged using a FEI TITAN G2 60–300 microscope with a high brightness electron gun (X-FEG) operated at 300 kV and equipped with a Cs image corrector CEOS (Center for Scientific Instrumentation, University of Granada). Elemental composition maps were acquired using a SUPER-X silicon-drift windowless EDX detector. Spot EDX spectra were semi-quantitatively analyzed to determine the relative

intensities of phosphorous across soy phospholipid treatments (Supplementary Information 2.3). Selected area electron diffraction (SAED) patterns were also collected on barite crystals. Two to four crystals were imaged for each treatment in which HRTEM analysis was conducted. SAED patterns were quantitatively analyzed using CrysTBox Software (Klinger 2017). Since a greater number of crystals were analyzed via SEM and HRTEM sample preparation preferentially selects for small crystals, SEM was used to determine the dominant crystal morphologies and size distributions for each treatment.

Results

Effect of saturation index on barite morphology

Barite saturation index (SI) had a large effect on observed barite crystal morphology. Barite crystals precipitated in solutions with a barite SI of 1.5 and 2 displayed irregular morphologies and were mostly under 1 μm in length (Figs. 8A, 8B). Barite crystals from solutions of SI 2.5 displayed clearly defined rectangular and rhomboidal morphologies and were 1-3 μm in length (Fig. 8C). Solutions of SI 3 and 3.5 produced crystals with distinctive twinned concave diamond and bladed rosette morphologies ranging from 1 μm to 5 μm in length (Fig. 8D, 8E). These morphologies were consistent with those observed under similar conditions in Godinho and Stack (2015). Solution mixing protocol had a large effect on barite precipitation; in early experiments that did not minimize barite concentration gradients at the solution mixing interface, crystal morphologies typical of SI 3 and 3.5 were observed even in solutions with lower saturation indices. $[Ba^{2+}]$:$[Sr^{2+}]$ had no discernible effect on barite crystal size and morphology within the range of conditions tested here (Supplementary Information 2.1). $[Ba^{2+}]$:$[SO_4^{2-}]$ had little effect on barite crystal size and morphology, but crystals precipitated at very high $[SO_4^{2-}]$ were smaller and displayed rounded corners (Supplementary Information 2.2).

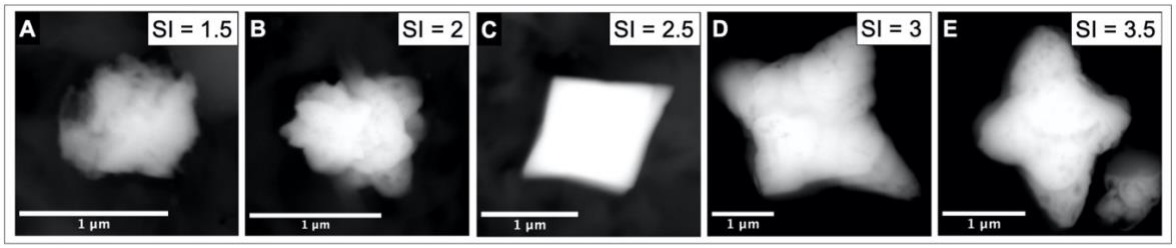

Figure 8. SEM images of representative barite crystal morphologies for treatments A) SI-1.5, B) SI-2, C) SI-2.5, D) SI-3, and E) SI-3.5.

Effect of organic additives on barite morphology

Various organic additives had distinct effects on barite crystal morphology. In experiments with barite saturation of 2.5, formic acid produced crystals with globular, pointed elliptical morphologies, visibly uneven surface textures, and lengths of 1-3 μm (Fig. 9A). Ascorbic acid, with SI = 2.5, produced rectangular and rhomboidal crystals with lengths mostly under 1 μm (Fig. 9B). Approximately half of the rhomboidal crystals contained center holes resembling dissolution pits (Fig. 9B). Pyromellitic acid, with SI = 2.5, produced rectangular and narrow elliptical crystals mostly under 1 μm in length (Fig. 9C). Finally, EDTA (SI = 3) produced broad, elliptical crystals 1-2 μm in length (Fig. 9D).

HRTEM results were generally consistent with SEM observations (Figs. 9E, 9H), but HRTEM images for Ascorbic and Pyromellitic treatments showed more irregular morphologies than those observed during SEM analysis (Figs. 9F, 9G). Elemental composition maps for crystals synthesized in the presence of all four organic additives were consistent with barite (Figs. 9I-L). Lattice-fringe images and SAED patterns for all four treatments yielded d-space measurements consistent with barite (Figs. 9M-T). All four SAED patterns showed well-defined crystallinity, with the Formic treatment displaying some polycrystalline character (Figs. 9N, 9P, 9R).

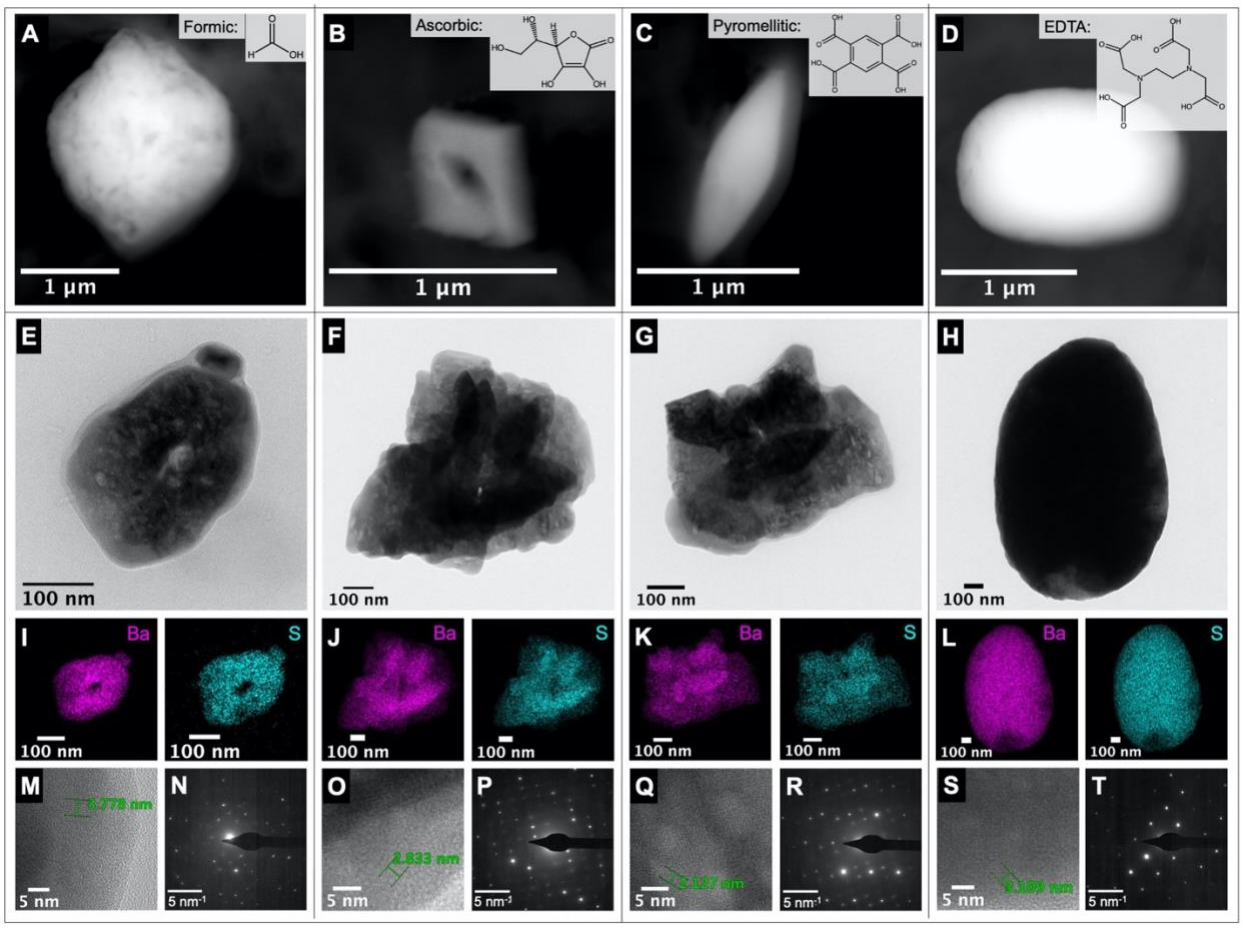

Figure 9. SEM images of representative barite crystal morphologies for treatments A) Formic, B) Ascorbic, C) Pyromellitic, and D) EDTA. Insets depict the chemical structure of the corresponding organic compound. HRTEM images of crystals from E) Formic, F) Ascorbic, G) Pyromellitic, and H) EDTA treatments. Ba and S elemental composition maps of corresponding crystals for I) Formic, J) Ascorbic, K) Pyromellitic, and L) EDTA treatments. Lattice fringe images and SAED patterns for a region of the corresponding crystal for M) and N) Formic, O) and P) Ascorbic, Q) and R) Pyromellitic, and S) and T) EDTA treatments. Lattice-fringe images show d-spacings characteristic of barite: 3.77 Å (201) for M, 2.84 Å (112) for O, 2.12 Å (113) for Q, and 3.10 Å (211) for S. Ten unit cells have been measured, so the indicated measurements in nm correspond to d-spacings in Å.

Effect of soy phospholipids on barite morphology

Barite crystals similar to marine barite formed in the presence of moderately high concentrations of soy phospholipids. Barite crystals precipitated in the presence of only ethanol or ethanol and 10 mg L^{-1} soy phospholipids displayed regular rectangular and rhomboidal

morphologies like those precipitated without soy phospholipids (Figs. 10A, 10B). However, crystals precipitated with ethanol and 50, 100, and 200 mg L^{-1} soy phospholipids displayed largely elliptical morphologies (Figs. 10C-E). Most barite crystals for all four treatments were 1-2 μm in length.

HRTEM analysis of barite in the absence of soy phospholipids confirmed its well-defined euhedral morphology (Fig. 10F). HRTEM analysis of 100 and 200 mg L^{-1} soy phospholipid treatments showed crystals that were broadly elliptical but fairly irregular in shape (Figs. 10L, 4R). Elemental composition maps were consistent with barite (Figs. 10G, 10H, 10M, 10N, 10S, 10T). Crystals from SI-2.5, Soy-100, and Soy-200 treatments showed some phosphorous incorporation into the crystal lattice, but the inclusion of phosphorous did not appear to increase with increasing concentrations of phospholipids in solution (Figs. 10I, 10O, 10U). Semi-quantitative analysis of spot EDX spectra suggest greater incorporation of phosphorous in the Soy-100 treatment than the other two treatments (Supplementary Information 2.3). Lattice-fringe images and SAED patterns for all three treatments showed well-defined crystallinity and yielded d-space measurements consistent with barite (Figs. 10J, 10K, 10P, 10Q, 10V, 10W).

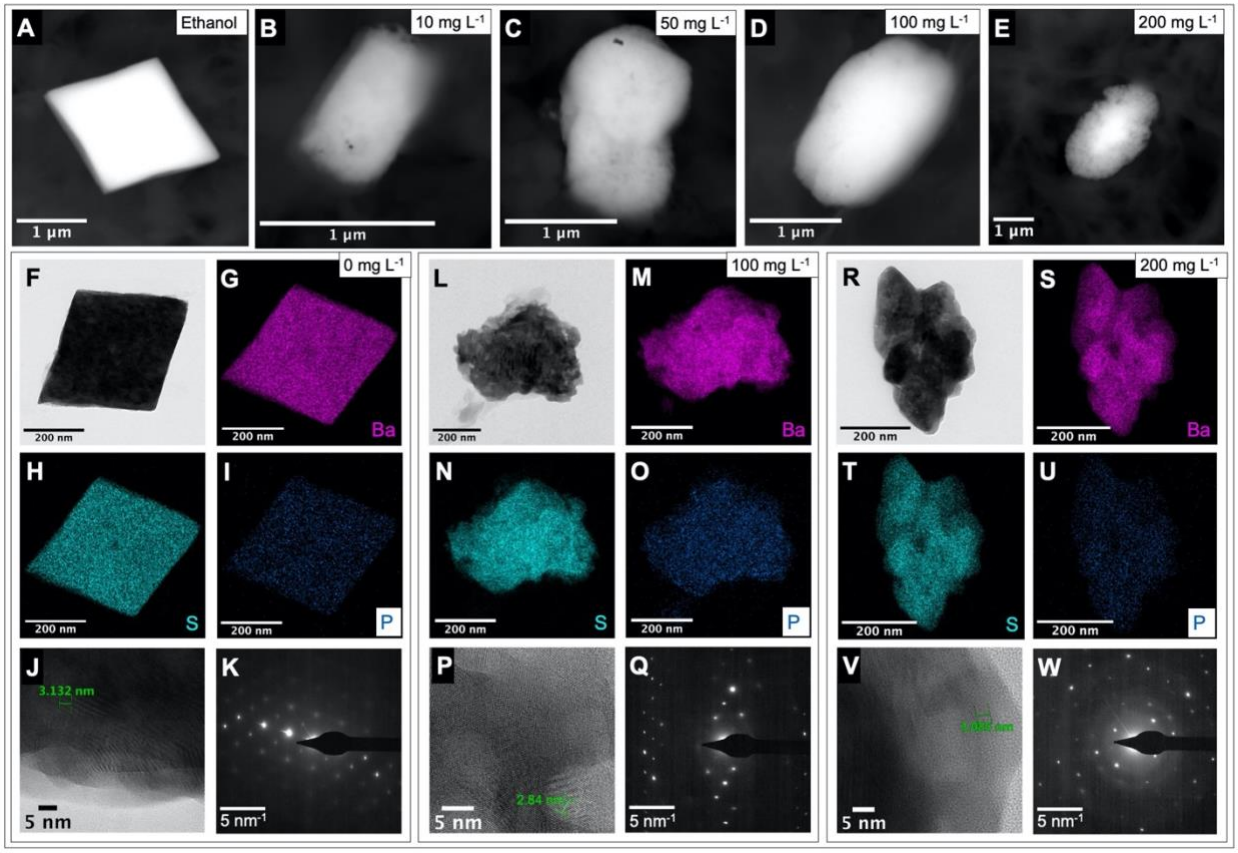

Figure 10. SEM images of representative barite crystal morphologies for treatments A) Ethanol, B) Soy-10, C) Soy-50, D) Soy-100, and E) Soy-200. HRTEM images and corresponding elemental composition maps for treatments F-I) SI-2.5, L-O) Soy-100, and R-U) Soy-200. Lattice-fringe images and SAED patterns for a region of the corresponding crystal for J) and K) SI-2.5, P) and Q) Soy-100, and V) and W) Soy-200 treatments. Lattice-fringe images show d-spacings characteristic of barite: 3.10 Å (211) for J, 2.84 Å (112) for P, and 3.10 Å (211) for V. Ten unit cells have been measured, so the indicated measurements in nm correspond to d-spacings in Å.

Effect of experiment duration on barite morphology

Barite crystals synthesized in the presence of 100 mg L^{-1} soy phospholipids became larger and more irregularly shaped with longer experiment durations (Figs. 11, 12). Crystals in solutions allowed to react for 2 minutes displayed regular elliptical morphologies and had an average length of 0.8 ± 0.1 µm (Figs. 11A, 12). Barite crystals became more globular with increasing experiment duration times and reached average lengths of 2.7 ± 0.4 µm, 15 ± 2 µm,

and 54 ± 8 μm after 10, 30, and 120 minutes, respectively (Figs. 11B-D, 12). D-spacing measurements from lattice-fringe images for crystals from 2-, 10-, and 30-minute treatments are consistent with barite. Lattice-fringe images and SAED patterns showed increasing polycrystallinity with longer experiment durations (Figs. 11E-J).

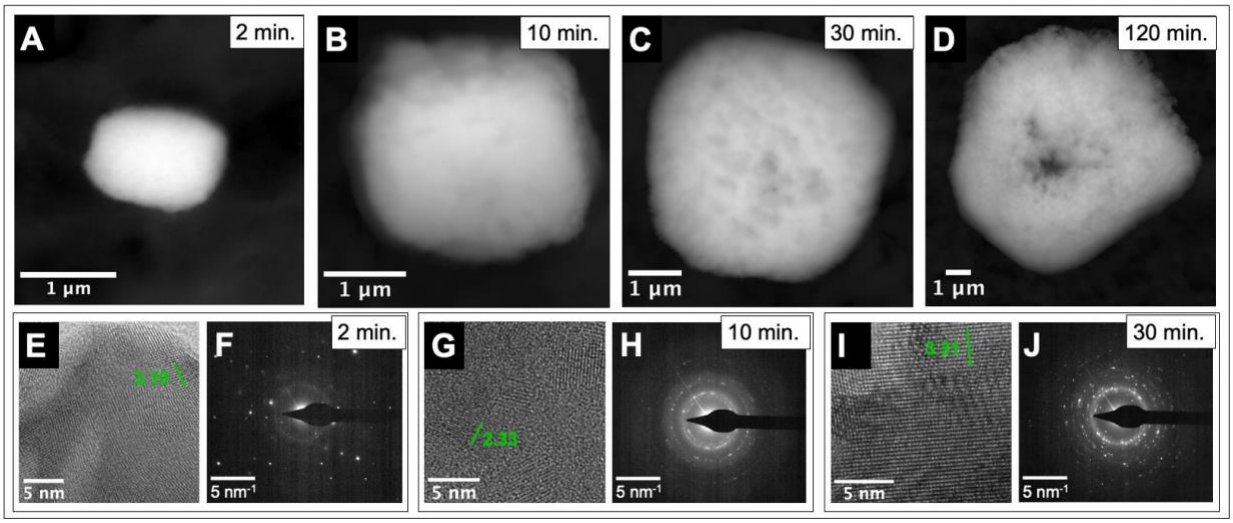

Figure 11. SEM images of representative barite crystal morphologies for treatments A) Soy-100, B) Time-10, C) Time-30, and D) Time-120. Lattice-fringe images and SAED patterns for crystals from treatments E) and F) Soy-100, G) and H) Time-10, and I) and J) Time-30. Lattice-fringe images show d-spacings characteristic of barite: 3.10 Å (211) for E, 2.33 Å (220) for F, and 3.32 Å (102) for G. Ten unit cells have been measured, so the indicated measurements in nm correspond to d-spacings in Å.

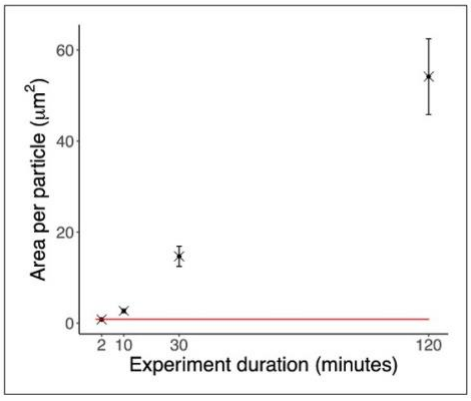

Figure 12. Average barite crystal area with experiment duration. The red line shows average barite crystal area for marine barite crystals collected from the North Pacific (Light and Norris 2021).

Discussion

Barite morphology as an indicator of conditions within organic matter aggregates

Our results show that barite saturation index, the presence of organic compounds, and experiment duration determine barite crystal size and morphology. Since only four out of the seventeen experiments we conducted here yielded barite crystals that resemble characteristic marine barite crystals (Table 2, Fig. 13), we can use our findings to constrain likely biogeochemical conditions in the organic matter aggregate microenvironments in which barite precipitates. Microscale dynamics within organic matter aggregates are poorly constrained, despite the importance of aggregates to marine ecosystems and the marine carbon cycle (Iversen 2023). Therefore, these findings provide new insights into the plausible biogeochemistry of aggregates.

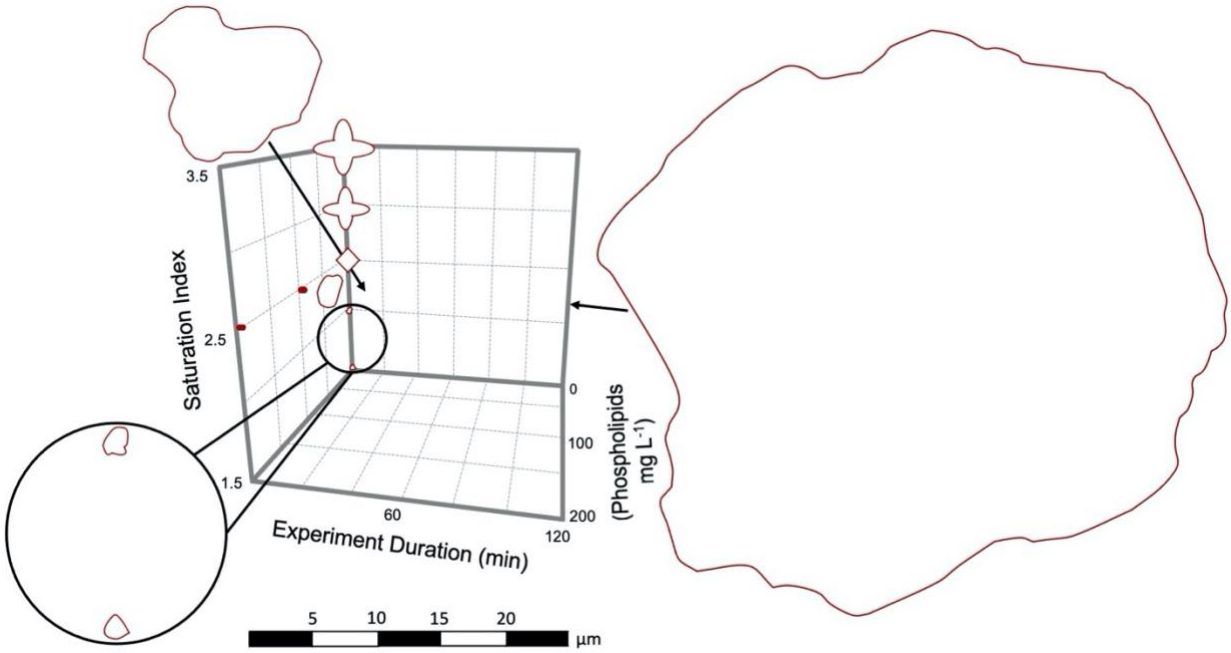

Figure 13. Generalized schematic of characteristic barite size and morphology as a function of experimental barite saturation index, experiment duration, and soy phospholipid concentrations. Filled symbols indicate experimental conditions that yielded barite crystals that resemble marine barite.

Marine barite crystals likely precipitate within microenvironments in which Ba^{2+} and/or SO_4^{2-} concentrations are high enough to achieve a barite saturation index of around 2.5. Barite crystals that formed in less saturated solutions were small and irregular in shape (Figs. 8A, 8B) compared to most marine barite crystals (Fig. 1). Conversely, solutions with saturation indices above 2.5 produced distinctive concave diamond and rosette morphologies typical of rapid, diffusion-limited crystal growth (Figs. 2D, 2E) (Dirksen and Ring 1991; Garcia-Ruiz 1999). Crystals that formed under barite supersaturation of 3 or 3.5 did display rounded corners, which suggests a transition to slower, spiral crystal growth once ongoing barite precipitation lowers the barite supersaturation of the solution (Kucher et al. 2006; Weber et al. 2021). However, these rounded corners were only observed in the presence of diamond and rosette morphologies that,

to the best of our knowledge, have never been observed for marine barite crystals (e.g., Dehairs et al. 1980; Light and Norris 2021). Thus, our findings suggest that whatever mechanism(s) facilitate marine barite precipitation do so by establishing a fairly narrow range of Ba^{2+} and SO_4^{2-} concentrations that allow for stable barite crystal growth. The rarity of irregular crystals in populations of marine barite crystals suggests either that precipitation is inhibited below a SI of ~2.5 or that these crystals form but then dissolve in the water column. Ongoing marine barite precipitation within microenvironments likely prevents sufficient Ba^{2+} and SO_4^{2-} accumulation to establish saturation indices above 2.5.

We did not observe elliptical or barrel-shaped barite crystals resembling marine barite in any experimental treatment without organic compounds. Previous studies have found that high concentrations of Sr^{2+} can enhance barite crystal growth in the [010] direction and favor the formation of celestite-like morphologies that may more closely resemble marine barite (Weber et al. 2018; Sánchez-Pastor et al. 2006). However, we observed rectangular and rhomboidal barite crystal morphologies even at a Sr^{2+}:Ba^{2+} ratio of 10:1 under our experimental conditions, which were designed to emulate plausible conditions within a marine organic matter aggregate (Supplementary Information 2.1). Therefore, elevated Sr^{2+} concentrations in organic matter aggregates are unlikely to be the main driver of elliptical marine barite morphologies. Similarly, literature suggests that curvilinear barite crystal morphologies may be promoted by Ba^{2+}:SO_4^{2-} ratios greater than ~5 (Bracco et al. 2016), but these high ratios have little relevance to marine systems given the high ambient concentration of SO_4^{2-} in seawater (28.2 mmol kg^{-1}; Emerson and Hedges 2008). We explored barite precipitation at barite supersaturation of 2.5 with Ba^{2+}:SO_4^{2-} ratios ranging from elevated Ba^{2+} and ambient seawater SO_4^{2-} (1:625) to ambient seawater Ba^{2+} and elevated SO_4^{2-} (1:6670) (Supplementary Information 2.2). These experiments

did show changes in crystal size and morphology that suggest that Ba^{2+}:SO_4^{2-} ratios affect barite crystal growth mechanisms, but none of these treatments yielded crystals that resemble marine barite in size and morphology (Supplementary Information 2.2).

Our findings suggest that marine barite crystals precipitate in the presence of phospholipids or other organic compounds. We found that various organic compounds affected barite crystal morphologies, but, of the compounds analyzed here, only EDTA and soy phospholipids produced barite crystals that resembled marine barite (Figs. 9, 10). It is likely that other organic compounds also produce elliptical barite morphologies, but an exhaustive assessment of these compounds is outside the scope of this study. EDTA does not naturally occur in the ocean (Oviedo and Rodríguez 2003). Thus, the distinctive morphologies of marine barite cannot be attributed to growth modification by EDTA.

Phospholipids have more relevance than EDTA to marine contexts. Soy phospholipids were selected to serve as a proxy for the diverse range of phospholipids produced by marine organisms. Phospholipids in marine EPS are hypothesized to facilitate marine barite precipitation via the bioaccumulation of Ba and formation of amorphous, phosphorus-rich barite precursors (Martinez-Ruiz et al. 2018, 2019). Sulfate groups are then thought to substitute for the phospholipid phosphate moieties in the amorphous precursor, which yields crystalline barite (Martinez-Ruiz et al. 2018, 2019). Amorphous Ba-P phases and short-lived barite precursors have also been observed in other laboratory investigations (e.g., Jones et al. 2012; Ruiz-Agudo et al. 2020; Ruiz-Agudo et al. 2021). Given this existing literature, it is notable that phospholipid experimental treatments produced barite crystals that resemble marine barite. With the relatively high barite supersaturation of these treatments, phospholipid Ba bioaccumulation was not

necessary to yield barite precipitation. However, barite precipitation in these treatments may have still occurred via sulfate substitution into amorphous phosphorus-rich barite precursors that were rapidly replaced by crystalline barite under our experimental conditions. An amorphous phosphorus-rich barite precursor may contribute to the relatively high phosphorous counts observed via EDX for the Soy-100 treatment (Supplementary Information 2.3). The morphological similarity between marine barite and barite precipitated in the presence of phospholipids in this investigation provides new evidence for this precipitation pathway occurring in marine organic matter aggregates.

Characteristic elliptical barite morphologies were only consistently observed in solutions with soy phospholipid concentrations above 10 mg L^{-1} (Fig. 10). This far exceeds reported phospholipid concentrations in seawater: e.g., 0.6 - 5.7 μg L^{-1} in the North Atlantic (Gašparović et al. 2018), 3.0 - 27.7 μg L^{-1} in the Mediterranean (Frka et al. 2011), and 36.4 - 93.5 μg L^{-1} in the Equatorial Atlantic (Triesch et al. 2021). Marine phospholipids are primarily observed within the cell membranes of bacteria and other organisms (Suzumura 2005). Thus, phospholipid concentrations high enough to facilitate the precipitation of elliptical barite crystals may result from bacterial cell lysis, which can release cellular material into the extracellular matrix of organic matter aggregates (Flemming and Wingender 2010). Phospholipids play a role in maintaining EPS structure (Wingender et al. 1999), so EPS microenvironments themselves may contain sufficient phospholipid concentrations to yield elliptical barite morphologies.

Phospholipid experiments produced elliptical morphologies like those most frequently observed in seawater, but these experiments did not produce the six-sided barite morphologies that are also observed in seawater and marine sediments (Fig. 7). Six-sided marine barite morphologies are likely produced by slightly different precipitation conditions than those

recreated here. Godinho and Stack (2015) found that abiotic barite precipitation in the presence of NaCl favors the formation of six-sided crystals by promoting face-specific growth, and $SrCl_2$ can inhibit barite growth at particular crystal faces. Thus, six-sided marine barite crystals may form in the presence of relatively lower concentrations of organic compounds and reflect cation concentrations in their formation environments. These conditions warrant further study.

Lastly, our results suggest that marine barite precipitation is fairly rapid. Barite crystals from experiment durations of 10 minutes or more were more than twice the size and displayed more globular morphologies than typical marine barite crystals (Figs. 12, 13). This suggests that nascent barite crystals spend no more than a few minutes in microenvironments with a barite saturation index near 2.5. These supersaturated microenvironments themselves may be short-lived due to a depletion of Ba^{2+} or SO_4^{2-} ions. Alternatively, barite crystals may become dislodged from the precipitation microenvironment once they reach a certain size. Previous laboratory investigations simulating marine barite precipitation have conducted incubations on timescales of days or weeks (e.g., Ganeshram et al. 2003; González-Muñoz et al. 2003; Torres-Crespo et al. 2015). These relatively long time periods may be necessary to facilitate the formation of microenvironments supersaturated with respect to barite, but, once these microenvironments are formed, barite precipitation is likely much more rapid. Relatively few methods exist for studying microscale spatial and temporal variability within marine organic matter aggregates, so our findings provide valuable insights into their microscale heterogeneity and dynamism.

Crystallographic origins of different barite crystal morphologies

The different barite crystal morphologies observed here suggest differences in crystal structure and/or growth mechanisms between treatments. The larger size, globular morphology,

and more polycrystalline SAED patterns observed for barite crystals with longer precipitation times suggest that they are the result of barite crystal aggregation. Alternatively, they may reflect the continued growth of existing barite particles once barite supersaturation has dropped below the threshold needed for the nucleation of new barite crystals (e.g., Weber et al. 2021).

Varied crystal morphology in the presence of organic additives may be partly due to heterogenous barite nucleation and growth, either on the glass walls of the beaker or, for phospholipid treatments, in association with microscopic phospholipid aggregates. Other investigations have observed Ba^{2+} accumulation and heterogeneous barite nucleation and growth at organic-water interfaces with terminal thiol (-SH) or carboxylic (-COOH) functional groups (Dai et al. 2016; Deng et al. 2022). As previously discussed, laboratory studies have also demonstrated that phospholipids concentrate Ba^{2+} (Martinez-Ruiz et al. 2018). This suggests that barite nucleation and growth may occur at organic-water interfaces with higher barite supersaturation than the surrounding solution in any of our experiments with organic additives. The texture of barite crystals synthesized in the presence of formic acid (Fig. 9A) somewhat resembled that of barite crystals formed in a solution with a barite saturation index of 3 (Fig. 8D), so localized Ba^{2+} accumulation and subsequent heterogeneous barite nucleation is particularly plausible for the formic acid treatment. Additional work is needed to assess heterogeneous barite nucleation and growth under conditions relevant to marine contexts.

The elliptical morphology observed for barite synthesized in the presence of EDTA is likely due to an increase in the relative exposure of particular crystal faces during crystallization. EDTA is an organic ligand that binds Ba^{2+}, but the influence of EDTA on barite morphology cannot be explained by complexation alone (Jones et al. 2007). Instead, Jones et al. (2007) suggests that EDTA influences barite morphology through carboxyl group interactions on

positively charged Ba^{2+} ions at the (0,1,0) or (0,1,1) crystal faces. Our findings are consistent with this mechanism for crystal growth modification; d-spacings in the SAED pattern for a barite crystal synthesized in the presence of EDTA suggest a basal face of (0,1,1) (Supplementary Information 2.4).

Our findings and existing literature suggest some potential explanations for why phospholipid-bearing solutions produced elliptical barite crystals. Organic solvents can influence barite nucleation, step advancement rates, and Ba^{2+} desolvation (e.g., Jones et al. 2008; Kowacz et al. 2007; Piana et al. 2006), so the ethanol used to dissolve the soy phospholipids may have affected barite crystal growth in the soy phospholipid treatments. However, the experimental treatment with only ethanol produced rhomboidal crystals (Fig. 10A), so the elliptical crystals that formed in the presence of soy phospholipids were likely due to crystal nucleation or growth effects independent from the presence of an organic solvent. Similarly, while some phosphorus was observed within the phospholipid treatment barite crystals, EDX maps and spectra suggest that phosphorus abundance did not clearly correlate with crystal morphology or phospholipid concentrations in the precipitating solution (Figs. 10I, 10O, 10U, Supplementary Information 2.3). This suggests that phospholipids do not primarily affect crystal morphology through direct incorporation into the barite crystal lattice but instead through one or more other mechanisms.

SAED patterns for crystals formed in the presence of soy phospholipids were insufficient to determine basal crystal faces with confidence (Figs. 10Q, 10W). However, given the similar crystal morphologies observed between soy phospholipid and EDTA treatments, it is plausible that carboxyl groups, phosphoryl groups, or other negatively charged phospholipid moieties influenced barite morphology via interactions at the (0,1,0) or (0,1,1) crystal faces, as is hypothesized to occur with EDTA. In fact, elliptical barite crystals and exposed (0,1,1) barite

crystal faces were also observed in crystals precipitated in the presence of phosphonates (Black et al. 1991) and algae (Barbosa et al. 2022). The barite crystals grown with our phospholipid treatments displayed more irregular edges and yielded more poorly defined SAED patterns than EDTA treatment crystals (Figures 3, 4). If phospholipid moiety interactions at barite crystal faces are responsible for the elliptical morphologies observed here, these irregularities suggest that phospholipid moieties are likely less consistent in their interactions with barite crystal faces than the carboxyl moieties of EDTA. This would be unsurprising, since phospholipids are larger and more structurally complex than EDTA.

Alternatively, phospholipids may create elliptical barite morphologies by causing the oriented aggregation of barite nanoparticles that form in association with phospholipid moieties. Elliptical barite morphologies in the presence of phytic acid are hypothesized to form via an interface coupled dissolution-precipitation mechanism in which an amorphous Ba-P phase is replaced with crystalline barite sub-units that aggregate with a preferential orientation (Ruiz-Agudo et al. 2021). Similar aggregation pathways have been proposed for barite precipitation in the presence of other polymers and solvents (Fillingham et al. 2021; Qi et al. 2001.; Ruiz-Agudo et al. 2020). Nonclassical crystallization by particle attachment and the transition from amorphous precursor to crystalline substance is common in the biomineralization of minerals such as calcite, magnetite, and zeolite (Jones and Ogden 2009; De Yoreo et al. 2015 and references therein). Therefore, nonclassical crystallization pathways such as oriented aggregation may contribute to the elliptical barite morphologies observed here and in marine barite.

Lastly, elliptical barite morphologies may have been promoted by the viscosity of microenvironments within the soy phospholipid treatments. Previous work has shown that viscous media and microbial EPS promotes the formation of rounded calcium carbonate crystal

morphologies by slowing the rate of ion diffusion and thus the rate of precipitation (Braissant et al. 2003; Buczynski and Chafetz 1991; Chekroun et al. 2004). Phospholipids increase the viscosity of a solution (Schneider 1997). Modeling and experimental work suggests that Ba^{2+} desolvation from water is the rate-limiting step in barite precipitation (Piana et al. 2006; Stack et al. 2016). Phospholipids may, in part, modify barite crystal morphology by influencing Ba^{2+} diffusion and/or desolvation and thus face-specific growth rates.

Implications for the marine barite proxy

Barite has been extensively used as a proxy for past ocean conditions (e.g., Carter et al. 2016; Erhardt et al. 2013; Kim et al. 2022; Lowery and Bralower 2022; Ma et al. 2014; Paytan et al. 1996), but its utility is limited by uncertainties surrounding barite formation, precipitation, dissolution, and variation in time and space (e.g., Carter et al. 2020). Our work advances the barite proxy by 1) developing methods that facilitate future laboratory investigations into marine barite dynamics and 2) providing evidence for marine barite as an ecosystem-wide proxy for export production.

Here, we developed simple and reliable methods for the synthesis of crystals resembling marine barite in size and shape. Laboratory investigations into marine barite dynamics have been lacking. Notably, we find that high barite saturation indices at solution mixing interfaces are an obstacle to simulating marine barite precipitation. As we discuss in our Methods section, this obstacle can be overcome and model marine barite crystals can be synthesized through the addition of dilute Na_2SO_4 to a relatively large volume of rapidly stirred artificial seawater containing Ba^{2+} and either EDTA or soy phospholipids. This method can be used to create barite crystals for future laboratory-based investigations into processes such as marine barite dissolution, ballasting of organic matter aggregates, and isotopic fractionation.

Our experiments also shed light onto marine barite precipitation mechanisms. Previous work suggested that elliptical marine barite crystals are the result of biotic precipitation within vesicles (Bertram and Cowen 1997), but our findings demonstrate that this characteristic marine barite morphology can precipitate without direct biological mediation. Rather, we find that crystals resembling marine barite in size and morphology passively precipitate in synthetic seawater with high concentrations of naturally occurring phospholipids. As previously discussed, this is consistent with the hypothesis that phospholipids within marine EPS facilitate barium accumulation and marine barite precipitation (Martinez-Ruiz et al. 2018, 2019). The fundamentally abiotic, passive precipitation of marine barite in association with chemical gradients created by biological activity and organic matter remineralization strengthens marine barite's utility as a proxy. It suggests that marine barite accumulation rates are not dependent on particular organism types but instead on EPS, which are produced by most marine microbes (Decho and Gutierrez 2017). Thus, barite is likely to serve as an ecosystem-wide productivity proxy.

Conclusions

Here, we used barite crystal morphology to constrain the plausible biogeochemical conditions under which marine barite precipitates. Our findings are consistent with the role of phospholipids in marine barite precipitation and provide new insight into microenvironments within marine organic matter aggregates. We suggest that marine barite is likely to crystallize quickly (within a few minutes or less) and at saturation indices near 2.5. The brief experiment durations needed to form crystals resembling marine barite suggest that the precipitation conditions for marine barite are ephemeral, perhaps reflecting the rapid drawdown of saturation state as crystallization occurs. Moreover, we have facilitated future laboratory investigations into

marine barite dynamics by developing simple and reliable methods for the synthesis of crystals that resemble marine barite in size and shape. These efforts advance marine barite as a tool for studying the marine carbon cycle in the past and present. This work also contributes to our understanding of mineral nucleation and growth within the ocean, biofilms, and other natural systems.

Acknowledgements

T.L. was supported by a U.S. Department of Defense National Defense Science and Engineering Graduate Student Fellowship, a William B. and Dorothy Heroy Research Grant from the Geological Society of America, and a Ruth Newmark Scholarship from the UCSD Friends of the International Center. The authors thank Drs. Athina Lange, Julia Diaz, Adina Paytan, and Tristan Horner for their valuable insights.

Chapter 2, in full, is a reprint of the material as it appears in "Marine barite morphology as an indicator of biogeochemical conditions within organic matter aggregates," published in Geochimica et Cosmochimica Acta in 2023. T. Light, F. Martínez-Ruiz, and R. Norris. The dissertation author was the primary investigator and author of this paper.

References

Akyol, E., Cedimagar, M. A., 2016. Size and morphology controlled synthesis of barium sulfate. Cryst. Res. Tech., 51, 393-399.

Arganda-Carreras, I., Kaynig, V., Rueden, C., Eliceiri, K. W., Schindelin, J., Cardona, A., Seung, S. H., 2017. Trainable Weka Segmentation: A Machine Learning Tool for Microscopy Pixel Classification. Bioinformatics. 33, 2424–26.

Barbosa, N., Jaquet, J., Urquidi, O., Adachi, T. B. M., Filella, M., 2022. Combined in Vitro and in Vivo Investigation of Barite Microcrystals in *Spirogyra* (Zygnematophyceae, Charophyta). J. Plant Physiol. 276, 153769.

Benton, W. J., Collins, I. R., Grimsey, I. M., Parkinson, G. M., Rodger, S. A., 1993. Nucleation, Growth and Inhibition of Barium Sulfate-Controlled Modification with Organic and Inorganic Additives. Faraday Discuss. 95, 281.

Bernard-Michel, B., Pons, M. N., Vivier, H., 2002. Quantification, by Image Analysis, of Effect of Operational Conditions on Size and Shape of Precipitated Barium Sulphate. Chem. Eng. J. 87, 135–47.

Bertram, M. A., Cowen, J. P., 1997. Morphological and Compositional Evidence for Biotic Precipitation of Marine Barite. J. Mar. Res. 55, 577–93.

Bethke, C. M., 2022. Geochemical and Biogeochemical Reaction Modeling. Cambridge University Press, Cambridge.

Bishop, J. K. B., 1988. The Barite-Opal-Organic Carbon Association in Oceanic Particulate Matter. Nature 332, 341.

Black, S. N, Bromley, L. A., Cottier, D., Davey, R. J., Dobbs, B., 1991. Interactions at the Organic/Inorganic Interface: Binding Motifs for Phosphonates at the Surface of Barite Crystals. J. Chem. Soc. Faraday. Trans. 87, 6.

Boon, M., Jones, F., 2016. Barium sulfate crystallization from synthetic seawater. Crys. Growth Des. 16, 4646-4657.

Bracco, J. N., Gooijer, Y., Higgins, S. R., 2016. Hydrothermal atomic force microscopy observations of barite step growth rates as a function of the aqueous barium-to-sulfate ratio. Geochim. Cosmochim. Acta. 183, 1-13.

Braissant, O., Cailleau, G., Dupraz, C., Verrecchia, E. P., 2003. Bacterially Induced Mineralization of Calcium Carbonate in Terrestrial Environments: The Role of Exopolysaccharides and Amino Acids. J. Sed. Res. 73, 485–90.

Buczynski, C., Chafetz, H. S., 1991. Habit of bacterially induced precipitates of calcium carbonate and the influence of medium viscosity on mineralogy. J. Sed. Res. 61, 226-233

Buesseler, K. O., Boyd, P. W., Black, E. E., Siegel, D. A., 2020. Metrics That Matter for Assessing the Ocean Biological Carbon Pump. Proc. Natl. Acad. Sci. 117, 9679–87.

Carter, S. C., Griffith, E. M., Penman, D. E., 2016. Peak intervals of equatorial Pacific export production during the middle Miocene climate transition. Geology, 44, 923-926.

Carter, S. C., Paytan, A., Griffith, E. M., 2020. Toward an Improved Understanding of the Marine Barium Cycle and the Application of Marine Barite as a Paleoproductivity Proxy. Minerals. 10, 421.

Chekroun, K. B., Rodríguez-Navarro, C., González-Muñoz, M. T., Arias, J. M., Cultrone, G., Rodríguez-Gallego, M., 2004. Precipitation and growth morphology of calcium carbonate induced by Myxococcus xanthus: implications for recognition of bacterial carbonates. J. Sed. Res. 74, 868-876.

Dai, C., Stack, A. G., Koishi, A., Fernandez-Martinez, A., Lee, S. S., Hu, Y., 2016. Heterogeneous nucleation and growth of barium sulfate at organic–water interfaces: interplay

between surface hydrophobicity and Ba^{2+} adsorption. Langmuir, 32, 5277-5284.

Decho, A. W., Gutierrez, T., 2017. Microbial extracellular polymeric substances (EPSs) in ocean systems. Front. Microbiol. 8, 922.

Dehairs, F., Chesselet, R., Jedwab, J., 1980. Discrete Suspended Particles of Barite and the Barium Cycle in the Open Ocean. Earth Planet. Sci. Lett. 49, 528–50.

Deng, N., Stack, A. G., Weber, J., Cao, B., De Yoreo, J. J., Hu, Y., 2019. Organic–mineral interfacial chemistry drives heterogeneous nucleation of Sr-rich (Ba_x, Sr_{1-x}) SO_4 from undersaturated solution. Proc. Nat. Acad. Sci. 116, 13221-13226.

Deng, N., Zuo, X., Stack, A. G., Lee, S. S., Zhou, Z., Weber, J., Hu, Y., 2022. Selenite and Selenate Sequestration during Coprecipitation with Barite: Insights from Mineralization Processes of Adsorption, Nucleation, and Growth. Environ. Sci. Tech. 56, 15518-15527.

De Yoreo, J. J., Gilbert, P. U., Sommerdijk, N. A., Penn, R. L., Whitelam, S., Joester, D., Zhang, H., Rimer, J. D., Navrotsky, A., Banfield, J. F., Wallace, A. F., Marc Michelle, F., Meldrum, F. C., Cölfen, H., Dove, P. M., 2015. Crystallization by particle attachment in synthetic, biogenic, and geologic environments. Science, 349, aaa6760.

Dirksen, J. A., Ring, T. A., 1991. Fundamentals of crystallization: kinetic effects on particle size distributions and morphology. Chem. Eng. Sci., 46, 2389-2427.

Dupraz, C., Reid, R. P., Braissant, O., Decho, A. W., Norman, R. S., Visscher, P. T., 2009. Processes of carbonate precipitation in modern microbial mats. Earth Sci. Rev., 96, 141-162.

Emerson, S., Hedges, J., 2008. Chemical Oceanography and the Marine Carbon Cycle. Cambridge University Press, Cambridge.

Erhardt, A. M., Pälike, H., Paytan, A., 2013. High-resolution record of export production in the eastern equatorial Pacific across the Eocene-Oligocene transition and relationships to global climatic records. Paleoceanography. 28, 130-142.

Fakhraee, M., Planavsky, N. J., Reinhard, C. T., 2020. The Role of Environmental Factors in the Long-Term Evolution of the Marine Biological Pump. Nat. Geosci. 13, 812–16.

Fernandez-Diaz, L., Putnis, A., Cumberbatch, T. J., 1990. Barite nucleation kinetics and the effect of additives. Eur. J. Mineral. 2, 495-502.

Fillingham, R., Boon, M., Javaid, S., Saunders, J. A., Jones, F., 2021. Barium sulfate crystallization in non-aqueous solvent. Cryst. Eng. Comm. 23, 2249-2261.

Flemming, H., Wingender, J., 2010. The Biofilm Matrix. Nat. Rev. Microbiol. 8, 623–33.

Freeman, S. R., Jones, F., Ogden, M. I., Oliviera, A., Richmond, W. R., 2006. Effect of Benzoic Acids on Barite and Calcite Precipitation. Cryst. Growth Des. 6, 2579–87.

Frka, S., Gašparović, B., Marić, D., Godrijan, J., Djakovac, T., Vojvodić, V., Dautović, J., Kozarac, Z., 2011. Phytoplankton Driven Distribution of Dissolved and Particulate Lipids in a Semi-Enclosed Temperate Sea (Mediterranean): Spring to Summer Situation. Estuar. Coast. Shelf Sci. 93, 290–304.

Ganeshram, R. S., François, R., Commeau, J., Brown-Leger, S. L., 2003. An Experimental Investigation of Barite Formation in Seawater. Geochim. Cosmochim. Acta. 67, 2599–2605.

Garcia-Ruiz, J., 1999. Morphological Behavior of Inorganic Precipitation Systems. Inst. Met. Mis. Astrobiol. II. 3755, 74–82.

Gašparović, B., Penezić, A., Lampitt, R. S., Sudasinghe, N., Schaub, T., 2018. Phospholipids as a Component of the Oceanic Phosphorus Cycle. Mar. Chem. 205, 70–80.

Godinho, J. R., Stack, A. G., 2015. Growth kinetics and morphology of barite crystals derived from face-specific growth rates. Cryst. Growth Des., 15, 2064-2071.

Goldschmidt, V. M., 1913. Atlas der Krystallformen. Carl Winters Universitätsbuchhandlung, Heidelberg.

González-Muñoz, M. T., Fernández-Luque, B., Martínez-Ruiz, F., Chekroun, K. B., Arias, J. M., Rodríguez-Gallego, M., Martínez-Cañamero, M., de Linares, C., Paytan, A., 2003. Precipitation of Barite by *Myxococcus Xanthus*: Possible Implications for the Biogeochemical Cycle of Barium. Appl. Environ. Microbiol. 69, 5722–25.

Griffith, E. M., Thomas, E., Lewis, A. R., Penman, D. E., Westerhold, T., Winguth, A. M. E., 2021. Bentho-Pelagic Decoupling: The Marine Biological Carbon Pump During Eocene Hyperthermals. Paleoceanogr. Paleoclimatol. 36, e2020PA004053.

He, S., Oddo, J. E., Tomson, M. B., 1995. The nucleation kinetics of barium sulfate in NaCl solutions up to 6 m and 90 C. J. Colloid Interf. Sci., 174, 319-326.

Henson, S. A., Laufkötter, C., Leung, S., Giering, S. L. C., Palevsky, H. I., Cavan, E. L., 2022. Uncertain Response of Ocean Biological Carbon Export in a Changing World. Nat. Geosci. 15, 248–54.

Hsieh, Y., Henderson, G. M., 2017. Barium Stable Isotopes in the Global Ocean: Tracer of Ba Inputs and Utilization. Earth Planet. Sci. Lett. 473, 269–78.

Hülse, D., Arndt, S., Wilson, J. D., Munhoven, G., Ridgwell, A., 2017. Understanding the Causes and Consequences of Past Marine Carbon Cycling Variability through Models. Earth-Sci. Rev. 171, 349–82.

House, B. M., Norris, R. D., 2020. Unlocking the barite paleoproductivity proxy: A new high-throughput method for quantifying barite in marine sediments. Chem. Geo., 552, 119664.

Iversen, M. H., 2023. Carbon Export in the Ocean: A Biologist's Perspective. Ann. Rev. Mar. Sci. 15, 357-381.

Jacquet, S. H. M., Dehairs, F., Dumont, I., Becquevort, S., Cavagna, A. J., Cardinal, D., 2011. Twilight Zone Organic Carbon Remineralization in the Polar Front Zone and Subantarctic Zone South of Tasmania. Deep Sea Res. II: Top. Stud. Oceanogr. 58, 2222–34.

Jones, F., Jones, P., Ogden, M. I., Richmond, W. R., Rohl, A. L., Saunders, M., 2007. The Interaction of EDTA with Barium Sulfate. J. Colloid Interface Sci. 316, 553–61.

Jones, F., Ogden, M. I., 2009. Controlling crystal growth with modifiers. CrystEngComm. 12, 1016-1023.

Jones, F., Piana, S., Gale, J. D., 2008. Understanding the kinetics of barium sulfate precipitation from water and water–methanol solutions. Cryst. Growth Des. 8, 817-822.

Jones, F., 2012. Infrared investigation of barite and gypsum crystallization: Evidence for an amorphous to crystalline transition. CrystEngComm. 14, 8374-8381.

Judat, B., M. Kind., 2004. Morphology and Internal Structure of Barium Sulfate—Derivation of a New Growth Mechanism. J. Colloid Interface Sci. 269, 341–53.

Kim, J. E., Westerhold, T., Alegret, L., Drury, A. J., Röhl, U., Griffith, E. M., 2022. Precessional pacing of tropical ocean carbon export during the Late Cretaceous. Clim. Past, 18, 2631-2641.

Kowacz, M., Putnis, C. V., Putnis, A., 2007. The effect of cation: anion ratio in solution on the mechanism of barite growth at constant supersaturation: Role of the desolvation process on the growth kinetics. Geochim. Cosmochim. Acta. 71, 5168-5179.

Koyama, T., Thompson, T. G., 1964. Identification and determination of organic acids in sea water by partition chromatography. J. Oceanogr. Soc. Japan, 20, 209-220.

Klinger, M., 2017. More Features, More Tools, More CrysTBox. J. Appl. Crystallogr. 50, 1226–34.

Kucher, M., Babic, D., Kind, M., 2006. Precipitation of barium sulfate: experimental investigation about the influence of supersaturation and free lattice ion ratio on particle formation. Chem. Eng. Process, 45, 900-907.

Light, T., Norris, R., 2021. Quantitative Visual Analysis of Marine Barite Microcrystals: Insights into Precipitation and Dissolution Dynamics. Limnol. Oceanogr. 66, 3619–29.

Liu, S., Parsons, R., Opalk, K., Baetge, N., Giovannoni, S., Bolaños, L. M., Kujawinski, E. B., Longnecker, K., Lu, Y., Halewood, E., Carlson, C. A., 2020. Different carboxyl-rich alicyclic molecules proxy compounds select distinct bacterioplankton for oxidation of dissolved organic matter in the mesopelagic Sargasso Sea. Limnol. Oceanogr. *65*, 1532-1553.

Liu, Y., Guo, X., Yang, S., He, Q., Jin, H., 2018. Controllable Preparation of Uniform Micron-Sized Barium-Sulfate Spheres. Cryst. Res. Tech. 53, 1700212.

Lowery, C. M., Bralower, T. J., 2022. Elevated Post K-Pg Export Productivity in the Gulf of

Mexico and Caribbean. Paleoceanogr. Paleoclim. 37, e2021PA004400.

Ma, Z., Gray, E., Thomas, E., Murphy, B., Zachos, J., Paytan, A., 2014. Carbon Sequestration during the Palaeocene–Eocene Thermal Maximum by an Efficient Biological Pump. Nat. Geosci. 7, 382–88.

Markovic, S., Paytan, A., Li, H., Wortmann, U. G., 2016. A Revised Seawater Sulfate Oxygen Isotope Record for the Last 4Myr. Geochim. Cosmochim. Acta. 175, 239–51.

Martinez-Ruiz, F., Paytan, A., Gonzalez-Muñoz, M. T., Jroundi, F., Abad, M. M., Lam, P. J., Bishop, J. K. B., Horner, T. J., Morton, P. L., Kastner, M., 2019. Barite Formation in the Ocean: Origin of Amorphous and Crystalline Precipitates. Chem. Geol. 511, 441–51.

Martinez-Ruiz, F., Jroundi, F., Paytan, A., Guerra-Tschuschke, I., Abad, M., González-Muñoz, M. T., 2018. Barium Bioaccumulation by Bacterial Biofilms and Implications for Ba Cycling and Use of Ba Proxies. Nat. Comm. 9, 1619.

Martinez-Ruiz, F., Paytan, A., Gonzalez-Muñoz, M. T., Jroundi, F., Abad, M. M., Lam, P. J., Horner, T. J., Kastner, M., 2020. Barite Precipitation on Suspended Organic Matter in the Mesopelagic Zone. Front. Earth Sci. 8, 567714.

Monnin, C., Jeandel, C., Cattaldo, T., Dehairs, F., 1999. The Marine Barite Saturation State of the World's Oceans. Mar. Chem. 65, 253–261.

Murray, R. W., Leinen, M., 1993. Chemical transport to the seafloor of the equatorial Pacific Ocean across a latitudinal transect at 135 W: tracking sedimentary major, trace, and rare earth element fluxes at the Equator and the Intertropical Convergence Zone. Geochim. Comochim. Acta. 57, 4141-4163.

Nowicki, M., DeVries, T., Siegel, D. A., 2022. Quantifying the Carbon Export and Sequestration Pathways of the Ocean's Biological Carbon Pump. Glob. Biogeochem. Cycles. 36, e2021GB007083.

Oviedo, C., Rodríguez, J., 2003. EDTA: The Chelating Agent under Environmental Scrutiny. Química Nova. 26, 901–905.

Piana, S., Jones, F., Gale, J. D., 2006. Assisted desolvation as a key kinetic step for crystal growth. J. Am. Chem. Soc., 128, 13568-13574.

Paytan, A., Kastner, M., Campbell, D., Thiemens, M. H., 1998. Sulfur Isotopic Composition of Cenozoic Seawater Sulfate. Science. 282, 1459–62.

Paytan, A., Kastner, M., Chavez, F. P., 1996. Glacial to interglacial fluctuations in productivity in the equatorial Pacific as indicated by marine barite. Science, 274, 1355-1357.

Paytan, A., Kastner, M., Martin, E. E., Macdougall, J. D., Herbert, T., 1993. Marine Barite as a Monitor of Seawater Strontium Isotope Composition. Nature. 366, 445– 449.

Qi, L., Cölfen, H., Antonietti, M., Li, M., Hopwood, J. D., Ashley, A. J., Mann, S., 2001. Formation of $BaSO_4$ fibres with morphological complexity in aqueous polymer solutions. Chem. Eur. J. 7, 3526-3532.

R Core Team, 2020. R: A Language and Environment for Statistical Computing. R Foundation for Statistical Computing, Vienna, Austria.

Ruiz Agudo, C., Ibañez-Velasco, A., Ruiz-Agudo, E., 2021. The role of amorphous P-bearing precursors on barite formation. Geochem. Perspect. Lett. 18, 32-36.

Ruiz-Agudo, C., McDonogh, D., Avaro, J. T., Schupp, D. J., Gebauer, D., 2020. Capturing an amorphous $BaSO_4$ intermediate precursor to barite. CrystEngComm. 22, 1310-1313.

Ruiz-Agudo, C., Ruiz-Agudo, E., Burgos-Cara, A., Putnis, C. V., Ibáñez-Velasco, A., Rodriguez-Navarro, C., Putnis, A., 2016. Exploring the effect of poly(acrylic acid) on pre-and post-nucleation $BaSO_4$ species: New insights into the mechanisms of crystallization control by polyelectrolytes. CrystEngComm. 18, 2830-2842.

Ruiz-Agudo, C., Ruiz-Agudo, E., Putnis, C. V., Putnis, A., 2015. Mechanistic principles of barite formation: from nanoparticles to micron-sized crystals. Cryst. Growth Des. 15, 3724-3733.

Sánchez-Pastor, N., Pina, C. M., Fernandez-Diaz, L., 2006. Relationships between crystal morphology and composition in the (Ba, Sr) SO_4–H_2O solid solution–aqueous solution system. Chem. Geo. 225, 266-277.

Saraya, M. E. S. I. 2015. Effect of L (+) ascorbic acid and monosodium glutamate concentration on the morphology of calcium carbonate. J. Solid State Chem. 231, 114-122.

Schindelin, J., Arganda-Carreras, I., Frise, E., Kaynig, V., Longair, M., Pietzsch, T., Preibisch, S., et al., 2012. Fiji: An Open-Source Platform for Biological-Image Analysis. Nat. Methods. 9, 676–682.

Schindelin, J., Rueden, C. T., Hiner, M. C., Eliceiri, K. W., 2015. The ImageJ Ecosystem: An Open Platform for Biomedical Image Analysis. Mol. Reprod. Dev. 82, 518–29.

Schneider, M., 1997. Phospholipids. In: Gunstone, F. D., Padley, F. B. (Eds.), Lipid technologies and applications. Routledge, Milton Park, pp. 51-78.

Shen, Y., Li, C., Zhu, X., Xie, A., Qiu, L., Zhu, J., 2007. Study on the Preparation and Formation Mechanism of Barium Sulphate Nanoparticles Modified by Different Organic Acids. J. Chem. Sci. 119, 319–324.

Smith, E., Hamilton-Taylor, J., Davison, W., Fullwood, N. J., McGrath, M., 2004. The effect of humic substances on barite precipitation–dissolution behaviour in natural and synthetic lake waters. Chem. Geo. 207, 81-89.

Stack, A. G., Borreguero, J. M., Prisk, T. R., Mamontov, E., Wang, H. W., Vlcek, L., Wesolowski, D. J., 2016. Precise determination of water exchanges on a mineral surface. Phys.

Chem. Chem. Phys. 18, 28819-28828.

Sun, X., Yang, Z., Fan, D., Li, Y., 2015. Crystals of Suspended Marine Barite in the Eastern Equatorial Pacific: Processes of Dissolution and Effects on Crystal Morphology. Chin. J. Oceanol. Limnol. 33, 194–203.

Suzumura, M., 2005. Phospholipids in Marine Environments: A Review. Talanta. 66, 422–434.

Torres-Crespo, N., Martínez-Ruiz, F., González-Muñoz, M. T., Bedmar, E. J., De Lange, G. J., Jroundi, G. J., 2015. Role of Bacteria in Marine Barite Precipitation: A Case Study Using Mediterranean Seawater. Sci. Tot. Environ. 512–513, 562–571.

Triesch, N., van Pinxteren, M., Frka, S., Stolle, C., Spranger, T., Hoffmann, E. H., Gong, X., et al., 2021. Concerted Measurements of Lipids in Seawater and on Submicrometer Aerosol Particles at the Cabo Verde Islands: Biogenic Sources, Selective Transfer and High Enrichments. Atmospheric Chem. Phys. 21, 4267–83.

Weber, J., Bracco, J.N., Poplawsky, J.D., Ievlev, A.V., More, K.L., Lorenz, M., Bertagni, A.L., Jindra, S.A., Starchenko, V., Higgins, S.R., Stack, A.G., 2018. Unraveling the effects of strontium incorporation on barite growth—In situ and ex situ observations using multiscale chemical imaging. Cryst. Growth Des. 18, 5521-5533.

Weber, J., Bracco, J. N., Yuan, K., Starchenko, V., Stack, A. G., 2021. Studies of Mineral Nucleation and Growth Across Multiple Scales: Review of the Current State of Research Using the Example of Barite ($BaSO_4$). ACS Earth Space Chem., 5, 3338-3361.

Wickham, H., 2016. Ggplot2: Elegant Graphics for Data Analysis. New York: Springer-Verlag.

Widanagamage, I. H., Schauble, E. A., Scher, H. D., Griffith, E. M., 2014. Stable strontium isotope fractionation in synthetic barite. Geochim. Chosmochim. Acta. 147, 58-75.

Widanagamage, I. H., Waldron, A. R., Glamoclija, M., 2018. Controls on Barite Crystal Morphology during Abiotic Precipitation. Minerals. 8, 480.

Wingender, J., Neu, T. R., Flemming, H., 1999. What Are Bacterial Extracellular Polymeric Substances? in: Wingender, J., Neu, T. R., Flemming, H. (Eds.), Microbial Extracellular Polymeric Substances: Characterization, Structure and Function. Springer, Berlin, 1–19.

Wangersky, P. J., 1952. Isolation of ascorbic acid and rhamnosides from sea water. Science, 115, 685-685.

Yao, W., Griffith, E., Paytan, A., 2021. Pelagic Barite: Tracer of Ocean Productivity and a Recorder of Isotopic Compositions of Seawater S, O, Sr, Ca and Ba, 1st ed. Cambridge University Press, Cambridge.

Yao, W., Paytan, A., Griffith, E. M., Martínez-Ruiz, F., Markovic, S., Wortmann, U. G., 2020. A Revised Seawater Sulfate S-Isotope Curve for the Eocene. Chem. Geol. 532, 119382.

Yuan, K., Starchenko, V., Rampal, N., Yang, F., Yang, X., Xiao, X., Lee, W.K., Stack, A.G., 2021. Opposing effects of impurity ion Sr^{2+} on the heterogeneous nucleation and growth of barite ($BaSO_4$). Cryst. Growth Des., 21, 5828-5839.

Zhang, M., Zhang, B., Li, X., Yin, Z., Guo, X., 2011. Synthesis and Surface Properties of Submicron Barium Sulfate Particles. Appl. Surf. Sci. 258, 24–29.

CHAPTER 3: Water column barium sulfate dissolution and shielding by organic matter aggregates: Implications for the pelagic barite proxy

T. Light, M. Garcia, J. C. Prairie, F. Martínez Ruiz, and R. Norris

Abstract

Pelagic barite ($BaSO_4$) and related proxies are useful tools for reconstructing the marine carbon cycle. The factors controlling pelagic barite dissolution in the ocean water column are poorly understood, which adds uncertainty to Ba-based reconstructions. Here, we conducted static laboratory incubations to test the sensitivity of barium sulfate dissolution rate to a range of commonly occurring seawater pH, salinity, and temperature conditions. We observed relatively rapid dissolution rates ranging from 1.7 ± 0.4 to 3.4 ± 0.8 pg $BaSO_4$ day^{-1} for these experiments, and we did not observe statistically significant differences in the rate of dissolution with varying pH, salinity, or temperature. The slowest dissolution rate observed in these experiments suggests that an average barium sulfate crystal would survive in the ocean water column just 6.2 ± 0.3 days. We estimate that an average isolated pelagic barite crystal would take 67 years to sink down through the water column, so our experiments imply that solitary pelagic barite crystals do not survive this transit. We conducted an additional experiment on a roller table to assess the impact of organic matter aggregates on barium sulfate dissolution. Free barium sulfate crystals incubated on the roller table dissolved even more rapidly than crystals in the static experiment (19 ± 7 pg $BaSO_4$ day^{-1}), but barium sulfate crystals incubated with organic matter aggregates showed little sign of dissolution over time. Our findings suggest that organic matter aggregates play a vital role in shielding pelagic barite from dissolution in the water column. This implies that pelagic barite in ocean sediments records the arrival of organic detritus to the seafloor, not just barite crystal formation in sinking organic matter in the upper water column.

Additional work is needed to determine which aspects of the marine carbon cycle the pelagic barite proxy captures.

Introduction

The biological pump, or the export of atmospheric carbon dioxide to the deep ocean and marine sediments in the form of organic carbon, plays an important role in regulating global climate on timescales of tens to thousands of years (DeVries, 2022). Quantifying how the biological pump responds to variable climate, biogeochemical, and ecosystem conditions is vital to accurately predicting how the marine carbon cycle will function in the future (e.g., Fakhraee et al., 2020; Nowicki et al., 2022). Reliable proxies for various components of the marine carbon cycle are required to achieve a nuanced understanding of the past and present biological pump (e.g., Lam et al., 2011; Ma et al., 2015; Winckler et al., 2016). However, proxy interpretation can be complicated by the decoupling of primary productivity in the surface ocean, export production of organic carbon out of the surface ocean, and organic carbon burial at the seafloor (Lopes et al., 2015).

Pelagic barite is a promising tool for reconstructing various aspects of the marine biological pump (Carter et al., 2020; Horner et al., 2021). Barite is a naturally occurring mineral consisting of barium sulfate ($BaSO_4$), while pelagic or marine barite specifically refers to barite that forms in the ocean water column (e.g., Paytan and Griffith, 2007; Yao et al., 2020). Pelagic barite is ubiquitous in seawater and ocean sediments (Dehairs et al., 1980; Paytan and Griffith, 2007) and occurs as microcrystals that are, on average, approximately 1 μm in length and have a mass of 9–11 pg (Bu et al., 2023; Dehairs et al., 1980; Light and Norris, 2021; Robin et al., 2003). It is thought to precipitate in microenvironments within organic matter aggregates during microbial oxidation, as first proposed by Chow and Goldberg (1960). Given the link between

organic matter remineralization and barite precipitation, pelagic barite accumulation rates in ocean sediments have been widely used to reconstruct marine export production (e.g., Costa et al., 2016; Nürnberg et al., 1997; Paytan et al., 1996; Torfstein et al., 2010). However, uncertainties surrounding pelagic barite precipitation and preservation limit it from achieving its full potential as a proxy.

Previous investigations have studied barium sulfate dissolution kinetics and dynamics, particularly in the context of inorganic chemistry and formation of scale in pipelines and well equipment in the oil and gas industries (Higgins et al., 1998; Kamal et al., 2018; Nancollas and Liu, 1975). Observations of barium sulfate dissolution in a closed system reactor demonstrate that barite dissolves with a reaction order of 0.2 with respect to the barium sulfate saturation state (Ω_{BaSO_4}) of the surrounding fluid (Zhen-Wu et al., 2016), as defined by the equation:

$$\Omega_{BaSO_4} = \frac{a_{Ba^{2+}} a_{SO_4{}^{2-}}}{K_{BaSO_4}}$$

where *a* is the activity of the specified species and KBaSO4 is the equilibrium constant for the dissolution of solid $BaSO_4$ into aqueous Ba^{2+} and SO_4^{2-} ions. The rate-limiting step of barite dissolution is the detachment of a Ba^{2+} ion from the barite surface, which is followed by the relatively fast dissolution of a neighboring SO_4^{2-} ion (Becker et al., 2005). Factors such as temperature, concentrations of background electrolytes, and presence low molecular weight organic compounds and organic chelators can affect the rate of barium sulfate dissolution (e.g., Christy and Putnis, 1993; Dove and Czank, 1995; Dunn et al., 1999; Ouyang et al., 2017; Ouyang et al., 2019; Zhen-Wu et al., 2016). In seawater, pelagic barite solubility has been constrained via laboratory experiments (Burton et al., 1968) and by computation (Church and Wolgemuth, 1972; Hanor, 1969; Rushdi et al., 2000).

Pelagic barite dissolution plays a significant role in the marine barium cycle (e.g., Carter et al., 2020), but the factors controlling it are poorly constrained. Ba and δ^{138}Ba water column profiles in a variety of oceanographic settings are consistent with pelagic barite precipitation in the mesopelagic zone followed by pelagic barite dissolution below 1000 m depth (e.g., Bates et al., 2017; Horner et al., 2015; Horner and Crockford, 2021; Hsieh and Henderson, 2017). The ocean is largely undersaturated with respect to barite, although barite saturation varies geographically and with water depth (Church and Wolgemuth, 1972; Monnin et al., 1999; Rushdi et al., 2000). Seawater is undersaturated with respect to barite in the surface ocean globally and at depth in the Atlantic Ocean, while seawater is at or above saturation below 1000 m in much of the Pacific Ocean (Mete et al., 2023). Meanwhile, observations suggest that pelagic barite burial efficiencies are not predicted by barite saturation indices in the overlying water column (Rahman et al., 2022). Sr/Ba and δ^{138}Ba have been proposed as methods for accounting for variable pelagic barite preservation in the interpretation of sediment barite records (Van Beek et al., 2003; Bridgestock et al., 2018; Bridgestock et al., 2019).

Estimates of water column barite dissolution vary. ^{230}Th-normalized barium flux measurements suggest average water column barite dissolution rates of 58–69% and 17–46% along transects in the North Atlantic and Eastern Tropical Pacific, respectively (Rahman et al., 2022). Observations in the North Pacific suggest water column dissolution rates of 60 ± 20%, while approximately 10% of water column pelagic barite crystals show dissolution pits and other morphological evidence of dissolution (Light and Norris, 2021). Box models created using sediment trap (Dymond et al., 1992) and pore water (Paytan and Kastner, 1996) data suggest that ~70% of particulate barite flux to the deep ocean dissolves before incorporation into the sediment record. Pelagic barite dissolution rates are high in anoxic ocean basins such as the

Black Sea where there is water column sulfate reduction (Falkner et al., 1993), but little is known regarding the controls on barite dissolution rates in oxic waters. Questions remain regarding how variable barite dissolution rates influence sediment barite records (e.g., Schoepfer et al., 2015). Organic matter aggregates may shield marine barite crystals from dissolution (Carter et al., 2020), but, to our knowledge, the impact of aggregates on barite dissolution has never been directly assessed.

Here, we conducted laboratory experiments to estimate plausible rates of water column pelagic barite dissolution under different chemical and environmental conditions. We compared the dissolution rate of synthetic barium sulfate microcrystals in two sets of experiments. In the organic matter shielding experiment, we assessed differences in the rate of barium sulfate dissolution between crystals encased within organic matter aggregates formed from a diatom culture (the "Aggregate" treatment), free crystals from the water column overlying the aggregates in the aggregate tanks (the "Overlying Water" treatment), and free crystals within a control tank without diatoms added (the "No Aggregate" treatment). In the second set of experiments, we assessed barium sulfate dissolution in free crystals suspended in seawater under a range of salinity, pH, and temperature conditions. We also used Stokes' Law to calculate approximate pelagic barite sinking velocities in the water column to contextualize observed dissolution rates, and we consider the implications for interpretation of marine barite proxies.

Materials and Methods

Barium sulfate crystal synthesis

A protocol was developed to synthesize barium sulfate microcrystals as homogenous in size and morphology as possible. Initially, we tested simpler methods for the formation of barium sulfate. These included addition of $BaCl_2$ to seawater, addition of $BaCl_2$ to artificial

seawater in a single step, and addition of $BaCl_2$ to seawater seeded with smaller barium sulfate microcrystals. These methods yielded crystals with a large range of crystal morphologies and sizes within a single batch and were discontinued.

Subsequently, we standardized our methods as follows: for each batch, seawater was collected from the Scripps Institution of Oceanography pier and filtered through a 0.2 um pore size polycarbonate membrane filter (referred to as filtered seawater hereafter). Barium sulfate precipitation was induced by adding 1 mL 10 mM $BaCl_2$ to 49 mL filtered seawater in polypropylene centrifuge tubes. Tubes were shaken and placed in a 4°C refrigerator for 60 min to allow for crystal growth.

Barium sulfate-spiked seawater was then transferred to 1 L polycarbonate bottles, and the bottles were shaken to coat their walls with the seeded barium sulfate solution. These bottles were emptied to remove the initial barium sulfate crystals, which were large and displayed many different morphologies. Seeded bottles were then filled with 32 g NaCl, 4 g Na_2SO_4, and 1 L ultrapure Milli-Q water (18.2 MΩ·cm) to produce a basic artificial seawater solution. Bottles were sonicated for 10 min to dissolve the NaCl and suspend barium sulfate nucleation seeds from the bottle walls into the artificial seawater solution. Larger barium sulfate crystals were then formed from the nucleation seeds through the addition of 2 mL 10 mM $BaCl_2$ to each bottle. Bottles were agitated and placed in a 4°C refrigerator overnight to facilitate ongoing barium sulfate microcrystal growth. The next day, 50 mL of barium sulfate/seawater solution was filtered through a 0.2 um pore size nylon membrane filter for each experiment/treatment. All filters were dried in a 50°C oven and stored until experiment set up.

Crystals were synthesized in one batch for the organic matter shielding experiment and one batch for the pH, salinity, and temperature experiments. We optimized for uniform barium

sulfate crystals to facilitate the reliable visual assessment of barium sulfate dissolution over time and to control for morphology or size effects on barite dissolution. Crystals made for the organic matter shielding experiment were larger than those for the pH, salinity, and temperature experiments, but, in both cases, crystals were fairly homogeneous in size and morphology within a synthesis batch (Figs. 14, 15).

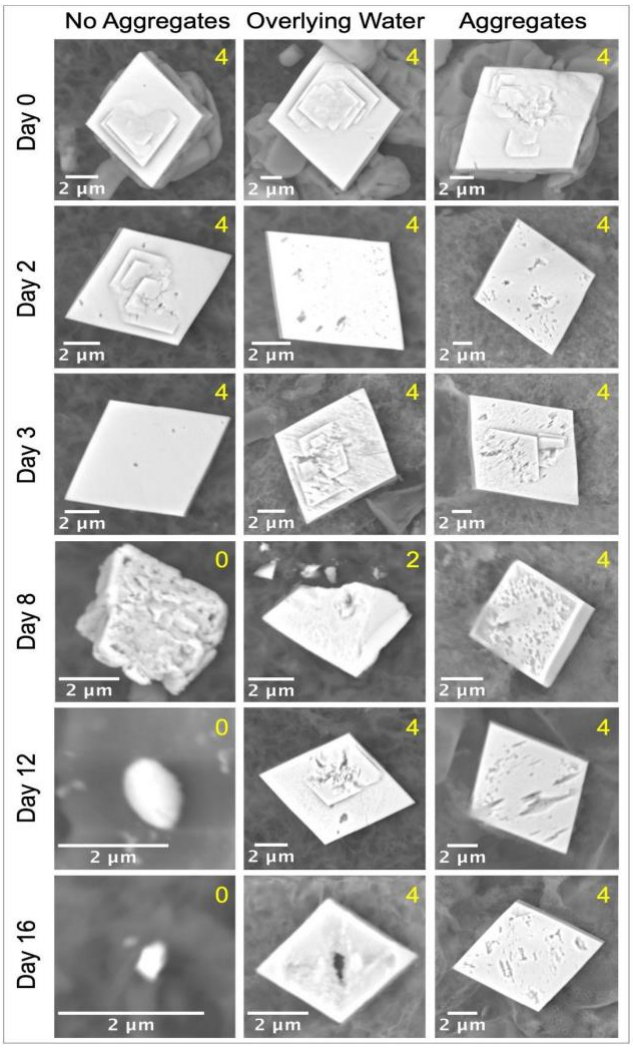

Figure 14. SEM images of representative barium sulfate microcrystals over time from No Aggregate, Overlying Water, and Aggregate treatments of the organic matter shielding experiment. Yellow numbers indicate the number of clearly visible, well-defined crystal faces assigned to each particle.

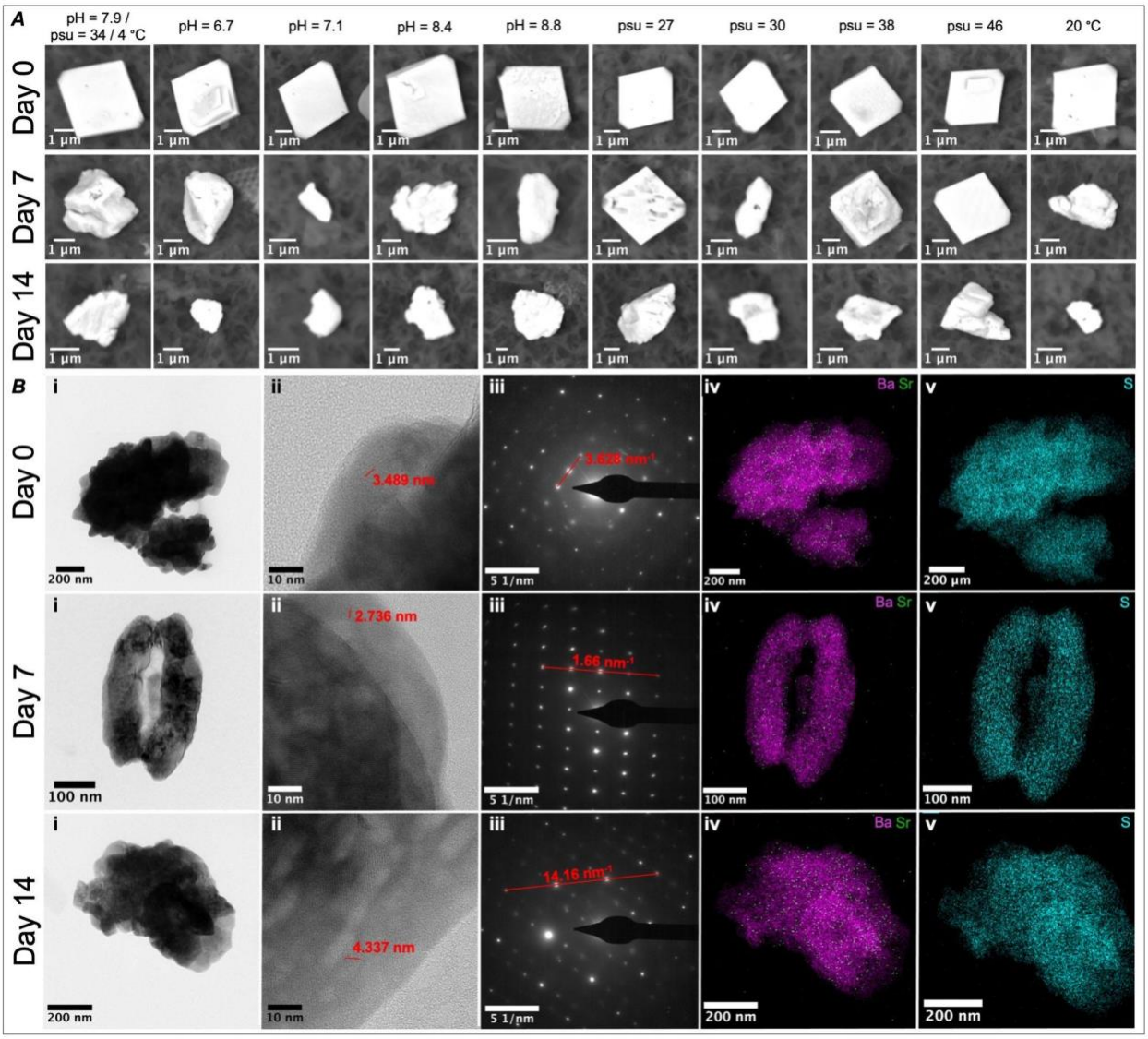

Figure 15. A) SEM images of representative barium sulfate microcrystals from pH, salinity, and temperature experiments on Day 0, Day 7, and Day 14. B) TEM results for select crystals from Day 0 (pH = 7.9/psu = 34/4 °C treatment), Day 7 (psu = 26.7 treatment), and Day 14 (pH = 7.9/psu = 34/4 °C treatment). i) HRTEM images. ii) Lattice fringe images, with ten unit cell annotations such that measurements in nm correspond to d-spacings in Å. iii) SAED patterns with characteristic d-space measurements. iv. Ba and Sr and v. S elemental composition maps.

Barium sulfate dissolutions rates with organic matter shielding experiment

Non-axenic phytoplankton cultures of the diatom *Thalassiosira weissflogii* were cultured to produce organic matter aggregates in 2 L flasks with f/2 media under a 12:12 h LED light/dark cycle. On day 10, the cell concentration in each culture was measured using a particle counter

(Multisizer 3, Beckman Coulter Counter). Cultures were diluted with filtered seawater to a concentration of 20,000 cells mL^{-1} and added to 5 custom-made 2.2 L cylindrical acrylic tanks. Six filters carrying synthesized barium sulfate crystals were each submerged in 50 mL filtered seawater and sonicated for 10 min to suspend the barium sulfate crystals. Filters were removed, and a barium sulfate suspension was added to each of the 5 cylindrical tanks prepared for aggregate formation and to an additional identical control tank containing only filtered seawater. The control tank was shaken and immediately sampled as described below for an initial time point. All 6 tanks were placed on a roller table and allowed to rotate at a speed of 3.3 rpm, allowing for the formation of aggregates by the diatom cultures. The roller table incubation was conducted at room temperature (20–22°C) and in the dark to prevent any further phytoplankton growth. This method has been widely used in previous studies to form aggregates from phytoplankton in the laboratory (e.g., Prairie et al., 2019).

Subsequent sampling was conducted 2, 3, 8, 12, and 16 days after aggregate formation began (i.e., after tanks were placed on the roller table). For the control tank, 10 mL was sampled via syringe and filtered through a 25 mm diameter 0.2 um pore size nylon membrane filter; this sample became the No Aggregate treatment filter. The filter was then rinsed with 10 mL Milli-Q water to prevent crystallization of salt. Filtered seawater was added to the tank to replace the sampled volume.

For the tanks with aggregates, 1 randomly selected tank was destructively sampled on each sampling day. The tank was removed from the roller table. Organic aggregates were allowed to settle to the bottom of the tank for 2 min, after which 10 mL overlying water was immediately sampled as described above for the control tank to form the Overlying Water treatment filter.

Organic matter aggregates that had settled to the bottom of the tank were photographed on a mm-square grid sealed on the bottom of the roller tank (Supplementary Information 3.1). Aggregates were then individually removed from the tank using a volumetric pipette with a cut-off tip. The total volume of aggregates from that tank was approximated, and aggregates were filtered through a single 47 mm diameter 0.2 μm pore size polycarbonate membrane filter. The filter made from the aggregates became the Aggregate treatment filter of each experimental tank. The filter was rinsed with 20 mL Milli-Q water to prevent crystallization of salt. All filters were dried and stored until later analysis.

Barium sulfate dissolution rates with varying pH, salinity, and temperature experiments

In addition to the organic matter shielding experiment, we also studied the effects of pH, salinity, and temperature on barite dissolution. Filtered seawater was modified as necessary to achieve 10 experimental treatments (Table 3). pH was adjusted through additions of 0.1 M HCl and 0.1 M NaOH. Salinity was modified by dilution with Milli-Q water or concentration by evaporation over a hotplate. Salinity treatments were then pH adjusted as necessary to replicate unmodified seawater pH. We measured pH and salinity using a multiparameter meter (ProQuatro, YSI). Concentrations of major cations and anions in each experimental treatment were estimated by assuming linear dilution/concentration based on salinity using average seawater values from Emerson and Hedges (2008) (Supplementary Information 3.1). Barium concentrations were estimated from linear dilution/concentration from previously published coastal San Diego seawater barium measurements (Esser and Volpe, 2002) (Supplementary Information 3.1). These seawater chemistry estimates were used to calculate barite saturation indices for each treatment on The Geochemist's Workbench software (Version 17.0.1; Bethke et

al., 2022) using the default thermo.tdat database compiled by Lawrence Livermore National Laboratory (Delany and Lundeen, 1991).

Table 3. pH, salinity, temperature, and estimated barium sulfate saturation state for barium sulfate dissolution rate experimental treatments. pH = 7.9/psu = 34/4 °C and 20 °C treatments used unmodified filtered seawater, and pH and/or salinity were adjusted for all other treatments.

Treatment	**pH**	**Salinity**	**Temperature (**°C)	$\boldsymbol{\Omega_{BaSO_4}}$
pH = 7.9/psu = 34/4 °C	7.87	33.78	4	0.44
pH = 6.7	6.65	33.17	4	0.44
pH = 7.1	7.07	33.46	4	0.44
pH = 8.4	8.42	33.57	4	0.44
pH = 8.8	8.81	33.45	4	0.44
psu = 27	7.90	26.67	4	0.34
psu = 30	7.97	30.04	4	0.39
psu = 38	7.95	38.18	4	0.50
psu = 46	7.96	45.97	4	0.62
20 °C	7.92	33.80	20-22	0.19

1 L modified seawater from each treatment was added to a 1 L polycarbonate bottle for the incubation. A 50 mL aliquot from each treatment was added to a centrifuge tube with a filter carrying the previously synthesized barium sulfate crystals. Tubes were sonicated for 10 min to

resuspend the barium sulfate crystals, and the filters were removed. The contents of each tube were returned to the corresponding seawater treatment bottle, and bottles were agitated. The room temperature treatment was incubated in the dark at room temperature (20–22°C), and all other bottles were incubated in a dark 4°C refrigerator for the remainder of the experiment. Sampling was conducted immediately following experiment set-up and after 7, 14, 21, 28, and 35 days. Bottles were shaken to completely mix them. Then, 50 mL was removed from each bottle and filtered through a 25 mm diameter 0.2 um pore size nylon membrane filter. All filters were dried and stored until later analysis.

SEM analysis

Barium sulfate crystal quantity, size, and morphology across treatments and over time were assessed via Scanning Electron Microscopy equipped with Energy-dispersive X-ray Spectroscopy (SEM-EDS). Approximately 1 cm^2 of each filter was mounted on an aluminum stub with carbon tape for analysis. Analyses were conducted using a Phenom Desktop SEM with an accelerating voltage of 15 kV, vacuum of 1 Pa, and working distance of 9–10 mm (Scripps Institution of Oceanography).

For the organic matter shielding experiment, 5 randomly selected fields were quantitatively analyzed for each filter. Fields were 0.82–0.91 mm^2 for No Aggregates and Overlying Water treatments. Fields were 0.21–0.44 mm^2 for the Aggregate treatment due to the much higher density of barium sulfate crystals on these filters. A backscatter electron detector was used to systematically identify all potential barium sulfate crystals within each field by their high atomic number. Identification was confirmed by EDS, and all barium sulfate crystals were imaged. For the pH, temperature, and salinity experiments, potential barium sulfate crystals were identified, their identity was confirmed, and crystals were imaged. The process was

repeated until either 15–20 crystals were imaged (28 out of 36 filters) or all visible barium sulfate crystals on the stub were imaged (8 out of 36 filters).

Barium sulfate crystal morphology was assessed via visual image analysis. For the organic matter shielding experiment, images were visually assessed to assign each crystal with its number of clear, well-defined crystal edge faces (Fig. 15). Since crystal surface topography was not always visible, the upward-facing crystal face oriented toward the viewer was not included in these assessments. For both experiments, crystal size was quantitatively determined using the Fiji distribution of ImageJ (Schindelin et al., 2012, Schindelin et al., 2015). Scaling parameters were extracted from the metadata of each image. Barium sulfate crystals were distinguished from the filter background using the Trainable Weka Segmentation plugin (Arganda-Carreras et al., 2017). Fiji's Analyze Particles plugin was then used to calculate the area, Feret diameter, and best fit ellipse major and minor axis lengths for each crystal. For the organic matter shielding experiment, barium sulfate quantity in each field, defined as total area hereafter, was determined by adding together the areas of every crystal observed in each field. Total area for each field was corrected for the corresponding sample volume according to the equation

$$T = \frac{S \times A_T}{A_F \times V}$$

where T is the total area for a field, S is the sum of individual barium sulfate crystal areas in that field, A_T is the area of the filter, A_F is the area of the field, and V is the volume of seawater filtered through the corresponding filter.

To estimate the mass of barium sulfate crystals imaged, we assumed that barium sulfate crystals with 2 or more well-defined crystal faces had the idealized barite habit of Goldschmidt (1913) barite no. 325, which is most consistent with the rhomboidal two-dimensional barium

sulfate images acquired via SEM. We assume that these crystals were imaged from their (0,0,1) face, so crystal thickness in the direction not visible on the SEM was equivalent to the width of the (2,1,0) face. The volume of the crystal, V, can then be estimated by

$$V = A \times c \times L$$

where A is the crystal area visible from the SEM image, c is 0.283, a constant derived from the relative dimensions of crystal thickness: length (crystal axes c: a) of idealized barite no. 325 (Goldschmidt, 1913), and L is the length of the crystal as determined by the Feret diameter. For barium sulfate crystals with 1 or 0 well-defined crystal faces, we assumed that three-dimensional shape could be approximated as an ellipsoid of rotation around the major axis of the best-fit ellipse of each crystal's two-dimensional outline. Crystal volume, V, can then be estimated by

$$V = \frac{4}{3} \times \pi \times \frac{y}{2} \times (\frac{x}{2})^2$$

where y and x are the length and width of the best-fit ellipse, respectively. We then used the density of barium sulfate, 4.48 g cm^{-3}, to calculate the mass of each barium sulfate crystal based on their estimated volume. The average area per barium sulfate crystal is shown in the Supplementary Material (Supplementary Information 3.2, 3.3).

HRTEM analysis

A subsample of pH, salinity, and temperature experiment filters were analyzed via high resolution transmission electron microscopy (HRTEM) to assess the crystallinity of barium sulfate crystals over time. The following filters were analyzed: pH = 7.9/psu = 34/4°C (Days 0, 7, and 14), pH = 6.7 (Day 7), and psu = 26.7 (Day 7). One quarter of each filter was suspended in ethanol and ground with an agate mortar. Particulate matter suspended in this ethanol was then deposited on carbon-film-coated copper grids. Barium sulfate crystals on these grids were imaged using a FEI TITAN G2 60–300 microscope with a high brightness electron gun (X-FEG)

operated at 300 kV and equipped with a Cs image corrector CEOS (Center for Scientific Instrumentation, University of Granada). Elemental composition maps were acquired using a SUPER-X silicon-drift windowless EDX detector. Selected area electron diffraction (SAED) patterns were also collected on barium sulfate crystals. Two to four crystals were imaged for each filter. HRTEM sample preparation preferentially selects for smaller crystals, so only SEM images were used to evaluate barium sulfate crystal size and morphology.

Statistical analyses

ANCOVAs were conducted to compare the rate of change of experimental parameters between treatments over time. For the organic matter shielding experiment, ANCOVAs were conducted on cube root transformed total area, natural log transformed mass per crystal, and average number of crystal faces per field over time. Since no organic matter aggregates were present on Day 0, crystal total area, mass per crystal, and crystal face measurements from the No Aggregate treatment were used as the initial time point for Aggregate and Overlying Water treatments as well. For pH, salinity, and temperature experiments, ANCOVAs were conducted to compare the rate of change in estimated mass per crystal over time between treatments. Mass per crystal was cube root transformed, square root transformed, and natural log transformed for pH, salinity, and temperature data, respectively. Across all experiments, linear regressions were conducted for each treatment when rates of change appeared to significantly differ between treatments. Linear regressions were conducted across treatments when no significant interaction effect was observed. For total area, all treatments were cube root transformed. For mass per crystal, No Aggregate and Aggregate treatments were square root transformed, and the overlying water treatment was natural log transformed. For number of crystal faces, all treatments were square root transformed. For all data, assumptions of normality and homoscedasticity were

assessed via Q-Q and residual-fitted plots. All statistical analysis was performed in R Version 3.6.3 (R Core Team, 2020), and the ggplot package was used for data visualization (Wickham, 2016).

Barite sinking velocity calculations

An idealized spherical pelagic barite crystal was used to calculate an approximate barite sinking velocity through the water column. Sinking velocity was calculated according to Stokes' law

$$S_V = \frac{2}{9} \times g \times r^2 \times \frac{\rho_{barite} - \rho_{seawater}}{\eta_{seawater}}$$

where S_V is sinking velocity, g is Earth's gravitational acceleration (9.81 m s^{-2}), r is the radius of the sphere, $\boldsymbol{\rho}_{barite}$ is the density of barite (4480 kg m^{-3}), $\boldsymbol{\rho}_{seawater}$ is the density of seawater, and $\eta_{seawater}$ is the dynamic viscosity of seawater. The radius of the sphere was calculated from a crystal area of 0.90 ± 0.03 μm^2, the average area of intermediate depth pelagic barite crystals in the North Pacific (Light and Norris, 2021). $\boldsymbol{\rho}_{seawater}$ and $\eta_{seawater}$ values for seawater with salinity of 35 g kg^{-1} at a temperature of 10°C were used (Nayar et al., 2016; Sharqawy et al., 2010). The Reynolds number (R_e) of this idealized barite crystal was calculated using

$$R_e = \frac{2 \times \rho_{seawater} \times S_v \times r}{\eta_{seawater}}$$

to determine if Stokes' Law applied to the sinking particle. R_e was <0.1, so Stokes' Law does apply (McNown and Malaika, 1950).

Results

Barium sulfate dissolutions rates with organic matter shielding

Immediately following experiment set-up, most (> 90%) barium sulfate crystals formed regularly-shaped rhombuses with 4 clear, well-defined crystal edge faces (Fig. 16). Most initial

crystals displayed stair-stepped surface topography (Fig. 16). Organic matter aggregates were visible in all phytoplankton tanks by day 2 of the incubation and became smaller and better-defined over time (Supplementary Information 3.1). Barium sulfate crystals from the Aggregate treatment showed little change in morphology over the course of the incubation. The only observed change in crystals removed from the Aggregate treatment was that stair-stepped surface topography was less common and pitted surface topography was more common later in the incubation (Fig. 16). Crystals from the Overlying Water treatment crystals displayed a mixture of rhomboidal and irregular morphologies by day 3, with some crystals displaying pits and other visual evidence of dissolution (Fig. 16). By day 8, most barium sulfate crystals from the No Aggregate treatment displayed irregular morphologies (Fig. 16).

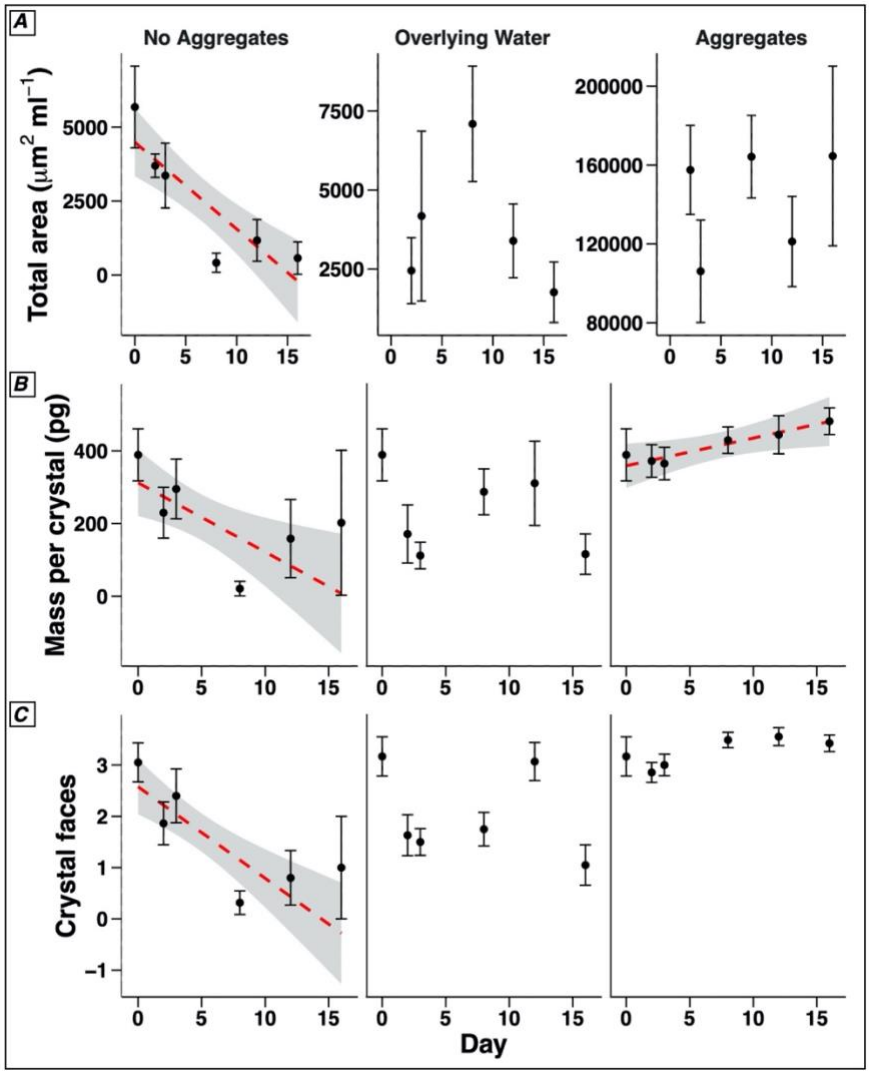

Figure 16. Barium sulfate A) total area per field, B) mass per crystal, and C) average number of well-defined crystal faces per field over time for No Aggregates, Overlying Water, and Aggregate treatments of the organic matter shielding experiment. Red dashed lines show fitted linear regression curves with standard error in gray for all parameters with a statistically significant ($p < 0.05$) change over time (see Table 4 for statistics and regression values).

The rate of change for total crystal area, mass per crystal, and average number of crystal faces over time depended on experimental treatment (ANCOVAs; $F_{2,74} = 5.266$, $p = 0.007$; $F_{2,584} = 15.569$, $p < 0.001$; and $F_{2,80} = 5.918$, $p = 0.004$, respectively). Total crystal area decreased over time for the No Aggregate treatment and did not significantly change over time for the Overlying Water or Aggregate treatments (Table 2). Mass per crystal decreased over time

for the No Aggregate treatment, increased over time for the Aggregate treatment, and did not significantly change over time for the Overlying Water treatment (Table 2). The number of crystal faces significantly declined over time for the No Aggregate treatment, but no significant change over time was observed for the other treatments (Table 2).

Table 4. Linear regression values for No Aggregate, Overlying Water, and Aggregate treatments of the organic matter shielding experiment. Regressions were calculated with time in days as the independent variable.

Regression	**F**	**df**	**P-value**	**r^2**	**m**	**b**
Total area (μm^2 ml^{-1})						
No Aggregates	34.57	1, 28	< 0.001	0.55	-290 ± 60	4500 ± 600
Overlying Water	0.49	1, 23	0.492	0.02	-	-
Aggregates	0.08	1, 23	0.774	0	-	-
Mass per crystal (pg)						
No Aggregates	13.50	1, 90	< 0.001	0.13	-19 ± 7	310 ± 50
Overlying Water	2.74	1, 158	0.100	0.02	-	-
Aggregates	7.40	1, 336	0.045	0.01	8 ± 3	360 ± 30
Crystal faces						
No Aggregates	13.47	1, 24	0.001	0.36	-0.15 ± 0.05	2.8 ± 0.4
Overlying Water	0.18	1, 28	0.679	0.01	-	-
Aggregates	1.83	1, 28	0.187	0.06	-	-

Barium sulfate dissolution with varying pH, salinity, and temperature

On day 0, most (> 95%) barium sulfate crystals were regularly shaped rhombuses (Fig. 15). On day 7, approximately half of observed crystals were rhomboidal and half displayed

irregular morphologies (Fig. 15). On day 14, approximately 90% of crystals displayed irregular morphologies, and some crystals displayed etching and dissolution pits (Fig. 15). Beginning on day 21, barium sulfate crystals across treatments displayed globular morphologies and were larger than crystals from day 0 (Supplementary Information 3.4). These large, globular morphologies suggested that the aggregation of barium sulfate microcrystals had occurred, so samples from day 21 and later were excluded from subsequent analyses. All barium sulfate crystals analyzed via HRTEM displayed well-defined crystallinity (Fig. 15). Lattice-fringe images and SAED patterns yielded d-space measurements consistent with barium sulfate. There was no significant difference in the rate of change in crystal mass over time between treatments for pH, salinity, and temperature variation experiments (ANCOVAs, $F_{1,227} = 2.903$, $p = 0.090$; $F_{1,204} = 0.603$, $p = 0.438$; $F_{1,91} = 3.261$, $p = 0.074$, respectively). Since there was no significant difference in the rate of change between treatments, we conducted a single regression for each treatment to determine the overall rate of change in crystal mass over time. These regressions revealed that crystal mass significantly decreased over time across treatments for all three experiments (Fig. 17, Table 5).

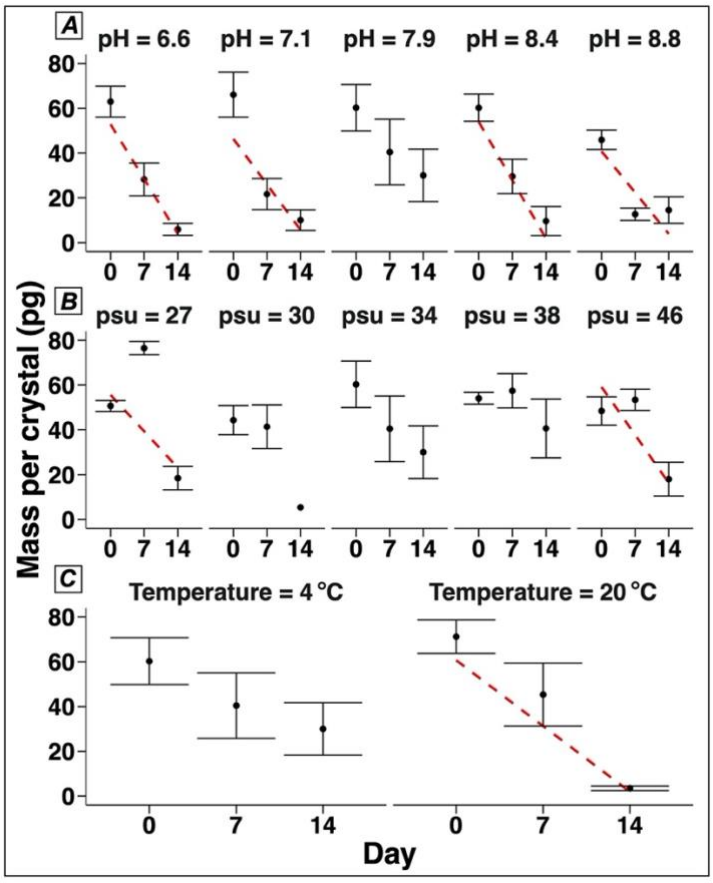

Figure 17. Barium sulfate mass per crystal over time for free crystals in the A) pH, B) salinity, and C) temperature variation experiments. Red dashed lines show fitted linear regression curves for each treatment with a statistically significant ($p < 0.05$) change over time (see Supplementary Information 3.2 for regression values). Interaction between treatment and rate of change in crystal mass over time was insignificant for all three experiments, so treatment-specific regressions were calculated for visualization purposes only. Regression for each experiment are presented in Table 5.

Table 5. Linear regression values for pH, salinity, and temperature experiments. A single regression was conducted using data from all treatments within each experiment. Regressions were calculated with time in days as the independent variable and crystal mass as the dependent variable.

Regression	F	df	P-value	r^2	m (pg)	b (pg)
pH	139.4	1, 229	< 0.001	0.38	-3.2 ± 0.4	56 ± 3
Salinity	28.9	1, 206	< 0.001	0.12	-1.7 ± 0.4	54 ± 4
Temperature	23.6	1, 93	< 0.001	0.20	-3.4 ± 0.8	66 ± 7

These results can be used to estimate how long typical pelagic barite crystals survive in the ocean water column. We observed barium sulfate dissolution rates ranging from 19 ± 7 pg day^{-1} for the No Aggregates treatment of the organic matter shielding experiment (Table 4) to 1.7 ± 0.4 pg day^{-1} for the salinity variation experiment (Table 5). Thus, we can use the slowest dissolution rate from the salinity variation experiment to estimate an upper threshold for average pelagic barite crystal survival time. The mean mass per crystal of pelagic barite was 10.0 ± 2.4 pg and 10.6 ± 2.2 pg in surface sediments collected from the North Pacific and North Atlantic, respectively (Robin et al. 2003). At a dissolution rate of 1.7 ± 0.4 pg day^{-1}, barite crystals of mean mass would entirely dissolve after 5.9 ± 0.3 and 6.2 ± 0.3 days. Crystals would last only half a day under the faster rate of dissolution suggested by the No Aggregates treatment.

We can compare these estimated survival times to the approximate amount of time it takes a typical pelagic barite crystal to sink down through the water column. The estimated sinking velocity of an average-sized pelagic barite crystal (length 1.08 μm; see Methods for details) is 0.14 m day^{-1}. At this sinking velocity, a barite crystal would sink only 87 ± 4 cm from its point of formation in 6.2 ± 0.3 days, or the estimated average barite survival time calculated

above. In contrast, a pelagic barite crystal sinking at a velocity of 0.14 m day^{-1} would take 67 years to sink from a point of formation at 200 m depth to a seafloor depth of 3,500 m.

Discussion

Rapid dissolution of free barium sulfate crystals

Barium sulfate crystal quantity, mass and morphology over time across all experiments suggest that barium sulfate crystals not encased within organic matter aggregates dissolve within days when exposed to surface ocean seawater. We observed statistically significant declines in crystal total area and mass per crystal for all experiments and treatments without organic matter aggregates (Figs. 14-17). Additionally, the enumeration of well-defined faces for each crystal provided a quantitative measure for the qualitative observation that barium sulfate crystal morphology changed over time (Fig. 16). Since most barium sulfate crystals displayed four well-defined crystal edge faces at the beginning of the incubation, subsequent declines in the number of crystal faces were likely due to dissolution. HRTEM analyses confirm that barium sulfate crystals displayed a high degree of crystallinity throughout the incubation, so the observed changes in morphology were due to crystal dissolution (Fig. 15). A range of crystal sizes and morphologies were observed within each treatment on any given day (Figs. 15, 16), which suggests that there is natural variability in barium sulfate dissolution. Our analyses of covariance revealed no statistically significant changes in the rate of barium sulfate dissolution with pH, salinity, or temperature over time (Fig. 17).

While barium sulfate dissolution was observed across all treatments without organic matter aggregates, rates of dissolution did vary between experiments. The rate of dissolution in the salinity experiment was slightly slower than that of the pH and temperature experiments (Table 5). This may be a function of sampling variability, particularly since we imaged a

relatively small number of crystals for each treatment. The rate of barium sulfate dissolution in the No Aggregate treatment of the organic matter shielding experiment was higher than that of the pH, salinity, or temperature experiments. The organic matter shielding experiment was conducted at room temperature on a roller table, so the No Aggregate treatment crystals likely dissolved more quickly in part because they were exposed to fluid resistance resembling a crystal sinking down through the ocean water column. While we did not observe a statistically significant difference in barium sulfate dissolution rate in our temperature variation experiment, the higher temperature of the organic matter shielding experiment may have also contributed the more rapid dissolution rate in this treatment.

Since we only directly measured changes in barium sulfate crystal area over time, our experiments are limited in their ability to provide detailed insights into the kinetics of barium sulfate dissolution in seawater. However, we can use our estimates of barium sulfate mass loss over time combined with estimated surface area per crystal on Day 0 to determine surface area normalized rate of barium sulfate dissolution (Supplementary Information 3.3). The surface area normalized dissolution rates we observed were slightly slower than those reported for similar experiments in Zhen-Wu et al. (2016). For example, we calculated a surface area normalized dissolution rate of $-0.7 \pm 0.3 \times 10^{-8}$ mol m^{-2} s^{-1} for the No Aggregate treatment, while a rate constant from Zhen-Wu et al. (2016) predicts a barium sulfate dissolution rate of -2.2×10^{-8} mol m^{-2} s^{-1} in a 1 mol kg^{-1} NaCl solution with an equivalent Ω_{BaSO_4} (Supplementary Information 3.3). Zhen-Wu et al. (2016) observed modest changes in barium sulfate dissolution rate with pH and larger changes with increased ionic strength and temperature. However, these experiments were conducted using a wider range of pH, ionic strength, and temperature conditions than those found in the natural seawater. Our experiments suggest that barium sulfate

dissolution rate varies little within commonly observed ocean pH, salinity, temperature conditions, but a more rigorous investigation into the kinetics of barium sulfate dissolution in seawater would be helpful for further constraining these relationships.

Additionally, we conducted our experiments with synthetic barium sulfate rather than naturally occurring pelagic barite, so our experiments are limited in their ability to fully reproduce pelagic barite dissolution in the water column. In some ways, the use of synthetic barium sulfate crystals likely underestimates pelagic barite dissolution. Synthetic barium sulfate crystals likely lacked structural defects that occur in naturally occurring pelagic barite (Light and Norris, 2021; Sun et al., 2015), so they may have been less susceptible to dissolution. Similarly, our barium sulfate crystals were formed in the absence of Sr^{2+} and other trace elements, but pelagic barite contains 10 mg strontium per g of barite on average (Averyt and Paytan, 2003). Strontium incorporation increases the solubility of pelagic barite relative to pure barium sulfate (Monnin and Cividini, 2006; Rushdi et al., 2000; Widanagamage et al., 2014), so this may lead to an underestimation of pelagic barite dissolution rates. Pelagic barite is also 5–15 times smaller than the barium sulfate crystals we observed at the beginning of our experiments (Figs. 14, 15; Bertram and Cowen, 1997; Light and Norris, 2021), so pelagic barite generally has a larger surface area to volume ratio than our synthetic crystals. The larger size of our synthetic crystals compared to marine crystals may have led to slower observed dissolution rates because dissolution is dependent on crystal surface area (e.g., Lüttge, 2005) and increases with decreasing crystal size (Briese et al., 2017). In contrast with these other discrepancies, the morphology of our synthetic barium sulfate crystals may have caused our rates to overestimate pelagic barite dissolution. Pelagic barite is generally ellipsoidal, but our experimental crystals were euhedral (Figs. 14, 15; Bertram and Cowen, 1997; Light and Norris, 2021). Dissolution is

enhanced at crystal edges (Trindade Pedrosa et al., 2019), so pelagic barite may have dissolved more slowly than our synthetic crystals under the same experimental conditions.

Despite these limitations, we can use our observations to estimate plausible pelagic barite dissolution rates in the water column. Our findings suggest that variation in pelagic barite dissolution rates with pH, salinity, and temperature is very small relative to the difference between estimated barite crystal survival and sinking times in the water column. The longest estimated survival time suggested by our experiments for an average pelagic barite crystal (6.2 ± 0.3 days) is much shorter than the estimated time that it would take the average pelagic barite crystal to sink down 3300 m to the seafloor (67 years). The coastal, surface ocean seawater used in our incubations likely had a lower barite saturation state than deep seawater in much of the ocean (Mete et al., 2023). However, most pelagic barite precipitation occurs within the upper 1000 m of the water column, where barite undersaturation is widespread (Carter et al., 2020). Therefore, pelagic barite survival in the upper ocean is vital to barite transport throughout the water column. Our measured barium sulfate dissolution rates across a range of feasible seawater pH, salinity, and temperature conditions suggest that free pelagic barite is unlikely to survive transit through an ocean water column.

The changes in barium sulfate crystal size and morphology observed in the pH, temperature, and salinity experiments between days 14 and 21 suggest barium sulfate microcrystal aggregation began to occur in these treatments. While all treatments were undersaturated with respect to barium sulfate at the beginning of the experiment (Table 3), ongoing barium sulfate dissolution during the experiment released both Ba^{2+} and SO_4^{2-} into the ambient seawater. We did not monitor the concentration of Ba^{2+} and SO_4^{2-} in the ambient seawater over time. However, since we added up to 1 μmol barium sulfate to each treatment at

the beginning of the experiment and observed considerable barium sulfate dissolution over time (Fig. 17), it is likely that the ambient seawater was at or near barium sulfate saturation by day 21. Barium sulfate microcrystal aggregation and nonclassical growth is well-documented (e.g., Judat and Kind, 2004; Kügler et al., 2015; Marchisio et al., 2002), so the aggregation of partially dissolved barium sulfate crystals may have been facilitated by these conditions. This transition from barium sulfate dissolution to aggregation highlights a shortcoming in our experimental design, particularly over longer time scales. Future investigations should consider maintaining a constant degree of barium sulfate undersaturation throughout the experiment by tracking Ba^{2+} and SO_4^{2-} concentrations over time and diluting treatments as needed. We would have likely observed even greater rates of barium sulfate dissolution if we had taken such measures.

Organic matter aggregates shield barium sulfate crystals from dissolution

Barium sulfate crystal quantity, mass, and morphology over time in the organic matter shielding experiment suggest that organic matter aggregates protect barium sulfate from dissolution in seawater undersaturated with respect to seawater. Barium sulfate crystals sampled from the Overlying Water treatment showed no statistically significant changes in size or morphology over the course of the incubation. The only statistically significant change observed for the Aggregate treatment was a small increase in mass per crystal for the average population of crystals within aggregates (Table 4 and Fig. 16). The only visibly observable change in barium sulfate crystals over time for Aggregate and Overlying Water treatments was a slight change in surface topography (Fig. 14), which suggests that barium sulfate dissolution may occur within organic matter aggregates but over much longer time scales than those studied here. Organic matter aggregates likely shield barium sulfate from dissolution through physical and chemical mechanisms, both in our experiments and in the ocean water column. Interstitial flow

through organic matter aggregates is limited (Ploug et al., 2002; Zetsche et al., 2020), so aggregates form a physical barrier that may protect barite from fluid resistance from the water column. Small-scale chemical gradients can form within sinking aggregates (Alldredge and Silver, 1988; Ploug, 2001), so aggregates may also shield barite from dissolution by limiting diffusion and creating microenvironments with higher barite saturation states than the surrounding water column. Aggregates are held together by extracellular polymeric substances (EPS), which have been shown to bioaccumulate Ba^{2+} (Martinez-Ruiz et al., 2018). It is possible that this bioaccumulation not only facilitates pelagic barite precipitation but also subsequently protects crystals from dissolution.

While sinking velocities were not experimentally tested here, incorporation into aggregates likely also promotes pelagic barite preservation by increasing the sinking velocities of crystals. Settling velocities for organic matter aggregates range from 10 to 1000 m day^{-1} depending on the characteristics of the aggregate (e.g., Iversen and Ploug, 2010; Laurenceau-Cornec et al., 2020). These velocities are 70–7000 times faster than the estimated sinking velocity for an average-sized free barite crystal. Similarly, the incorporation of high-density pelagic barite crystals into organic matter aggregates may increase their sinking velocity. Experiments show that ballast materials such as opal and atmospheric dust increase the sinking velocity of aggregates, so pelagic barite may also be an effective aggregate ballast (Iversen and Ploug, 2010; van der Jagt et al., 2018).

The similarities between barium sulfate crystals in the Aggregate and Overlying Water treatments (Figs. 14, 16) suggest that even very small organic matter aggregates or transparent exopolymeric particle (TEP) films coating barium sulfate crystals are sufficient to shield crystals from dissolution. While our Overlying Water treatment samples contained few, if any, visible

organic matter aggregates, they undoubtedly contained subvisible aggregates and TEP. Shielding by these smaller particles likely explains the limited dissolution of Overlying Water treatment crystals (Figs. 14, 16), and these results suggest that subvisible marine particles also play a role in pelagic barite dynamics.

In our incubation and in natural seawater, marine organic matter aggregates grow over time through coagulation, or the collisions of smaller particles due to processes such as fluid shear, Brownian motion, and particle settling (Alldredge and Jackson, 1995). These processes, combined with the stickiness of EPS, likely explain how barium sulfate was efficiently incorporated into aggregates, since total barium sulfate area was much higher in Aggregate treatment filters than the other treatments (Fig. 16). Ongoing coagulation may also explain the increase in mass per crystal over time for the average population of crystals within aggregates (Fig. 16). Earlier in the incubation, aggregates likely incorporated some smaller crystals which had undergone partial dissolution in the surrounding seawater before colliding with an aggregate. By the end of the incubation, many of these surrounding crystals had likely dissolved completely, so the average population of Aggregate treatment barite included fewer of these smaller crystals.

Implications for the barite proxy

Together, these findings suggest that organic matter aggregates are vital to the survival of pelagic barite crystals as they sink through seawater undersaturated with respect to barite (Fig. 18). When barite crystals precipitate within aggregates but those aggregates then disintegrate, the barite crystals will likely dissolve well before they sink to the seafloor. The fraction of aggregates that survive transit through the water column is poorly constrained. However, aggregates are well-known to represent hotspots for bacterial activity (e.g., Ziervogel et al.,

2010) and a common food source for zooplankton (e.g., Cawley et al., 2021). Due to these pressures, much of the organic matter within aggregates is remineralized as these aggregates sink through the water column (DeVries and Weber, 2017; Sanders et al., 2014). Therefore, most pelagic barite crystals will dissolve before they reach the seafloor, as is consistent with prior mass balance estimates (Paytan and Kastner, 1996).

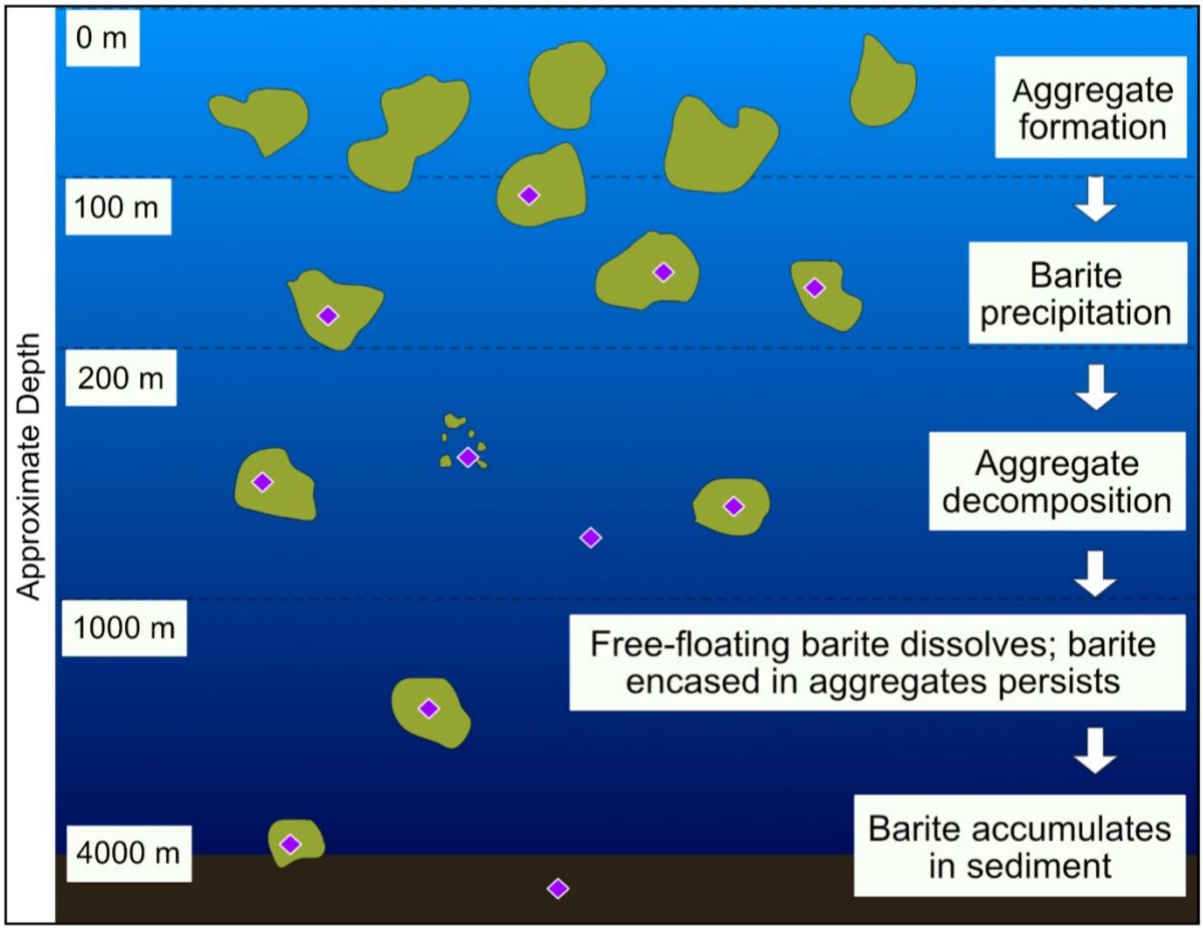

Figure 18. Schematic illustrating the proposed role of organic matter aggregates (depicted in green) in protecting pelagic barite crystals (depicted as purple diamonds) from dissolution in the water column. Schematic is not to scale, and water depths are approximate as each of the processes listed occur over a wide range of depths.

Under this hypothetical scenario, the free barite crystals that are observed in the water column (e.g., Light and Norris, 2021; Xiao et al., 2022) have likely been recently released by

organic matter aggregates that have been degraded or fragmented. A small fraction of these free crystals may be incorporated into other aggregates, given their stickiness and rapid sinking velocity compared to crystals. However, since aggregate formation occurs primarily in surface waters (Simon et al., 2002), most barite particles released into seawater undersaturated with respect to barite likely dissolve. This suggests that microbial activity and associated EPS production play an essential role in both pelagic barite formation (Gonzalez-Muñoz et al., 2012; Martinez-Ruiz et al., 2019; Torres-Crespo et al., 2015) and pelagic barite preservation. Our findings also show that seawater properties such as pH, salinity, and temperature have a much smaller effect on barite dissolution than a crystal's association with an organic matter aggregate. This increases our confidence in pelagic barite as a reliable, widely applicable carbon cycle proxy.

Nonetheless, the impact of spatial variability in water column barite dissolution on sediment barite accumulation rates and proxy interpretations should be explored. Recent work shows that micro-scale barite dissolution and precipitation fractionate Ba isotopes (Middleton et al., 2023), so the shielding of barite crystals by organic matter aggregates may also have implications for barite as a record of Ba isotopes. The factors influencing pelagic barite dissolution at the sediment-water interface also warrant further study. Finally, the role of subvisible TEP particles in shielding barite crystals from dissolution bears further analysis since our experiments suggest that crystals experimentally exposed to diatom cultures but not associated with large aggregates were also protected from dissolution.

An important implication of our findings is that the sediment pelagic barite proxy is likely to most closely track not organic matter remineralization or export out of the surface ocean but rather the flux of organic matter aggregates to the sediment-water interface. Our laboratory

experiments are inherently limited in their ability to recreate marine conditions, so this hypothesis must be tested in the field. Previous proxy calibrations have compared the accumulation rate of pelagic barite in marine sediments to surface ocean productivity or export production (Hayes et al., 2021; Eagle et al., 2003; Paytan et al., 1996). If pelagic barite crystals require shielding by organic matter aggregates to survive transport through the water column, we would expect pelagic barite accumulation rates to correlate more closely with proxies for the arrival of organic matter to the seafloor. These proxies include the abundance of benthic foraminifera, organic carbon, organic phosphorous, calcium carbonate, and opal in core top sediments (e.g., Brummer and Van Eijden, 1992; Bareille et al., 1991; Loubere, 1991; Pedersen and Calvert, 1990; Schenau and De Lange, 2001). However, these proxies have their own limitations in terms of preservation (e.g., Calvert and Pedersen, 2007; Ragueneau et al., 2000; Schoepfer et al., 2015), and pelagic barite formation is linked to microbial activity and EPS formation, which is not always well-correlated with foraminifera production (e.g., Martinez-Ruiz et al., 2020).

Some previous investigations have presented collocated core top Ba or barite data along with one or more of the other proxies listed above, allowing us to test our hypothesis (Hayes et al., 2021; Schoepfer et al., 2015; Serno et al., 2014; Shen et al., 2023). Reanalysis of these datasets yields mixed results, with excess barium sometimes showing stronger positive correlations with organic matter accumulation proxies than surface-based measures of productivity (Supplementary Information 3.4). A larger scale investigation specifically targeted at comparing core top pelagic barite accumulation with multiple other carbon cycle proxies from a variety of locations is likely needed to reliably assess which water column processes are recorded by sediment barite abundance.

If our hypothesis regarding the water column dissolution of free barite crystals is correct, it may undermine recent interpretations of some paleoceongraphic records. Griffith et al. (2021) and Diester-Haass and Faul (2019) found that pelagic barite accumulation rates were decoupled from benthic foraminiferal accumulation rates during Eocene hyperthermals in the South Atlantic and in the Paleogene Southern Ocean, respectively. These studies attributed this decoupling to pelagic barite recording export production out of the mesopelagic and benthic foraminifera recording the supply of organic matter and therefore food to the seafloor (Diester-Haass and Faul, 2019, Griffith et al., 2021). They suggest that these parameters diverge when there is a change in an ecosystem's transfer efficiency, or the fraction of organic matter that is exported out of the euphotic zone that reaches the deep ocean. This explanation relies on pelagic barite crystals surviving transit through the water column even when not shielded by organic matter aggregates. This might have been facilitated by a higher seawater barite saturation state during the Paleogene. However, Sr/Ba measurements suggest that barite undersaturation during the Paleocene-Eocene Thermal Maximum was comparable to that of the modern ocean (Paytan et al., 2007). Alternatively, benthic foraminifera may have only been able to consume a subset of the organic matter aggregates that shielded pelagic barite from dissolution, or ecosystem pressures independent from organic matter supply may have influenced benthic foraminifera populations. Palaeoceanographic studies from different locations and time periods generally show agreement between pelagic barite accumulation and benthic foraminifera (e.g., Gorbarenko et al., 2007; Moore Jr et al., 2014; Reolid and Martínez-Ruiz, 2012), so additional work is needed to determine how barite sediment records shed light on transfer efficiency and other vital aspects of the marine carbon cycle.

Conclusions

Here, we conducted laboratory experiments to assess the dissolution rate of synthetic barium sulfate in seawater under different conditions. We found that pH, salinity, and temperature did not significantly affect the observed rate of barium sulfate dissolution. Our findings suggest that pelagic barite dissolution in undersaturated seawater is far too rapid to allow for free barite crystals to survive transit through the water column. In contrast, barium sulfate crystals encased within organic matter aggregates showed little evidence of dissolution over time. This suggests that organic matter aggregates are critical to shielding pelagic barite crystals from dissolution. Therefore, the sediment pelagic barite proxy likely tracks the flux of organic matter aggregates to the seafloor. These findings call attention to the need for additional field-based studies to determine which water column processes are captured by sediment barite abundance. This has potentially important implications for the interpretation of sediment pelagic barite records to gain new insights into the marine carbon cycle.

Acknowledgements

T.L. was partially supported by a U.S. Department of Defense National Defense Science and Engineering Graduate Student Fellowship and a Ruth Newmark Scholarship from the UCSD Friends of the International Center. M. G. was supported by the Triton Research and Experiential Learning Scholars program. The authors thank Benjamin Gruber, Cecilia de la Prada, and Dr. Erica Ferrer and for their valuable assistance.

Chapter 3, in full, is a reprint of the material as it appears in “Water column barium sulfate dissolution and shielding by organic matter aggregates: Implications for the pelagic barite proxy,” published in Chemical Geology in 2023. T. Light, M. Garcia, J. C. Prairie, F. Martínez-

Ruiz, and R. Norris. The dissertation author was the primary investigator and author of this paper.

References

Alldredge, A.L., Jackson, G.A. 1995. Preface: aggregation in marine system. Deep Sea Res. Part II: Top. Stud. Oceanogr. 42, 1–7.

Alldredge, A.L., Silver, M. W. 1988. Characteristics, dynamics and significance of marine snow. Prog. Oceanogr. 20, 41–82.

Arganda-Carreras, I., Kaynig, V., Rueden, C., Eliceiri, K. W., Schindelin, J., Cardona, A., Sebastian Seung, H. 2017. Trainable Weka segmentation: a machine learning tool for microscopy pixel classification. Bioinformatics 33, 2424–2426.

Averyt, K. B., Paytan, A. 2003. Empirical partition coefficients for Sr and Ca in marine barite: implications for reconstructing seawater Sr and Ca concentrations. Geochem. Geophys. Geosyst. 4, 1043.

Bareille, G., Labracherie, M., Labeyrie, L., Pichon, J. J., Turon, J. L. 1991. Biogenic silica accumulation rate during the Holocene in the southeastern Indian Ocean. Mar. Chem. 35, 537–551.

Bates, S.L., Hendry, K.R., Pryer, H.V., Kinsley, C.W., Pyle, K.M., Woodward, E.M.S., Horner, T.J. 2017. Barium isotopes reveal role of ocean circulation on barium cycling in the Atlantic. Geochim. Cosmochim. Acta. 204, 286–299.

Becker, U., Biswas, S., Kendall, T., Risthaus, P., Putnis, C.V., Pina, C.M. 2005. Interactions between mineral surfaces and dissolved species: from monovalent ions to complex organic molecules. Am. J. Sci. 305, 791–825.

Bridgestock, L., Hsieh, Y.T., Porcelli, D., Homoky, W.B., Bryan, A., Henderson, G.M. 2018. Co ntrols on the barium isotope compositions of marine sediments. Earth Planet. Sci. Lett. 481, 101–110.

Bertram, M. A., Cowen, J. P. 1997. Morphological and compositional evidence for biotic precipitation of marine barite. J. Mar. Res. 55, 577–593.

Bethke, M.C., Farrell, B., Yeakel, S., 2022. GWB Essentials Guide. Aqueous Solutions, LLC.

Bridgestock, L., Hsieh, Y. T., Porcelli, D., Henderson, G. M., 2019. Increased export production during recovery from the Paleocene–Eocene thermal maximum constrained by sedimentary Ba isotopes. Earth Planet. Sci. Lett. 510, 53–63.

Briese, L., Arvidson, R. S., Luttge, A. 2017. The effect of crystal size variation on the rate of dissolution–A kinetic Monte Carlo study. Geochim. Cosmochim. Acta. 212, 167–175.

Brummer, G. J. A., Van Eijden, A. J. M. 1992. “Blue-ocean” paleoproductivity estimates from pelagic carbonate mass accumulation rates. Mar. Micropaleontol. 19, 99–117.

Bu, X., Liu, M., Ding, Y., Yang, Y., Huang, M., Sun, X., Fan, D., Yang, Z. 2023. The origin and preservation of suspended barites near the 90° E ridge in the northeastern Indian Ocean. J. Ocean Univ. China 22, 88–98.

Burton, J. D., Marshall, N. J., Phillips, A. J. 1968. Solubility of barium sulphate in sea water. Nature. 217, 834–835.

Calvert, S. E., Pedersen, T. F. 2007. Elemental proxies for palaeoclimatic and palaeoceanographic variability in marine sediments: interpretation and application. In: Hillaire-Marcel, C., De Vernal, A. (Eds.), Proxies in Late Cenozoic Paleoceanography. Elsevier, Amsterdam. 567–644.

Carter, S. C., Paytan, A., Griffith, E. M. 2020. Toward an improved understanding of the marine barium cycle and the application of marine barite as a paleoproductivity proxy. Minerals. 10, 421.

Cawley, G. F., Décima, M., Mast, A., Prairie, J.C. 2021. The effect of phytoplankton properties on the ingestion of marine snow by *Calanus pacificus*. J. Plankton Res. 43, 957–973.

Chow, T. J., Goldberg, E. D. 1960. On the marine geochemistry of barium. Geochim. Cosmochim. Acta. 20, 192–198.

Christy, A. G., Putnis, A. 1993. The kinetics of barite dissolution and precipitation in water and sodium chloride brines at 44–85 C. Geochim. Cosmochim. Acta. 57, 2161–2168.

Church, T.M., Wolgemuth, K. 1972. Marine barite saturation. Earth Planet. Sci. Lett. 15, 35–44.

Costa, K.M., McManus, J.F., Anderson, R.F., Ren, H., Sigman, D.M., Winckler, G., Fleisher, M. Q., Marcantonio, F., Ravelo, A. C. 2016. No iron fertilization in the equatorial Pacific Ocean during the last ice age. Nature. 529, 519–522.

Dehairs, F., Chesselet, R., Jedwab, J., 1980. Discrete suspended particles of barite and the barium cycle in the open ocean. Earth Planet. Sci. Lett. 49, 528–550.

Delany, J.M., Lundeen, S.R. 1991. The LLNL Thermochemical Data Base--Revised Data and File Format for the EQ3/6 Package No. UCID-21658 Lawrence Livermore National Lab (LLNL), Livermore.

DeVries, T. 2022. The ocean carbon cycle. Annu. Rev. Environ. Resour. 47, 317–341.

DeVries, T., Weber, T. 2017. The export and fate of organic matter in the ocean: new constraints from combining satellite and oceanographic tracer observations. Glob. Biogeochem. Cycles. 31, 535–555.

Diester-Haass, L., Faul, K. 2019. Paleoproductivity reconstructions for the Paleogene Southern Ocean: A direct comparison of geochemical and micropaleontological proxies. Paleoceanogr. Paleoclimatol. 34, 79–97.

Dove, P. M., Czank, C. A. 1995. Crystal chemical controls on the dissolution kinetics of the isostructural sulfates: celestite, anglesite, and barite. Geochim. Cosmochim. Acta. 59, 1907–1915.

Dunn, K., Daniel, E., Shuler, P. J., Chen, H. J., Tang, Y., Yen, T. F. 1999. Mechanisms of surface precipitation and dissolution of barite: a morphology approach. J. Colloid Interface Sci. 214, 427–437.

Dymond, J., Suess, E., Lyle, M. 1992. Barium in deep-sea sediment: a geochemical proxy for paleoproductivity. Paleoceanogr. 7, 163–181.

Eagle, M., Paytan, A., Arrigo, K. R., van Dijken, G., Murray, R. W. 2003. A comparison between excess barium and barite as indicators of carbon export. Paleoceanogr. 18.

Emerson, S., Hedges, J. 2008. Chemical Oceanography and the Marine Carbon Cycle. Cambridge University Press, Cambridge.

Esser, B.K., Volpe, A.M. 2002. At-sea high-resolution chemical mapping: extreme barium depletion in North Pacific surface water. Mar. Chem. 79, 67–79.

Fakhraee, M., Planavsky, N.J., Reinhard, C.T. 2020. The role of environmental factors in the long-term evolution of the marine biological pump. Nat. Geosci. 13, 812–816.

Falkner, K. K., Klinkhammer, G. P., Bowers, T. S., Todd, J. F., Lewis, B. L., Landing, W. M., Edmo, J. M. 1993. The behavior of barium in anoxic marine waters. Geochim. Cosmochim. Acta. 57, 537–554.

Goldschmidt, V. M., 1913. Atlas der Krystallformen. Carl Winters Universitätsbuchhandlung, Heidelberg.

Gonzalez-Muñoz, M. T., Martinez-Ruiz, F., Morcillo, F., Martin-Ramos, J. D., Paytan, A. 2012. Precipitation of barite by marine bacteria: a possible mechanism for marine barite formation. Geology. 40, 675–678.

Gorbarenko, S. A., Goldberg, E. L. V., Kashgarian, M., Velivetskaya, T. Y. A., Zakharkov, S. P., Pechnikov, V. S., Bosin, A. A. E., Psheneva, O. Y. E., Ivanova, E. D. 2007. Millennium scale environment changes of the Okhotsk Sea during last 80 kyr and their phase relationship with global climate changes. J. Oceanogr. 63, 609–623.

Griffith, E. M., Thomas, E., Lewis, A. R., Penman, D.E., Westerhold, T., Winguth, A.M. 2021. Bentho-pelagic decoupling: The marine biological carbon pump during Eocene hyperthermals. Paleoceanogr. Paleoclimatol. 36, e2020PA004053.

Hanor, J.S. 1969. Barite saturation in sea water. Geochim. Cosmochim. Acta. 33, 894–898.

Hayes, C.T., Costa, K.M., Anderson, R.F., Calvo, E., Chase, Z., Demina, L.L., Dutay, J.-C., German, C.R., Heimbürger-Boavida, L.E., Jaccard, S.L., Jacobel, A., Kohfeld, K.E., Kravchishina, M.D., Lippold, J., Mekik, F., Missiaen, L., Pavia, F.J., Paytan, A., Pedrosa-Pamies, R., Petrova, M.V., Rahman, S., Robinson, L.F., Roy-Barman, M., Sanchez-Vidal, A., Shiller, A., Tagliabue, A., Tessin, A.C., van Hulten, M., Zhang, J. 2021. Global ocean sediment composition and burial flux in the deep sea. Glob. Biogeochem. Cycles. 35, e2020GB006769.

Higgins, S. R., Jordan, G., Eggleston, C. M., Knauss, K. G. 1998. Dissolution kinetics of the barium sulfate (001) surface by hydrothermal atomic force microscopy. Langmuir. 14, 4967–4971.

Horner, T. J., Crockford, P. W. 2021. Barium Isotopes: Drivers, Dependencies, and Distributions Through Space and Time. Cambridge University Press.

Horner, T. J., Kinsley, C. W., Nielsen, S. G. 2015. Barium-isotopic fractionation in seawater mediated by barite cycling and oceanic circulation. Earth Planet. Sci. Lett. 430, 511–522.

Horner, T. J., Little, S. H., Conway, T. M., Farmer, J. R., Hertzberg, J. E., Janssen, D. J., Lough, A. J. M., McKay, J., Tessin, A., Galer, S. J. G., Jaccard, S. L., Lacan, F., Paytan, A., Wuttig, K., Bolton, C., Calvo, E., Cardinal, D., de Garidel-Thoron, T., Fietz, S., Hendry, K., Marcantonio, F., Rafter, P., Ren, H., Somes, C., Sutton, J., Torfstein, A., Winckler, G. 2021. Bioactive trace metals and their isotopes as paleoproductivity proxies: an assessment using GEOTRACES-era data. Glob. Biogeochem. Cycles. 35, e2020GB006814.

Hsieh, Y. T., Henderson, G. M. 2017. Barium stable isotopes in the global ocean: tracer of Ba inputs and utilization. Earth Planet. Sci. Lett. 473, 269–278.

Iversen, M. H., Ploug, H. 2010. Ballast minerals and the sinking carbon flux in the ocean: carbon-specific respiration rates and sinking velocity of marine snow aggregates. Biogeosciences. 7, 2613–2624.

Judat, B., Kind, M. 2004. Morphology and internal structure of barium sulfate—derivation of a new growth mechanism. J. Colloid Interface Sci. 269, 341–353.

Kamal, M.S., Hussein, I., Mahmoud, M., Sultan, A.S., Saad, M.A. 2018. Oilfield scale formation and chemical removal: a review. J. Pet. Sci. Eng. 171, 127–139.

Kügler, R.T., Doyle, S., Kind, M. 2015. Fundamental insights into barium sulfate precipitation by time-resolved in situ synchrotron radiation wide-angle X-ray scattering (WAXS). Chem. Eng. Sci. 133, 140–147.

Lam, P. J., Doney, S. C., Bishop, J. K. B. 2011. The dynamic ocean biological pump: Insights from a global compilation of particulate organic carbon, $CaCO_3$, and opal concentration profiles from the mesopelagic. Glob. Biogeochem. Cycles. 25, GB3009.

Laurenceau-Cornec, E.C., Le Moigne, F.A.C., Gallinari, M., Moriceau, B., Toullec, J., Iversen, M.H., Engel, A., De La Rocha, C.L. 2020. New guidelines for the application of Stokes' models to the sinking velocity of marine aggregates. Limnol. Oceanogr. 65, 1264–1285.

Light, T., Norris, R. 2021. Quantitative visual analysis of marine barite microcrystals: insights into precipitation and dissolution dynamics. Limnol. Oceanogr. 66, 3619–3629.

Lopes, C., Kucera, M., Mix, A.C. 2015. Climate change decouples oceanic primary and export productivity and organic carbon burial. Proc. Natl. Acad. Sci. 112, 332–335.

Loubere, P. 1991. Deep-sea benthic foraminiferal assemblage response to a surface ocean productivity gradient: a test. Paleocenography. 6, 193–204.

Lüttge, A. 2005. Etch pit coalescence, surface area, and overall mineral dissolution rates. Am. Mineral. 90, 1776–1783.

Ma, Z., Ravelo, A.C., Liu, Z., Zhou, L., Paytan, A. 2015. Export production fluctuations in the eastern equatorial Pacific during the Pliocene-Pleistocene: reconstruction using barite accumulation rates. Paleoceanography. 30, 1455–1469.

Marchisio, D.L., Barresi, A.A., Garbero, M. 2002. Nucleation, growth, and agglomeration in barium sulfate turbulent precipitation. AICHE J. 48, 2039–2050.

Martinez-Ruiz, F., Jroundi, F., Paytan, A., Guerra-Tschuschke, I., del Abad , M.M., González-Muñoz, M.T. 2018. Barium bioaccumulation by bacterial biofilms and implications for Ba cycling and use of Ba proxies. Nat. Commun. 9, 1619.

Martinez-Ruiz, F., Paytan, A., Gonzalex-Muñoz, M.T., Jroundi, F., Abad, M.D.M., Lam, P.J., Bishop, J.K.B., Horner, T.J., Morton, P.L., Kastner, M. 2019. Barite formation in the ocean: Origin of amorphous and crystalline precipitates. Chem. Geol. 511, 441–451.

Martinez-Ruiz, F., Paytan, A., Gonzalez-Muñoz, M.T., Jroundi, F., Abad, M.D.M., Lam, P.J., Horner, T.J., Kastner, M. 2020. Barite precipitation on suspended organic matter in the mesopelagic zone. Front. Earth Sci. 8, 567714.

McNown, J., Malaika, J. 1950. Effects of particle shape on settling velocity at low Reynolds numbers. Trans. Am. Geophys. Union. 31, 74–82.

Mete, Ö., Subhas, A., Kim, H., Dunlea, A., Whitmore, L., Shiller, A., Gilbert, M., Leavitt, W., Horner, T. 2023. Barium in seawater: dissolved distribution, relationship to silicon, and barite saturation state determined using machine learning. Earth Syst. Sci. Data Discuss. 1–42.

Middleton, J.T., Hong, W.L., Paytan, A., Auro, M.E., Griffith, E.M., Horner, T.J. 2023. Barium isotope fractionation in barite–fluid systems at chemical equilibrium. Chem. Geol. 121453.

Monnin, C., Cividini, D. 2006. The saturation state of the world's ocean with respect to (Ba, Sr) SO4 solid solutions. Geochim. Cosmoshim. Acta. 70, 3290–3298.

Monnin, C., Jeandel, C., Cattaldo, T., Dehairs, F. 1999. The marine barite saturation state of the world's oceans. Mar. Chem. 65, 253–261.

Moore, T.C., Jr., Wade, B.S., Westerhold, T., Erhardt, A.M., Coxall, H.K., Baldauf, J., Wagner, M. 2014. Equatorial Pacific productivity changes near the Eocene-Oligocene boundary. Paleoceanography. 29, 825–844.

Nancollas, G.H., Liu, S.T. 1975. Crystal growth and dissolution of barium sulfate. Soc. Pet. Eng. J. 15, 509–516.

Nayar, K. G., Sharqawy, M. H., Banchik, L. D., Lienhard, V. J. H. 2016. Thermophysical properties of seawater: a review and new correlations that include pressure dependence. Desalination. 390, 1–24.

Nowicki, M., DeVries, T., Siegel, D. A. 2022. Quantifying the carbon export and sequestration pathways of the ocean's biological carbon pump. Glob. Biogeochem. Cycles. 36, e2021GB007083.

Nürnberg, C.C., Bohrmann, G., Schlüter, M., Frank, M., 1997. Barium accumulation in the Atlantic sector of the Southern Ocean: results from 190,000-year records. Paleoceanography. 12, 594–603.

Ouyang, B., Akob, D. M., Dunlap, D., Renock, D. 2017. Microbially mediated barite dissolution in anoxic brines. Appl. Geochem. 76, 51–59.

Ouyang, B., Renock, D., Akob, D. M. 2019. Effects of organic ligands and background electrolytes on barite dissolution. Geochim. Cosmochim. Acta. 256, 6–19.

Paytan, A., Griffith, E. M., 2007. Marine barite: recorder of variations in ocean export productivity. Deep Sea Res. Part II: Top. Stud. Oceanogr. 54, 687–705.

Paytan, A., Kastner, M., 1996. Benthic Ba fluxes in the central Equatorial Pacific, implications for the oceanic Ba cycle. Earth Planet. Sci. Lett. 142, 439–450.

Paytan, A., Kastner, M., Chavez, F. P. 1996. Glacial to interglacial fluctuations in productivity in the equatorial pacific as indicated by marine barite. Science. 274, 1355–1357.

Paytan, A., Averyt, K., Faul, K., Gray, E., Thomas, E., 2007. Barite accumulation, ocean productivity, and Sr/Ba in barite across the Paleocene–Eocene thermal maximum. Geology. 35, 1139–1142.

Pedersen, T.F., Calvert, S.E. 1990. Anoxia vs. productivity: what controls the formation of organic-carbon-rich sediments and sedimentary rocks? AAPG Bull. 74, 454–466.

Ploug, H. 2001. Small-scale oxygen fluxes and remineralization in sinking aggregates. Limnol. Oceanogr. 46, 1624–1631.

Ploug, H., Hietanen, S., Kuparinen, J. 2002. Diffusion and advection within and around sinking, porous diatom aggregates. Limnol. Oceanogr. 47, 1129–1136.

Prairie, J. C., Montgomery, Q. W., Proctor, K. W., Ghiorso, K. S. 2019. Effects of phytoplankton growth phase on settling properties of marine aggregates. J. Mar. Sci. Eng. 7, 265.

R Core Team, 2020. R: A Language and Environment for Statistical Computing. R Foundation for Statistical Computing, Vienna, Austria.

Ragueneau, O., Tréguer, P., Leynaert, A., Anderson, R.F., Brzezinski, M.A., DeMaster, D.J., Dugdale, R.C., Dymond, J., Fischer, G., François, R., Heinze, C. 2000. A review of the Si cycle in the modern ocean: recent progress and missing gaps in the application of biogenic opal as a paleoproductivity proxy. Glob. Planet. Chang. 26, 317–365.

Rahman, S., Shiller, A.M., Anderson, R.F., Charette, M.A., Hayes, C.T., Gilbert, M., Grissom, K.R., Lam, P.J., Ohnemus, D.C., Pavia, F.J., Twining, B.S., Vivancos, S.M. 2022. Dissolved and particulate barium distributions along the US GEOTRACES North Atlantic and East Pacific Zonal Transects (GA03 and GP16): global implications for the marine barium cycle. Glob. Biogeochem. Cycles. 36, e2022GB007330.

Reolid, M., Martínez-Ruiz, F. 2012. Comparison of benthic foraminifera and geochemical proxies in shelf deposits from the Upper Jurassic of the Prebetic (southern Spain). J. Iber. Geol. 38, 449–465.

Robin, E., Rabouille, C., Martinez, G., Lefevre, I., Reyss, J.L., Van Beek, P., Jeandel, C. 2003. Direct barite determination using SEM/EDS-ACC system: implication for constraining barium carriers and barite preservation in marine sediments. Mar. Chem. 82, 289–306.

Rushdi, A.I., McManus, J., Collier, R.W. 2000. Marine barite and celestite saturation in seawater. Mar. Chem. 69, 19–31.

Sanders, R., Henson, S.A., Koski, M., De La Rocha, C.L., Painter, S.C., Poulton, A.J., Riley, J., Salihoglu, B., Visser, A., Yool, A., Bellerby, R., Martin, A.P. 2014. The biological carbon pump in the North Atlantic. Prog. Oceanogr. 129, 200–218.

Schenau, S.J., De Lange, G.J. 2001. Phosphorus regeneration vs. burial in sediments of the Arabian Sea. Mar. Chem. 75, 201–217.

Schindelin, J., Arganda-Carreras, I., Frise, E., Kaynig, V., Longair, M., Pietzsch, T., Preibisch, S., Rueden, C., Saalfeld, S., Schmid, B., Tinevez, J.-Y., White, D.J., Hartenstein, V., Eliceiri, K., Tomancak, P., Cardona, A. 2012. Fiji: an open-source platform for biological-image analysis. Nat. Methods. 9, 676–682.

Schindelin, J., Rueden, C.T., Hiner, M.C., Eliceiri, K.W. 2015. The ImageJ ecosystem: an open platform for biomedical image analysis. Mol. Reprod. Dev. 82, 518–529.

Schoepfer, S.D., Shen, J., Wei, H., Tyson, R.V., Ingall, E., Algeo, T.J. 2015. Total organic carbon, organic phosphorus, and biogenic barium fluxes as proxies for paleomarine productivity. Earth-Sci. Rev. Part II. 149, 23–52.

Serno, S., Winckler, G., Anderson, R.F., Hayes, C.T., Ren, H., Gersonde, R., Haug, G.H. 2014. Using the natural spatial pattern of marine productivity in the Subarctic North Pacific to evaluate paleoproductivity proxies. Paleoceanography. 29, 438–453.

Sharqawy, M.H., Lienhard, J.H., Zubair, S.M. 2010. Thermophysical properties of seawater: a review of existing correlations and data. Desalin. Water Treat. 16, 354–380.

Shen, W., Qiao, S., Sun, R., He, Z., Wu, B., Jin, L., Chen, L., Yin, Z., Ge, C., Shi, X., Sheng, J. 2023. Distribution pattern of planktonic and benthic foraminifera in surface sediments near the equatorial western Indian Ocean and its indications of paleo-environment and productivity. J. Asian Earth Sci. 250, 105635.

Simon, M., Grossart, H., Schweitzer, B., Ploug, H. 2002. Microbial ecology of organic aggregates in aquatic ecosystems. Aquat. Microb. Ecol. 28, 175–211.

Sun, X., Yang, Z., Fan, D., Li, Y. 2015. Crystals of suspended marine barite in the eastern equatorial Pacific: processes of dissolution and effects on crystal morphology. Chin. J. Oceanol. Limnol. 33, 194–203.

Torfstein, A., Winckler, G., Tripati, A. 2010. Productivity feedback did not terminate the Paleocene-Eocene thermal maximum (PETM). Clim. Past. 6, 265–272.

Torres-Crespo, N., Martínez-Ruiz, F., González-Muñoz, M.T., Bedmar, E.J., De Lange, G.J., Jroundi, F. 2015. Role of bacteria in marine barite precipitation: a case study using Mediterranean seawater. Sci. Total Environ. 512, 562–571.

Trindade Pedrosa, E., Kurganskaya, I., Fischer, C., Luttge, A. 2019. A statistical approach for analysis of dissolution rates including surface morphology. Minerals 9, 458.

Van Beek, P., Reyss, J. L., Bonte, P., Schmidt, S. 2003. Sr/Ba in barite: a proxy of barite preservation in marine sediments? Mar. Geol. 199, 205–220.

Van der Jagt, H., Friese, C., Stuut, J. B. W., Fischer, G., Iversen, M. H. 2018. The ballasting effect of Saharan dust deposition on aggregate dynamics and carbon export: aggregation, settling, and scavenging potential of marine snow. Limnol. Oceanogr. 63, 1386–1394.

Wickham, H. 2016. ggplot2: Elegant Graphics for Data Analysis. Springer-Verlag, New York.

Widanagamage, I. H., Schauble, E. A., Scher, H. D., Griffith, E. M. 2014. Stable strontium isotope fractionation in synthetic barite. Geochim. Cosmochim. Acta. 147, 58–75.

Winckler, G., Anderson, R.F., Jaccard, S.L., Marcantonio, F. 2016. Ocean dynamics, not dust, have controlled equatorial Pacific productivity over the past 500,000 years. Proc. Natl. Acad. Sci. 113, 6119–6124.

Xiao, C., Wang, Y., Tian, J. 2022. Formation of marine barite in the deep-sea environment: evidence from sinking particles in the challenger deep, Mariana Trench. Reg. Stud. Mar. Sci. 50, 102159.

Yao, W., Griffith, E., Paytan, A. 2020. Pelagic Barite: Tracer of Ocean Productivity and a Recorder of Isotopic Compositions of Seawater S, O, Sr, Ca and Ba. Cambridge University Press.

Zetsche, E.M., Larsson, A.I., Iversen, M.H., Ploug, H. 2020. Flow and diffusion around and within diatom aggregates: effects of aggregate composition and shape. Limnol. Oceanogr. 65, 1818–1833.

Zhen-Wu, B.Y., Dideriksen, K., Olsson, J., Raahauge, P.J., Stipp, S.L.S., Oelkers, E.H. 2016. Experimental determination of barite dissolution and precipitation rates as a function of temperature and aqueous fluid composition. Geochim. Cosmochim. Acta. 194, 193–210.

Ziervogel, K., Steen, A.D., Arnosti, C. 2010. Changes in the spectrum and rates of extracellular enzyme activities in seawater following aggregate formation. Biogeosciences. 7, 1007–1015.

CHAPTER 4: Marine barite dynamics across the sediment water interface and along an offshore gradient

T. Light and R. Norris

Abstract

The accumulation rate of pelagic barite in marine sediments is commonly used as a proxy for the marine carbon cycle, but many aspects of pelagic barite dynamics are poorly understood. Here, we conducted quantitative visual analyses to assess variability in pelagic barite across the sediment-water interface and along an offshore gradient off the coast of southern California. We analyzed 1,390 pelagic barite microcrystals from the upper 10 cm of marine sediment and 302 microcrystals from the overlying water column at 4 sites along an east-west transect across the highly productive California Current System. Barite microcrystals from the sediment were larger and displayed higher solidity than microcrystals in the water column. This suggests that the smallest barite microcrystals have been differentially lost between the water column and the sediment. A result of that dissolution of small barite microcrystals has preferentially concentrated larger crystals in bottom sediment. We infer that barite microcrystals that survive incorporation into the sediment record were protected by organic matter aggregates during their transit through the water column. We did not observe clear, systematic trends in barite microcrystal size or morphology with depth in the sediment or along the gradients in distance offshore or primary productivity sampled here. Our findings are consistent with the use of barite as a reliable carbon cycle proxy, but observations at the most onshore and most offshore sites raise questions about barite growth limitation and preservation within sediments, respectively. The findings presented here are preliminary, and we collected many more water column and sediment samples than we were able to fully analyze. We invite collaborators who are interested in acquiring these samples and continuing this investigation to contact the authors.

Introduction

The accumulation rate of pelagic barite in marine sediments is a useful proxy for reconstructing the marine carbon cycle across geologic time. Pelagic barite precipitates within organic matter aggregates as they sink down through the water column, so it has been used to gain insights into organic matter dynamics over many key periods of Earth's history (e.g., Carter et al., 2016; Erhardt et al., 2013; Kim et al., 2022; Lowery and Bralower, 2022). However, these interpretations rely on a number of largely unconfirmed assumptions regarding the formation and preservation of pelagic barite. Important questions remain regarding how pelagic barite dynamics may vary under different ecosystem conditions, and the preservation of barite within marine sediments over time is poorly constrained.

Our current understanding of the quantitative relationship between marine barite precipitation and carbon export is largely derived from sediment core top calibration studies that compare modern barite accumulation rates to primary productivity estimates (Eagle et al., 2003; Paytan, Kastner, and Chavez, 1996; Dymond, Suess, and Lyle, 1992). While necessary for the interpretation of sediment barite records, these studies offer little insight into how marine productivity and ecosystem structure influence pelagic barite dynamics in the water column. Some studies have observed increased water column barite precipitation and dissolved Ba uptake following increases in biological activity (Stecher and Kogut, 1999; Cardinal et al., 2005). More detailed sediment trap investigations have found that while export production is correlated with barite export, the ratio between sinking particulate organic carbon and marine barite varies with time and space (Dymond and Collier, 1996; Dehairs et al., 2000; Jeandel et al., 2000). This variability is poorly understood but may be driven by phytoplankton and zooplankton community composition, particle sinking rate, and bottom water chemistry (Paytan and Griffith,

2007). The lack of direct observations of water column pelagic barite under variable ecosystem conditions introduces uncertainty into the reliable application of sediment-based productivity calibrations.

Differential preservation of pelagic barite across the sediment-water interface is another potential complication for the interpretation of barite records. Barite dissolution increases dramatically in anoxic sediments that are depleted in sulfate, so the barite accumulation rate proxy is not well-suited for regions with suboxic or anoxic sediments (McManus et al., 1998; Torres et al., 1996; Dickens, 2001). Pelagic barite is thought to be well-preserved in oxic sediments because their porewaters are generally at or near saturation with respect to barite, but some pelagic barite dissolution does occur within oxic sediments (McManus et al., 1998; Carter et al. 2020). One investigation into barium cycling in the equatorial Pacific estimated that 30% of particulate barium flux to the deep ocean is preserved, with the majority of deep ocean barite dissolution occurring in the upper centimeters of sediment (Paytan and Kastner, 1996). Isotopic tracer data suggest that pelagic barite dissolution within sediments produces a flux of Ba to the deep-sea water column (Hsieh and Henderson, 2017), and benthic incubation chambers in the Southern California Borderland suggest Ba flux out of marine sediments (McManus et al., 1999). Factors such as sediment accumulation rate and primary productivity in the overlying water column may affect the rate of downcore pelagic barite dissolution, but, to our knowledge, their influence has not been directly investigated.

The quantitative visual analysis of pelagic barite microcrystals can provide new insights into barite dissolution because it offers more detailed information than bulk barite concentrations alone (e.g., Light and Norris 2021). In this investigation, we use quantitative visual analysis to assess how ecosystem variability and differential preservation within sediments may affect the

reliability of the sediment pelagic barite proxy. We present our preliminary findings on how pelagic barite size and morphology vary across the sediment-water interface and along an offshore primary productivity gradient, and we discuss potential next steps for this work.

Materials and Methods

Sample collection and preparation

Water column and sediment samples were collected during a cruise of the R/V Sally Ride from December 21 to December 27, 2023 off the coast of San Diego (Fig. 19). Sampling locations followed an offshore gradient and ranged from a continental margin site with high primary productivity to relatively oligotrophic deeper sites (Fig. 19, Table 6). The study transect spanned the southern portion of the California Current System, an eastern boundary current characterized by coastal upwelling and a high productivity (e.g., Checkley and Barth, 2009). Primary productivity across the transect was estimated via satellite-derived surface water chlorophyll data (Fig. 19; ACRI-ST GlobColour Team, 2020). Water and sediment samples from 4 sampling locations are discussed here, but additional sampling was also collected at 2 other locations (Supplementary Information 4.1).

Water sampling was conducted using Niskin bottles attached to a CTD rosette sampling system. Seawater was sampled via Niskin bottle spigot and sequentially filtered to collect suspended particulate matter. Seawater (2.9 L) was first filtered through 12 μm pore diameter polycarbonate filters to remove larger particles. Coarsely filtered seawater was then filtered through polycarbonate filters with a pore diameter of 0.22 μm to collect barite microcrystals and other small particles. Filters were rinsed with deionized water, dried, and stored in airtight sample bags until later analysis. A total of 55 water depths were sampled across the 6 study sites

(Supplementary Information 4.1), but only the deepest water sample from the 4 primary study sites was analyzed for barite microcrystal size, abundance, and morphology (Fig. 19, Table 6).

Sediment from all 6 study sites was collected via multi-corer. One multi-core per site was sectioned into 2 cm slices by depth and stored in airtight sample bags under refrigeration until later analysis. Three months later, subsamples from 0-2 cm, 4-6 cm, and 8-10 cm sediment slices from study sites A, B, C, and D were analyzed for barite microcrystal size, abundance, and morphology. Approximately 2 cm^3 of sediment was removed from each slice and dried for 72 hours in a 50°C oven. 15-20 mg dried sediment from each slice was thoroughly ground in an agate mortar. Ground sediment was suspended in ultrapure Milli-Q water (18.2 MΩ·cm) and filtered through a 0.2 μm pore size, 25 mm diameter nylon membrane filter enclosed in a reusable filter holder. Filters were then dried in a 50°C oven before SEM-EDS analysis.

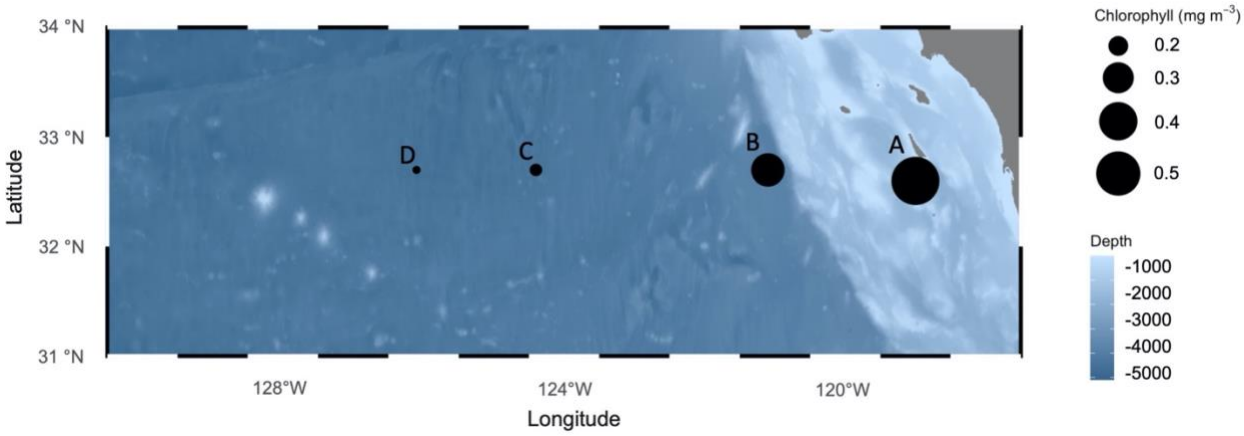

Figure 19. Locations of sampling sites A, B, C, and D. Bathymetry is from the global multiresolution topography (GMRT) synthesis (Ryan 2009). Chlorophyll concentrations represent gridded weighted averaging Level 3 Chl1 data for December 2022 from the GlobColour project, which provides a merged dataset from SeaWiFS, MODIS, and MERIS (ACRI-ST GlobColour Team, 2020).

Table 6. Sampling locations with the corresponding distance offshore, maximum water depth, water sampling depth analyzed, and satellite-based surface chlorophyll concentration estimate.

Site	Latitude	Longitude	Distance offshore (km)	Maximum water depth (m)	Sampling depth (m)	Chlorophyll (mg m^{-3})
A	32.58 N	118.52	120	1138	1125	0.58
B	32.70 N	120.63 W	317	3803	3794	0.33
C	32.70 N	123.88 W	621	4347	4344	0.17
D	32.70 N	125.60 W	782	4516	4505	0.16

Barite microcrystal analysis

Filters loaded with seawater particulate matter and sediment were analyzed for barite microcrystal size, abundance, and morphology via Scanning Electron Microscopy equipped with Energy-dispersive X-ray Spectroscopy (SEM-EDS). An approximately 1 cm^2 portion of each filter was mounted on an aluminum stub with carbon tape for analysis. Analyses were conducted on a Phenom Desktop SEM with an accelerating voltage of 15 kV, vacuum of 1 Pa, and working distance of 9-10 mm. For each sediment filter, 3 randomly selected fields with an area of 0.05 mm^2 were analyzed for each sediment filter. A backscatter electron (BSE) detector was used to systematically identify all potential barite microcrystals within the field by their high atomic number. Identification was confirmed by EDS, and all barite microcrystals were imaged. For each seawater filter, 70 barite crystals were randomly selected and imaged. All barite images were then quantitatively analyzed to determine barite microcrystal size and solidity using the

FIJI distribution of ImageJ (Schindelin et al. 2012; 2015), as described in Chapter 1. For sediment filters, barite microcrystal abundance for each field was calculated as follows:

$$A_b = \frac{n_b * A_f}{A_a * m}$$

where A_b is barite microcrystal abundance, n_b is number of barite particles observed in a given field, A_f is area of the filter, A_a is area of the field analyzed, and m is the mass of sediment loaded onto the filter. Solidity was calculated as a quantitative measure of morphology according to the equation:

$$S = \frac{A}{A_C}$$

where *S* is solidity, *A* is the area of the particle, and A_C is the area of the convex hull, or the smallest convex polygon that encloses the particle's outline.

Statistical analyses

One-way ANOVAs with a posteriori Tukey's honestly significant difference (HSD) tests were used to compare barite abundance, area per particle, and solidity between study sites and sediment depths (Table 7). For comparisons between sites, area per particle and solidity were log transformed. For comparisons between depths, area per particle and solidity were cube root transformed. One-way ANOVAs were used to compare barite area and solidity between microcrystals from the deepest water sampled at each site and surface sediment. For these ANOVAs, area was cube root transformed and solidity was log transformed. All statistical analysis was performed in R Version 3.6.3 (R Core Team, 2020), and the ggplot package was used for data visualization (Wickham, 2016).

Results

From the 4 sediment cores analyzed here, 1,390 barite microcrystals were imaged across 36 different fields. Barite microcrystals were predominantly ovoid or barrel-shaped, but other morphologies similar to those described in Chapter 1 were also observed. Barite microcrystal abundance was significantly lower at Site A than at the other three sites (Fig. 20, Table 7). Barite microcrystal area per particle varied between study sites, with Site A sediment containing the smallest barite microcrystals (Fig. 20, Table 7). No statistically significant differences were observed in microcrystal solidity between sites (Fig. 20, Table 7). Barite microcrystal abundance, area, and solidity did not significantly differ between sediment depths across all sampling sites, but there was variability with sediment depth within some sites (Fig. 20, Table 7).

An additional 302 barite microcrystals from the bottom water overlying sediment sampling locations were also imaged. Barite microcrystal morphology from water column samples was largely similar to that from sediment samples, but clusters of submicron barite crystals were more abundant in water column samples. Barite microcrystal area and solidity significantly differed between sediment and water column samples (Fig. 21, Table 7). Barite microcrystals from bottom water were smaller (0.55 ± 0.05 vs. 1.37 ± 0.06 μm^2) and displayed lower solidity (0.956 ± 0.002 vs. 0.966 ± 0.002) than barite from surface sediments (Fig. 21). The size distribution of microcrystals from the water column was skewed toward smaller particles than in the sediment, and microcrystals displaying lower solidity were more abundant in the water samples (Fig. 21).

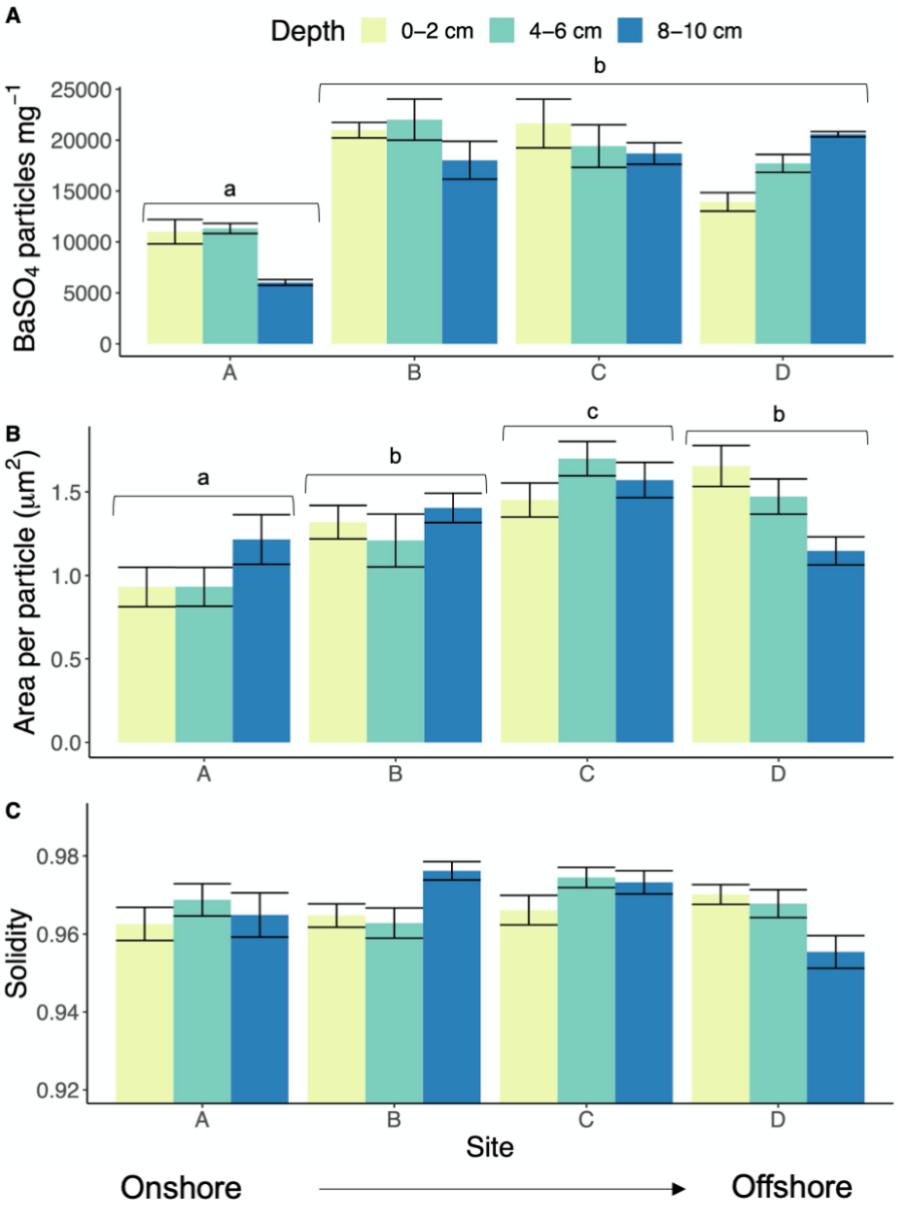

Figure 20. Average barite microcrystal A) abundance, B) area per particle, and C) solidity for each sediment depth slice across 4 sampling locations. Error bars display standard error. Lower case letters indicate statistically significant ($p < 0.05$) differences between sites as determined by post hoc Tukey's honestly significant difference (HSD) tests.

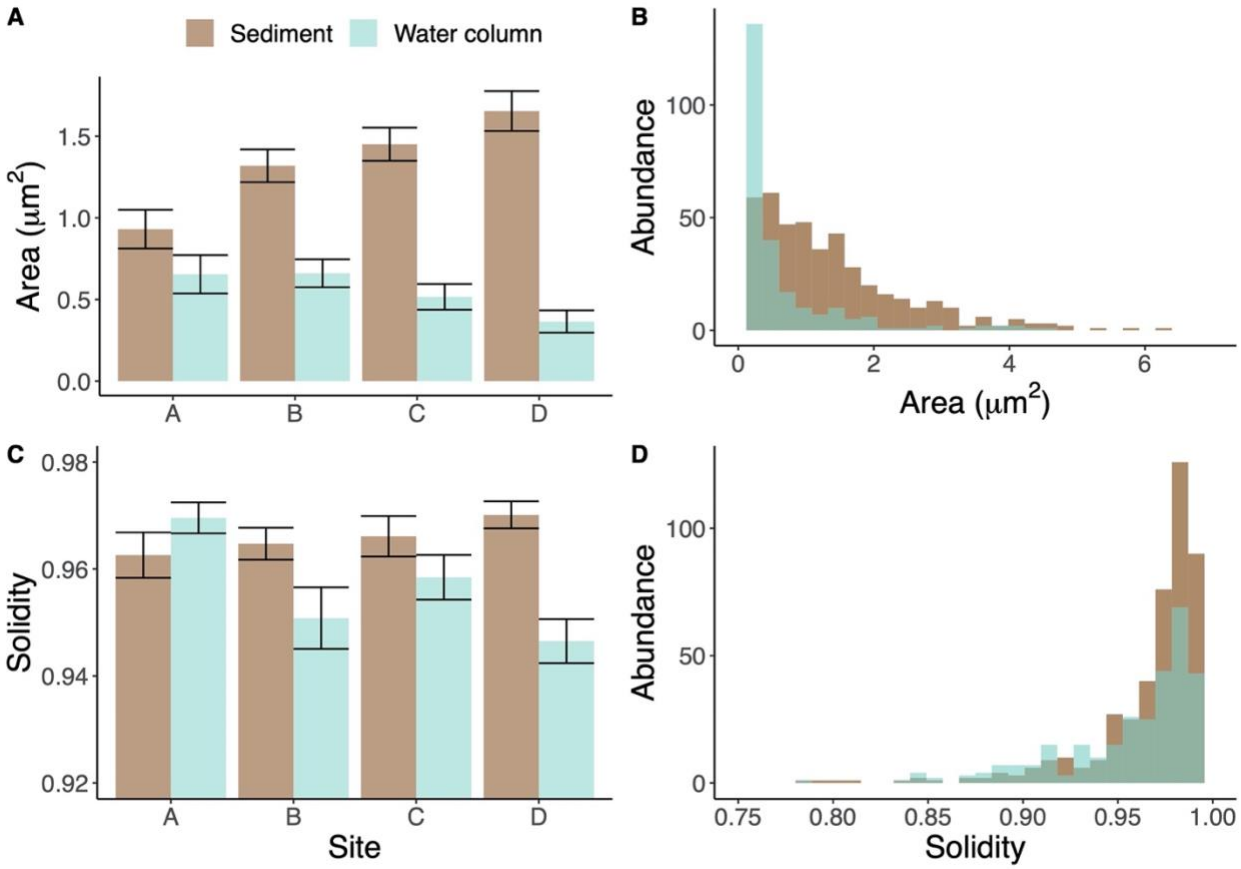

Figure 21. Average barite A) area per particle and C) solidity for microcrystals collected from the upper 2 cm of sediment and from bottom water at each of the 4 study sites. Error bars display standard error. Frequency distribution of B) area per particle and D) solidity across all 4 study sites. B) omits 2 outliers with areas ranging from 7-10 μm^2 and D) omits 3 outliers with solidity ranging from 0.65-0.75. Sediment microcrystals were larger and displayed higher solidity than microcrystals from the water column (Table 7).

Table 7. ANOVA statistics for comparisons in barite microcrystal abundance, area per particle, and solidity between locations (Sampling Sites A-D), sediment depths (0-2 cm, 4-6 cm, or 8-10 cm), and barite source (water column or sediment core top). Comparisons yielding statistically significant differences are bolded.

Parameter	**df**	**F**	**p**
Comparisons between sites			
Abundance	**3, 32**	**24.9**	**< 0.001**
Area per particle	**3, 1386**	**25.7**	**< 0.001**
Solidity	3, 1386	2.3	0.07
Comparisons between sediment depths			
Abundance	2, 33	0.3	0.7
Area per particle	2, 1387	0.6	0.7
Solidity	2, 1387	0.3	0.8
Comparisons between sediment and water column			
Area per particle	**1, 745**	**212.2**	**< 0.001**
Solidity	**1, 745**	**11.0**	**0.001**

Discussion

Differences in barite microcrystal size and solidity across the sediment water interface

To our knowledge, this investigation presents the first quantitative morphological comparison of collocated pelagic barite from marine sediments and the overlying water column. Very small crystals were more abundant in overlying water than in the upper 2 cm of the sediment (Fig. 21), which suggests that small crystals dissolved preferentially at the sediment-water interface. These very small particles may be sub crystalline or display other structural defects that make them more vulnerable to dissolution. The impact of this preferential dissolution

on pelagic barite accumulation rate and trace element and isotopic composition in the sediment record over time warrants further investigation.

The larger size and higher solidity of sediment barite (Fig. 21, Table 7) is somewhat surprising, since it suggests that water column barite has undergone more dissolution than that in sediments. Most pelagic barite formation occurs in the upper 1000 m of the water column (Carter et al., 2020), so we would expect barite in marine sediments to have spent more time exposed to seawater undersaturated with respect to barite. We hypothesize that, in addition to the preferential dissolution of small crystals, the higher size and solidity of sediment barite may be due to the shielding of pelagic barite by organic matter aggregates in the water column. Barite microcrystals that have survived transit through the water column and incorporation into marine sediments are likely protected from dissolution by organic matter aggregates (Light et al. 2023a). Meanwhile, barite crystals from the deep water overlying our study sites may have been recently released by organic matter aggregates that have been degraded or fragmented. We likely collected these water column crystals as they were dissolving in the water column, so they display more signs of dissolution than the sediment crystals which were largely shielded from the water column before arrival at the sediment-water interface. Thus, the contrast between barite microcrystals from the water column and sediment lends further support to the organic matter shielding hypothesis presented in Light et al. (2023a).

These findings highlight how barite from marine sediments differs from that in the water column and may help explain isotopic differences between pelagic barite and diagenetic barite (e.g., Paytan et al. 2002). While all pelagic barite in marine sediments was initially formed in the water column, sediment pelagic barite is not necessarily a representative sample of pelagic barite

found in the water column. More work is needed to determine how these differences influence the interpretation of barite proxy records.

Variability in barite properties along the offshore gradient

We did not observe clear, systematic trends in barite microcrystal area or solidity across the onshore to offshore or higher primary productivity to lower primary productivity gradient covered by our study sites (Fig. 20, Table 7). The lack of apparent systematic differences between these different marine ecosystems suggests that barite dynamics are broadly similar apart from the linear dependence of barite accumulation on carbon export. This supports pelagic barite in marine sediments as a reliable, ecosystem-wide carbon cycle proxy. That being said, this investigation only analyzed sediment from 4 study sites, and we did observe differences in average barite microcrystal size between locations.

Barite microcrystals were smallest at Site A, which was the shallowest, most productive, and most inshore site. The smaller size of microcrystals at this site may be due to lower Ba availability due to more widespread barite precipitation in accordance with the more intense organic matter remineralization. Direct observations of dissolved barium availability in our study region are not available, but coastal dissolved barium depletion is consistent with recent modeling work by Mete et al. (2023). This warrants further investigation because limitation of pelagic barite growth by Ba depletion in upwelling regions may be a source of non-linearity in the relationship between carbon export and barite accumulation. However, we did not test for sulfate reduction in the sediment cores we sampled, so barite crystals at Site A may be smaller because they were subjected to enhanced dissolution within the organic-matter-rich sediment column. Lastly, the shallower maximum water depth at this site may have contributed to the smaller microcrystal size, as barite microcrystals may have had more time to grow while sinking

down through the water column. However, Light et. al. (2023b) found that the formation of pelagic barite crystals likely occurs over the course of minutes, so water depth is unlikely to play a major role in determining microcrystal size.

Meanwhile, average area per barite crystal was highest at Site C, which has only slightly higher primary productivity than the oligotrophic Site D (Fig. 19). It may be that barite preservation is greatest at intermediate levels of primary productivity due to competing forces from high grazing pressure on organic matter aggregates in more productive areas and increased exposure to the undersaturated water column at the sediment water interface in less productive, slower sediment accumulation areas. Comparison of barite microcrystals from a greater number of study sites is necessary to resolve these differences.

We did not observe statistically significant differences in barite microcrystal abundance, area, or solidity with depth in the sediment core across all sites (Fig. 20, Table 7). This consistency suggests that barite dissolution within these sediments is limited, which further supports the reliability of the sediment barite proxy. Depth gradients may also be obscured by bioturbation, which often affects the upper 5-10 centimeters of marine sediments (Teal et al. 2008). However, we did observe some variability between depths at certain sites, particularly at Site D. There, barite microcrystal area per particle and solidity decreased with sediment depth (Fig. 20). This suggests that barite microcrystals gradually dissolved within the sediment over time. This dissolution may be most pronounced under low sediment accumulation rates, so it may not be well-captured by the sampling scheme used here. Additional assessment of barite microcrystal size and morphology with sediment depth in oligotrophic areas would be helpful in further constraining sediment barite preservation.

We also observed differences in barite abundance between study sites (Fig. 20), but barite abundance data alone is limited in its ability to provide insights into pelagic barite dynamics. Barite abundance values must be paired with sediment accumulation rate data to determine the rate of barite accumulation in marine sediments, which is the primary barite metric expected to correlate with primary productivity. The low barite abundance at Site A, the site closest to the coast, is likely due to the relative dilution of barite by a greater contribution of terrigenous input. If we were able to determine sediment accumulation rates for each site, we would expect sites A and B to have the highest rates of pelagic barite accumulation due to their higher primary productivity. We provide barite abundance data here in order to contextualize our other findings and facilitate the later determination of barite accumulation rates once sediment accumulation rates are available for these sites.

Conclusions and Next Steps

In this preliminary investigation, we present the first quantitative comparison of pelagic barite crystal size and morphology between marine sediments and the overlying water column. We found that barite microcrystals in marine sediments are significantly larger and more solid than those in the water column, which suggests that sediment barite is not a representative sample of the pelagic barite that forms in the water column. We also compared barite size and morphology with depth in the sediment column and across 4 sites with a large gradient in primary productivity. We did not observe clear, systematic trends in barite properties with sediment depth or productivity, which is generally consistent with the use of sediment pelagic barite as a reliable carbon cycle proxy. However, our data raise questions regarding barite crystal growth limitation and preservation at the sediment water interface that warrant further study.

This investigation invites a number of next steps that are necessary to take full advantage of the samples and data collected here. This future work includes analyzing barite microcrystal size, morphology, and abundance on the 51 water filters sampled but not analyzed here, analyzing pelagic barite in the sediments of the 2 remaining study sites, and establishing sediment accumulation rates at each site in order to compare barite accumulation rates across the offshore productivity gradient. Please contact the author if you are interested in collaborating on this work.

Acknowledgements

Sample collection was funded by the UC Ship Funds Program. Many thanks to Natalia Erazo and the entire science party and crew of Cruise SR 2215 on the RV Sally Ride for their invaluable assistance.

Chapter 4 contains unpublished material and is coauthored with R. Norris. The dissertation author was the primary investigator and author of this paper.

References

ACRI-ST GlobColour Team, 2020. *GlobColour Product User Guide*; Ref GC-UM-ACR-PUG-01; ACRI-ST GlobColour Team: Valborne, France.

Cardinal, D., Savoye, N., Trull, T. W., André, L., Kopczynska, E. E., Dehairs, F. 2005. Variations of Carbon Remineralisation in the Southern Ocean Illustrated by the Baxs Proxy. Deep Sea Res. Part I: Oceanogr. Res. Papers. 52, 355–70.

Carter, S. C., Griffith, E. M., Penman, D. E. 2016. Peak intervals of equatorial Pacific export production during the middle Miocene climate transition. Geology. 44, 923-926.

Carter, S. C., Paytan, A., Griffith, E. M. 2020. Toward an Improved Understanding of the Marine Barium Cycle and the Application of Marine Barite as a Paleoproductivity Proxy. Minerals. 10, 421.

Checkley Jr, D. M., Barth, J. A. 2009. Patterns and processes in the California Current System. Prog. Oceanogr. 83, 49-64.

Dehairs, F., Fagel, N., Antia, A. N., Peinert, R., Elskens, M., Goeyens, L. 2000. Export Production in the Bay of Biscay as Estimated from Barium – Barite in Settling Material: A Comparison with New Production. Deep Sea Res. Part I: Oceanogr. Res. Papers. 47, 583–601.

Dickens, G. R. 2001. Sulfate Profiles and Barium Fronts in Sediment on the Blake Ridge: Present and Past Methane Fluxes through a Large Gas Hydrate Reservoir. Geochim. Cosmochim. Acta. 65, 529–43.

Dymond, J., Collier, R. 1996. Particulate Barium Fluxes and Their Relationships to Biological Productivity. Deep Sea Res. Part I: Oceanogr. Res. Papers. 43, 1283–1308.

Eagle, M., Paytan, A., Arrigo, K. R., van Dijken, G., Murray, R. W. 2003. A Comparison between Excess Barium and Barite as Indicators of Carbon Export. Paleoceanography. 18.

Erhardt, A. M., Pälike, H., Paytan, A. 2013. High-resolution record of export production in the eastern equatorial Pacific across the Eocene-Oligocene transition and relationships to global climatic records. Paleoceanography. 28, 130-142.

Hsieh, Y., Henderson, G. 2017. Barium stable isotopes in the global ocean: tracer of Ba inputs and utilization. Earth Planet. Sci. Lett. 473, 269–78.

Jeandel, C., Tachikawa, K., Bory, A., Dehairs, F. 2000. Biogenic Barium in Suspended and Trapped Material as a Tracer of Export Production in the Tropical NE Atlantic (EUMELI Sites). Mar. Chem. 71, 125–42.

Kim, J. E., Westerhold, T., Alegret, L., Drury, A. J., Röhl, U., Griffith, E. M. 2022. Precessional pacing of tropical ocean carbon export during the Late Cretaceous. Clim. Past. 18, 2631-2641.

Light, T., Garcia, M., Prairie, J.C., Martínez-Ruiz, F. and Norris, R. 2023a. Water column barium sulfate dissolution and shielding by organic matter aggregates: Implications for the pelagic barite proxy. Chem. Geo. 636, 121637.

Light, T., Martínez-Ruiz, F., Norris, R. 2023b. Marine barite morphology as an indicator of biogeochemical conditions within organic matter aggregates. Geochim. Cosmochim. Acta. 358, 38-48.

Lowery, C. M., Bralower, T. J. 2022. Elevated Post K-Pg Export Productivity in the Gulf of Mexico and Caribbean. Paleoceanogr. Paleoclim. 37, e2021PA004400.

McManus, J., Berelson, W. M., Hammond, D. E. and Klinkhammer, G. P., 1999. Barium cycling in the North Pacific: Implications for the utility of Ba as a paleoproductivity and paleoalkalinity proxy. Paleoceanogr. 14, 53-61.

McManus, J., Berelson, W. M., Klinkhammer, G. P., Johnson, K. S., Coale, K. H., Anderson, Kumar, N., Burdige, D.J., Hammond, D.E., Brumsack, H.J., McCorkle, D.C. 1998. Geochemistry of Barium in Marine Sediments: Implications for Its Use as a Paleoproxy. Geochim. Cosmochim. Acta. 62, 3453–73.

Mete, Ö., Subhas, A., Kim, H., Dunlea, A., Whitmore, L., Shiller, A., Gilbert, M., Leavitt, W., Horner, T., 2023. Barium in seawater: dissolved distribution, relationship to silicon, and barite saturation state determined using machine learning. Earth Syst. Sci. Data Discuss. 15, 4023-4045.

Paytan, A., Mearon, S., Cobb, K., Kastner, M. 2002. Origin of marine barite deposits: Sr and S isotope characterization. Geology. 30, 747–750.

Paytan, A., Griffith, E. M. 2007. Marine Barite: Recorder of Variations in Ocean Export Productivity. Deep Sea Res. Part II Top. Stud. Oceanogr. The Role of Marine Organic Carbon and Calcite Fluxes in Driving Global Climate Change, Past and Future. 54, 687–705.

Paytan, A., Kastner, M. 1996. Benthic Ba Fluxes in the Central Equatorial Pacific, Implications for the Oceanic Ba Cycle. Earth Planet. Sci. Lett. 142, 439–50.

Paytan, A., Kastner, M., Chavez, F. P. 1996. Glacial to Interglacial Fluctuations in Productivity in the Equatorial Pacific as Indicated by Marine Barite. Science. 274, 1355–57.

R Core Team. 2020. R: A Language and Environment for Statistical Computing. R Foundation for Statistical Computing, Vienna, Austria.

Schindelin, J., C. Rueden, M. Hiner, and K. Eliceiri. 2015. The ImageJ ecosystem: an open platform for biomedical image analysis. Mol. Reprod. Dev. 82 (7–8): 518–29.

Schindelin, J., Arganda-Carreras, I., Frise, E., Kaynig, V., Longair, M., Pietzsch, T., Preibisch, S. Rueden, C., Saalfeld, S., Schmid, B., Tinevez, J. Y. 2012. Fiji: An open-source platform for biological image analysis. Nat. Methods. 9, 676–682.

Stecher, H. A., Kogut, M. B. 1999. Rapid Barium Removal in the Delaware Estuary. Geochim. Cosmochim. Acta. 63, 1003–12.

Teal, L. R., Bulling, M. T., Parker, E. R. Solan, M. 2008. Global patterns of bioturbation intensity and mixed depth of marine soft sediments. Aquat. Biol. 2, 207-218.

Torres, M. E., Brumsack, H. J., Bohrmann, G., Emeis, K. C. 1996. Barite Fronts in Continental Margin Sediments: A New Look at Barium Remobilization in the Zone of Sulfate Reduction and Formation of Heavy Barites in Diagenetic Fronts. Chem. Geo. 127, 125–39.

Wickham, H. 2016. ggplot2: Elegant Graphics for Data Analysis. Springer-Verlag, New York.

CONCLUSIONS

This work has considerably advanced the utility of the pelagic barite proxy by 1) providing new lines of evidence to support previously hypothesized aspects of pelagic barite formation and dissolution, 2) investigating which aspects of the marine carbon cycle the pelagic barite proxy records, and 3) highlighting potential obstacles that must be considered when interpreting barite sediment records. These findings increase our confidence in barite-based reconstructions and clarify how fluctuations in the barite sediment record should be interpreted. Thus, this work has improved pelagic barite as tool for studying the relationship between life in the ocean and global climate in the past, present, and future. Key findings of each dissertation chapter are as follows:

Chapter 1

- The most in-depth quantitative visual analysis of pelagic microcrystals to date provides a novel line of evidence for authigenic barite precipitation in association with organic matter aggregates and suggests that aggregates help protect barite from dissolution
- There is a rapid loss of barite microcrystals below ~500 m water depth, suggesting the dissolution of 60% ± 20% of particles formed shallower in the water column
- Additional work is needed to constrain spatial heterogeneity in pelagic barite precipitation and the factors that influence barite microcrystal morphology and cluster formation

Chapter 2

- Characteristic marine barite morphologies were produced in the laboratory under a narrow range of experimental conditions, which provide new insight into microenvironments within marine organic matter aggregates

- These findings are consistent with the hypothesized role of phospholipids in marine barite precipitation and suggest that pelagic barite precipitation is very rapid (< 10 minutes)

Chapter 3

- Salinity, pH, and temperature did not significantly affect the observed rate of barium sulfate dissolution in laboratory experiments
- Laboratory experiments suggest that pelagic barite dissolution in undersaturated seawater is far too rapid to allow free crystals to survive transit through the water column, but organic matter aggregates shield crystals from dissolution
- The sediment pelagic barite proxy likely tracks the flux of organic matter aggregates to the seafloor rather than export production higher in the water column

Chapter 4

- Barite microcrystals from the sediment were larger and displayed higher solidity than microcrystals in the water column, suggesting differential dissolution of very small crystals and shielding by organic matter aggregates
- While we observed interesting trends at certain study sites, our findings generally increase our confidence in the sediment barite proxy because we did not observe clear, systematic differences in barite with depth in the sediment, productivity in the overlying water column, or distance offshore

SUPPLEMENTARY INFORMATION

Supplementary Information for CHAPTER 1

Supplementary Information 1.1.

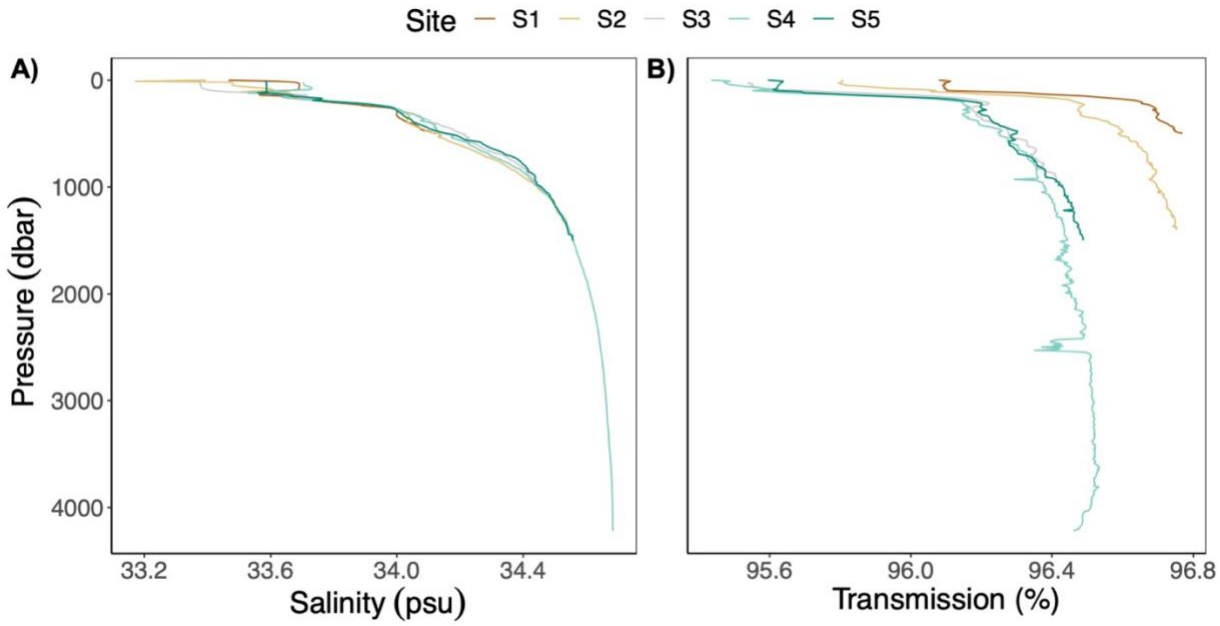

Figure 22. A) Salinity and B) transmission profiles acquired during CTD down casts at study sites S1-S5. Profiles were smoothed via boxcar averaging with a step size of 10 dbar.

Supplementary Information 1.2.

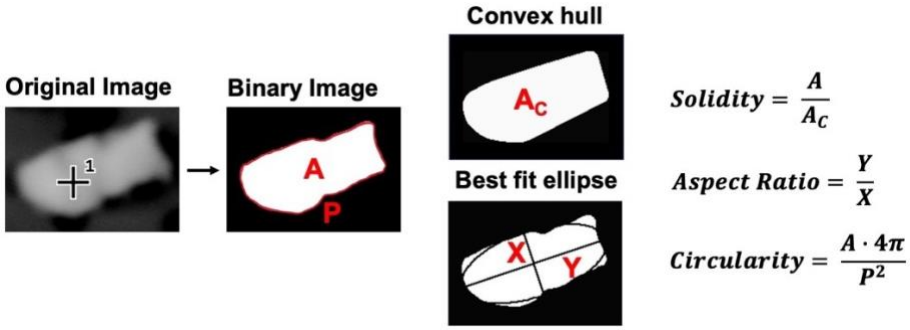

Figure 23. Schematic representing barite microcrystal image analysis. SEM images were binarized, smoothed, and quantitatively analyzed for area, solidity, aspect ratio, and circularity according to the equations displayed above.

Supplementary Information 1.3.

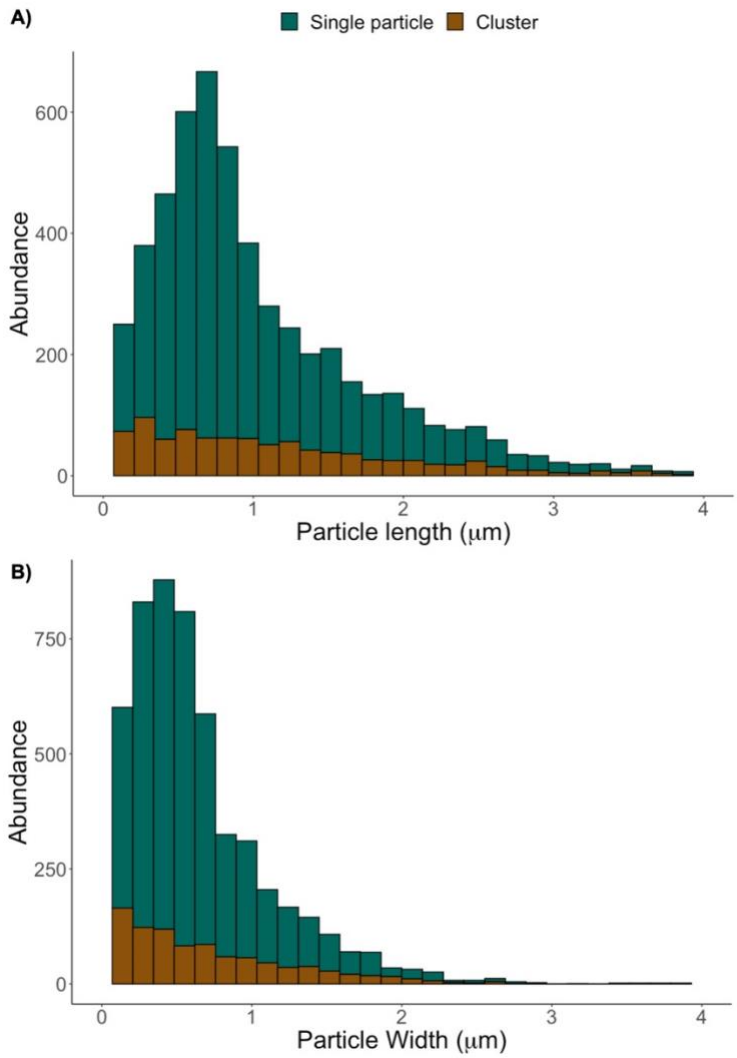

Figure 24. Histograms of barite microcrystal A) major axis and B) minor axis lengths for all single microcrystals and microcrystal clusters. A) omits 39 outliers with lengths ranging from 4-15 µm and B) omits 7 outliers with widths ranging from 4-6 µm.

Supplementary Information 1.4.

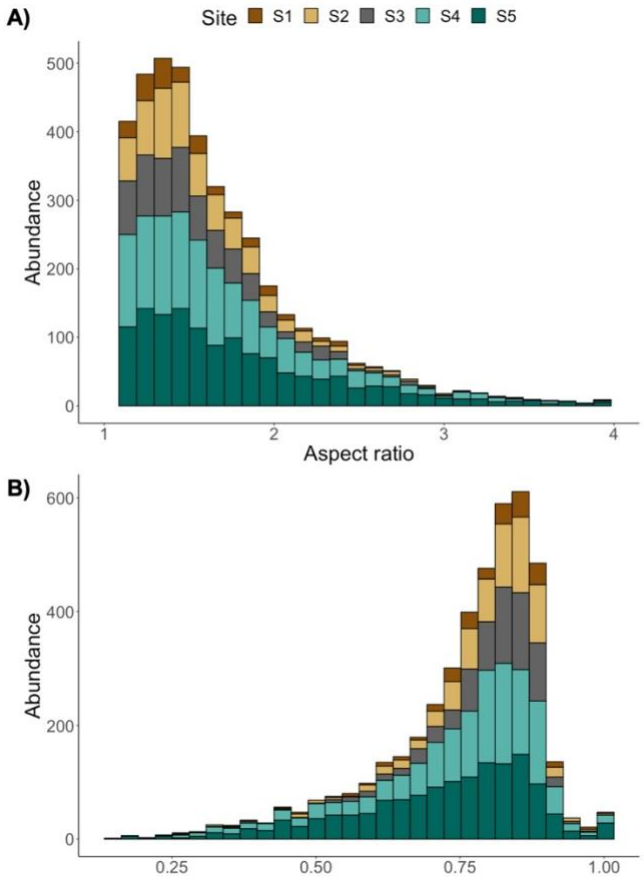

Figure 25. Histograms of barite microcrystal A) aspect ratio and B) circularity by sample site for all single particles, omitting barite clusters. A) omits 40 outliers with aspect ratios ranging from 4-7.25.

Supplementary Information for CHAPTER 2

Supplementary Information 2.1.

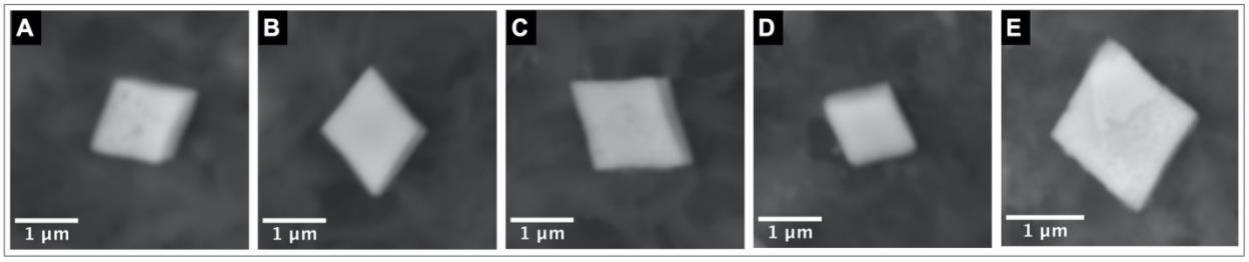

Figure 26. SEM images of representative barite crystal morphologies for crystals precipitated under Ba^{2+}:Sr^{2+} ratios of A) 10:1, B) 5:1, C) 1:1, D) 1:5, and E) 1:10. Barite crystal size and morphology were comparable between all 5 treatments. Apart from the quantity of $Sr(NO_3)_2$ added to the solution, experimental conditions were identical to those described for treatment SI-2.5 in the main text.

Supplementary Information 2.2.

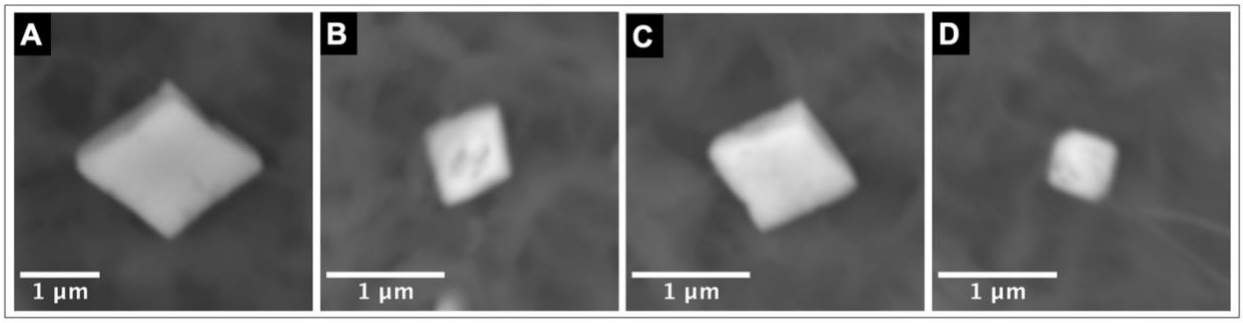

Figure 27. SEM images of barite crystal morphologies for crystals precipitated under Ba^{2+}:SO_4^{2-} ratios of A) 1:625, B) 1:2000, C) 1:7145, and D) 1:16670. Barite crystal size and morphology were comparable between treatments A-C, while crystals from treatment D were slightly smaller and displayed more rounded corners. Concentrations of Ba^{2+} and SO_4^{2-} were adjusted while maintaining a final solution barite saturation index of 2.5. Conditions largely resembled those described for treatment SI-2.5 in the main text, with the amount of NaCl adjusted to compensate for Na^+ added as Na_2SO_4.

Supplementary Information 2.3.

Table 8. Semi-quantitative EDX spectra spot analyses of phosphorous intensity relative to sulfur intensity for SI-2.5, Soy-100, and Soy-200 treatments. Phosphorous (P) intensity was measured at 2.01 keV, and sulfur (S) was measured at 2.31 keV.

Treatment	**Analysis**	**P Intensity (Counts)**	**S Intensity (Counts)**	**P/S Ratio (%)**
SI-2.5	Crystal 1 Spot 1	188.9	12.4	6.6
SI-2.5	Crystal 2 Spot 1	310.6	20.4	6.6
SI-2.5	Crystal 3 Spot 1	112.6	8.0	7.1
Average				**6.7 ± 0.3**
Soy-100	Crystal 1 Spot 1	227.2	15.3	6.7
Soy-100	Crystal 1 Spot 2	35.1	11.0	31.2
Soy-100	Crystal 1 Spot 3	53.0	9.8	18.5
Soy-100	Crystal 2 Spot 1	97.6	8.9	9.1
Average				**16 ± 11**
Soy-200	Crystal 1 Spot 1	147.5	10.2	6.9
Soy-200	Crystal 2 Spot 1	62.3	3.8	6.1
Average				**6.5 ± 0.6**

Supplementary Information 2.4.

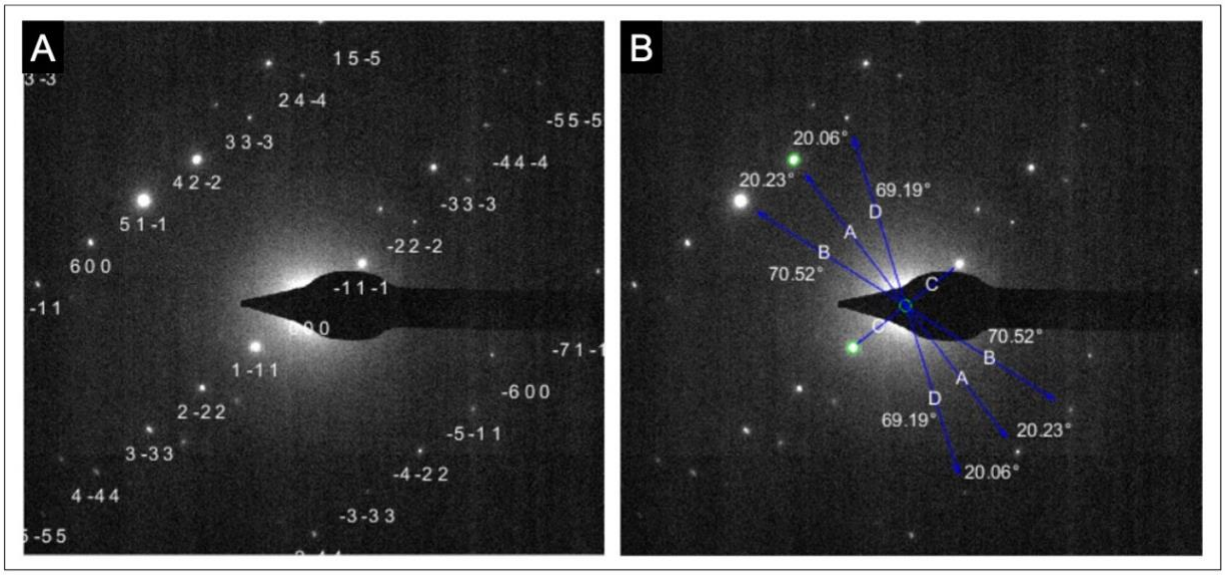

Figure 28. CrysTBox indexing analysis results for a SAED pattern of a barite crystal synthesized in the presence of EDTA. The annotated diffraction spot indices (A) and axes (B) are consistent with a crystal basal face of (0,1,1).

Supplementary Information for CHAPTER 3

Supplementary Information 3.1.

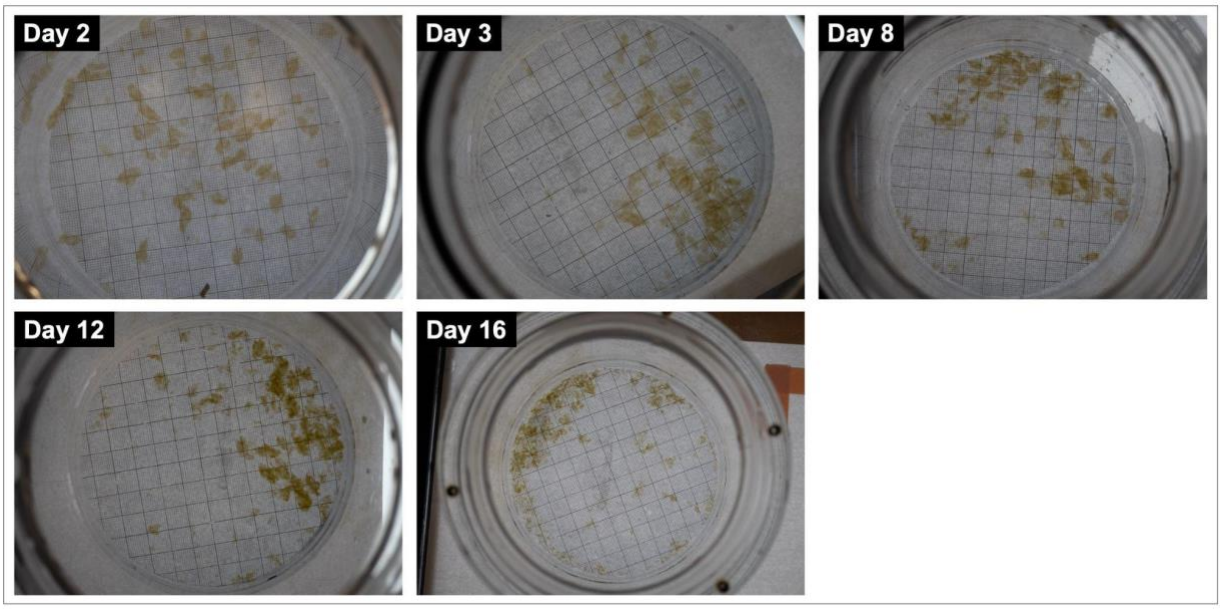

Figure 29. Organic matter aggregates imaged immediately before destructive sampling on incubation days 2, 3, 8, 12, and 16. Grid underneath the aggregates show 1 cm x 1cm larger squares and 1 mm x 1 mm smaller squares.

Supplementary Information 3.2.

Table 9. Estimated concentrations of seawater cations and anions for all treatments of the salinity experiment. Seawater for all other experimental treatments was assumed to have the same composition as the psu = 34 treatment.

Constituent	**psu = 27**	**psu = 30**	**psu = 34**	**psu = 38**	**psu = 46**
Ca^{2+} (mmol kg^{-1})	8.1	9.2	10.3	11.6	14.0
Mg^{2+} (mmol kg^{-1})	41.7	47.0	52.8	59.7	71.9
Na^{+} (mmol kg^{-1})	370.4	417.2	469.1	530.2	638.4
K^{+} (mmol kg^{-1})	8.1	9.1	10.2	11.5	13.9
SO_4^{2+} (mmol kg^{-1})	22.3	25.1	28.2	31.9	38.4
Cl^{-} (mmol kg^{-1})	431.0	485.5	545.9	617.0	742.9
Ba^{2+} (nmol kg^{-1})	30.0	33.8	38	42.9	51.7

Supplementary Information 3.3.

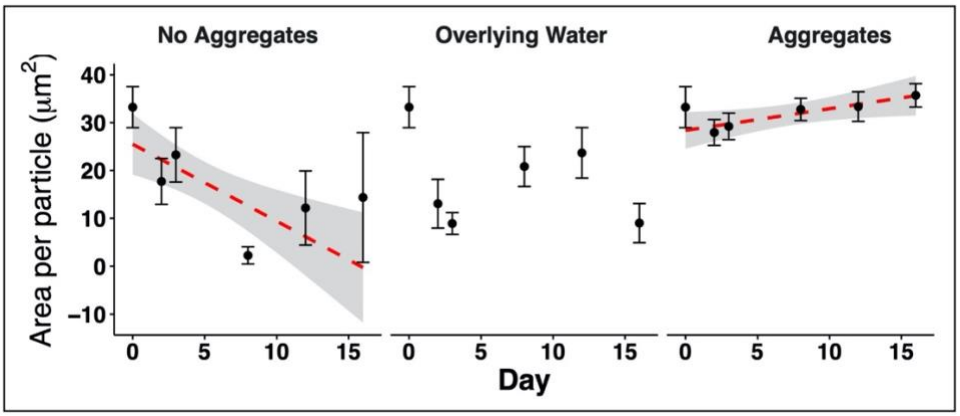

Figure 30. Barite crystal area per particle over time for No Aggregate, Overlying Water, and Aggregate treatments of the organic matter shielding experiment. Red dashed lines show fitted linear regression curves with standard error calculated by local regression in gray.

Supplementary Information 3.4.

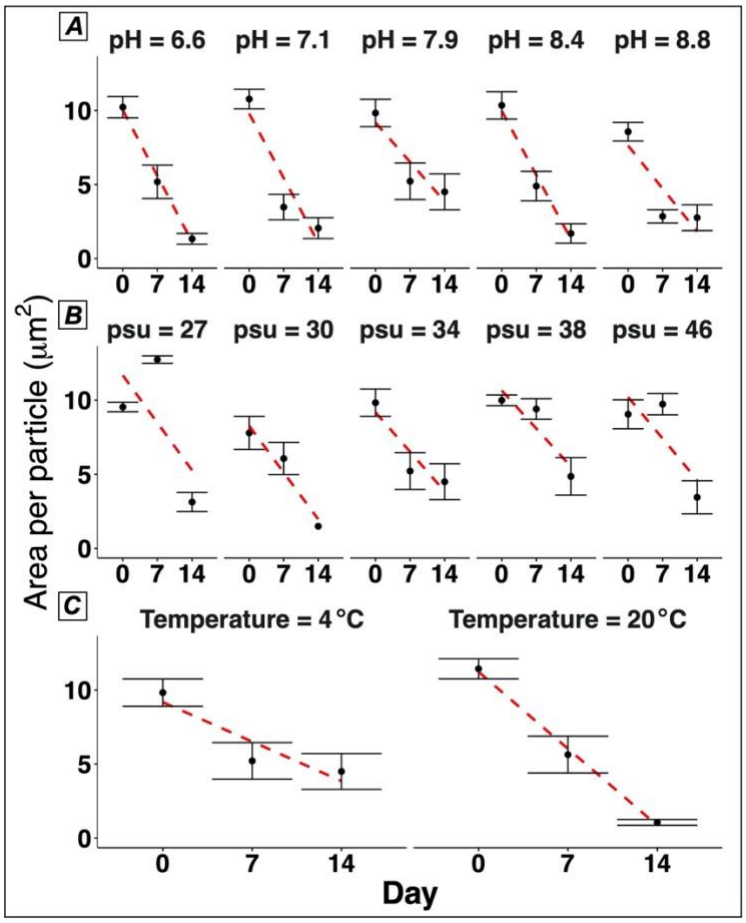

Figure 31. Barite crystal area per particle over time for A) pH, B) salinity, and C) temperature variation experiments. Red dashed lines show the fitted linear regression curve.

Supplementary Information 3.5.

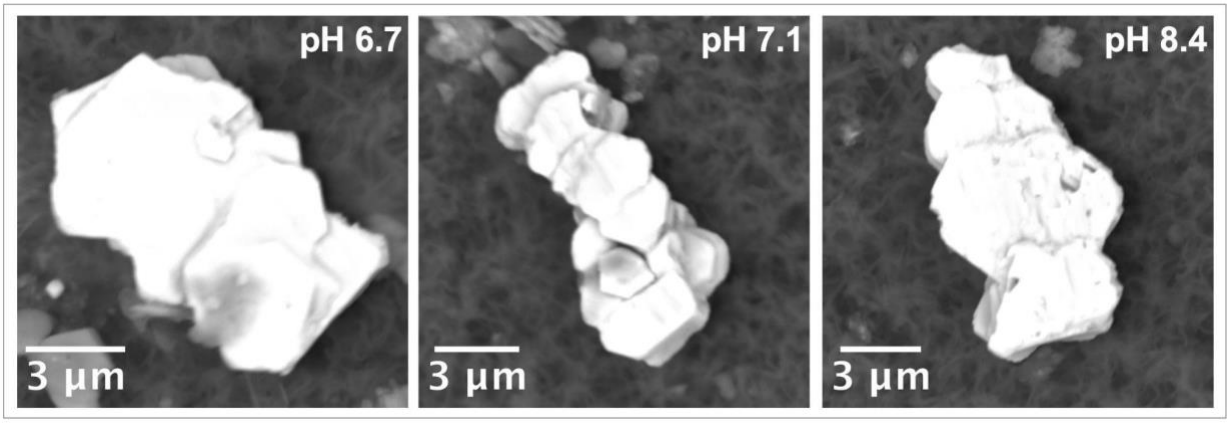

Figure 32. Representative barite crystals from day 21 of the pH, salinity, and temperature experiments.

Supplementary Information 3.6.

Table 10. Linear regression values for each treatment of the pH, salinity, and temperature experiments. Regressions were calculated with time in days as the independent variable and crystal mass as the dependent variable. Since rate of change in crystal mass did not significantly vary with treatment, these regression values were only calculated for visualization purposes.

Treatment	**F**	**df**	**P-value**	**r^2**	**m (pg)**	**b (pg)**
pH = 6.6	45.3	1, 43	< 0.001	0.51	-4.1 ± 0.6	61 ± 5
pH = 7.1	26.4	1, 43	< 0.001	0.38	-4.0 ± 0.8	61 ± 7
pH = 7.9	3.1	1, 47	0.086	0.06	-	-
pH = 8.4	29.0	1, 44	< 0.001	0.40	-3.6 ± 0.7	59 ± 6
pH = 8.8	19.9	1, 44	< 0.001	0.31	-2.2 ± 0.5	40 ± 5
psu = 27	16.9	1, 32	< 0.001	0.35	-2.3 ± 0.6	57 ± 5
psu = 30	0.5	1, 38	0.491	0.01	-	-
psu = 34	3.1	1, 47	0.0859	0.06	-	-
psu = 38	1.1	1,42	0.290	0.03	-	-
psu = 46	10.7	1, 39	0.002	0.22	-2.3 ± 0.7	57 ± 7
4 °C	3.1	1, 47	0.086	0.06	-	-
20 °C	25.3	1, 44	< 0.001	0.36	-5 ± 1	74 ± 9

Supplementary Information 3.7.

Table 11. Comparison of surface area normalized barium sulfate dissolution rates observed in this investigation with those calculated from rate constants reported in Zhen-Wu et al. (2016). Ω_{BaSO_4} is the average of the estimated Ω_{BaSO_4} of each treatment in the specified experiment. Average surface area (SA) per barium sulfate crystal at Day 0 is estimated by multiplying the two-dimensional area acquired from SEM images by 3.8, a constant derived from the idealized barite habit of Goldshmidt (1926) barite no. 325. $Rate_{1K}$ and $Rate_{DA}$ are the surface area normalized barium sulfate dissolution rates calculated at the specified Ω_{BaSO_4} from rate constants for Zhen-Wu et al. (2016) experiments 1K and DA, respectively. Experiment 1K was conducted at 25°C in a solution of 1.0 mol kg^{-1} NaCl at a shaking speed of 0.2 cycles s^{-1}. Experiment DA was conducted at 25°C in a solution of 0.1 mol kg^{-1} NaCl at a shaking speed of 1.3 cycles s^{-1}.

Experiment/ Treatment	Ω_{BaSO_4}	**Surface Area (μm²)**	**Dissolution Rate (mol m^{-2} s^{-1})**	**$Rate_{1K}$ (mol $m^{-2}s^{-1}$)**	**$Rate_{DA}$ (mol m^{-2} s^{-1})**
pH	0.44	37.8 ± 0.7	$-4.2 \pm 0.5 \times 10^{-9}$	-1.2×10^{-8}	-4.9×10^{-8}
Salinity	0.44	34.8 ± 0.8	$-2.4 \pm 0.6 \times 10^{-9}$	-1.2×10^{-8}	-4.9×10^{-8}
Temperature	0.32	40 ± 1	$-4 \pm 1 \times 10^{-9}$	-1.6×10^{-8}	-6.6×10^{-8}
No aggregates	0.19	126 ± 9	$-7 \pm 3 \times 10^{-9}$	-2.2×10^{-8}	-9.1×10^{-8}

Supplementary Information 3.8.

Table 12. Correlations between core top Ba measurements, other marine carbon cycle proxies, and export production estimates from datasets presented in Hayes et al. (2020), Schoeopfer et al. (2015), Serno et al. (2014), and Shen et al. (2023). Data from Schoeopfer et al. (2015) and Shen et al. (2023) suggest that sediment barite shows a stronger positive correlation with some organic matter accumulation proxies than export production estimates, but data from Hayes et al. (2020) and Serno et al. (2014) do not. See original publications for details regarding sample locations, analytical methods, export production methods etc. Pearson correlation tests were conducted for each comparison. Comparisons with $p < 0.05$ are bolded and comparisons with a negative correlation coefficient are in gray. Ba_{xs} is excess barium (barium corrected for terrigenous input), TOC is total organic carbon, EP is export production, and P_{Org} is organic phosphorous. Raw data from Shen et al. (2023) was not available, so correlation tests were conducted on data extracted from figures.

Comparison	**df**	**r**	**p**
Hayes et al. (2020)			
Ba_{xs}, $CaCO_3$	**840**	**-0.15**	**< 0.001**
Ba_{xs}, Opal	632	0.01	0.817
Ba_{xs}, TOC	**739**	**-0.15**	**< 0.001**
Ba_{xs}, EP*		**0.22**	**< 0.05**
Schoeopfer et al. (2015) (oxic facies only)			
Ba_{xs}, $CaCO_3$ & Opal	1366	0.22	**< 0.001**
Ba_{xs}, TOC	885	-0.29	**< 0.001**
Ba_{xs}, P_{Org}	850	0.14	**< 0.001**
Ba_{xs}, EP_{Dunne}	1357	-0.12	**< 0.001**

Table 13. Correlations between core top Ba measurements, other marine carbon cycle proxies, and export production estimates from datasets presented in Hayes et al. (2020), Schoeopfer et al. (2015), Serno et al. (2014), and Shen et al. (2023). Data from Schoeopfer et al. (2015) and Shen et al. (2023) suggest that sediment barite shows a stronger positive correlation with some organic matter accumulation proxies than export production estimates, but data from Hayes et al. (2020) and Serno et al. (2014) do not. See original publications for details regarding sample locations, analytical methods, export production methods etc. Pearson correlation tests were conducted for each comparison. Comparisons with $p < 0.05$ are bolded and comparisons with a negative correlation coefficient are in gray. Ba_{xs} is excess barium (barium corrected for terrigenous input), TOC is total organic carbon, EP is export production, and P_{Org} is organic phosphorous. Raw data from Shen et al. (2023) was not available, so correlation tests were conducted on data extracted from figures. (Continued)

Comparison	**df**	**r**	**p**
Ba_{xs}, EP_{Oregon}	1171	-0.10	< **0.001**
Ba_{xs}, $EP_{Longhurst}$	1357	-0.29	< **0.001**
Serno et al. (2014)			
Ba_{xs}, $CaCO_3$	25	0.08	0.709
Ba_{xs}, Opal	25	-0.24	0.226
Ba_{xs}, EP	21	0.02	0.924
Shen et al. (2023)			
Ba_{xs}, planktonic foraminifera	**27**	**-0.51**	**0.004**
Ba_{xs}, benthic foraminifera	27	-0.003	0.987

* Correlation statistics for this comparison were taken directly from Hayes et al. 2020, so degrees of freedom are not available.

Supplementary Information for CHAPTER 4

Supplementary Information 4.1.

Table 14. Sampling locations, types of sampling conducted, and the water depths sampled at all 6 study sites. Samples analyzed here are shaded in gray, while samples without highlighting have yet to be analyzed.

Latitude	Longitude	Sampling conducted	Water depths sampled
32.60 N	117.57	Sediment only	NA
32.58 N	118.52	Seawater, sediment	50,100, 200, 401, 601, 800, 1000, 1125
32.70 N	120.63 W	Seawater, sediment	49, 100, 200, 400, 601, 803, 1002, 1396, 2009, 3002, 3500, 3794
32.70 N	122.28 W	Seawater, sediment (limited sediment recovery)	50, 98, 186, 401, 600, 804, 1000, 1403, 2000, 2999, 3995, 4175
32.70 N	123.88 W	Seawater, sediment	50, 94, 204, 401, 660, 778, 1001, 1401, 1999, 2997, 3944, 4344
32.70 N	125.60 W	Seawater, sediment	52, 151, 402, 500, 701, 1404 x 2, 2000 x 2, 3998, 4505